Design and Electrochemical Study of Pd-based Nanostructures for Hydrogen Economy

By

Suresh Kumar Konda

A dissertation submitted in partial fulfillment of the requirements of the degree of

Doctor of Philosophy in Chemistry and Materials Science

Department of Chemistry

Lakehead University, Thunder Bay, Ontario, Canada

Abstract

Hydrogen storage remains one of the most challenging prerequisites to overcome toward the realization of a hydrogen based economy. The use of hydrogen as an energy carrier for fuel cell applications has been limited by the lack of safe and effective hydrogen storage materials. Another major challenge associated with fuel cells is the design of highly efficient electrocatalysts to reduce the high overpotential of the oxygen reduction reaction (ORR). Palladium has a high affinity for hydrogen sorption and has been extensively studied, both in the gas phase and under electrochemical conditions. Palladium has strong potential to play a major role in many aspects of a hydrogen based economy, leading to promising applications, encompassing hydrogen purification, storage and as a cathode to facilitate the oxygen reduction reaction.

During my PhD study, Cd@Pd core/shell nanostructured materials were synthesised for enhanced hydrogen sorption and storage. The effect of a capping agent was investigated, showing that it plays a critical role in the formation of the uniform and small size of the Cd@Pd nanostructures. The capacity for hydrogen sorption and storage was strongly contingent on the composition and structure of the formed Pd-based nanomaterials, as well as the applied electrode potential. The Cd@Pd core/shell nanostructure with an optimized composition of 1:2 exhibited the highest capacity for hydrogen storage, where a 340% increase was achieved in contrast to pure Pd nanoparticles.

The behaviours of the electrosorption of hydrogen into untreated and annealed Pd thin foils were systematically investigated with a primary effort concentrated on elucidating the effects of annealing on hydrogen uptake capacities. The change of the crystalline structure of Pd during the annealing process was monitored by in situ X-ray diffraction. Scanning electron microscopic images revealed the significant effect of the annealing temperature on the morphology of Pd thin

foils. Cyclic voltammetric and chronoamperometric techniques were employed to study the kinetics of hydrogen electrosorption, where α phase, β phase, and their transition were determined with respect to the electrode potential. The morphological and structural changes, as well as lattice parameters, played an important role in hydrogen uptake. A Pd thin foil annealed at 700 °C exhibited an over 19.4-fold increase in hydrogen uptake capacity in comparison to an untreated one.

In the next step, Pd nanoparticles and reduced graphene oxide nanocomposites were synthesized using a facile one-step electrochemical approach for promising applications in hydrogen sorption. The prepared nanocomposites exhibited significantly improved performance toward hydrogen sorption and storage in contrast to rGO and pure Pd nanoparticles. The Pd/rGO nanocomposite exhibited an increased hydrogen storage capacity of over 11 fold in the α phase and more than a fivefold enhancement in the β phase when compared to Pd nanoparticles.

Finally, to reduce the high overpotential of the oxygen reduction reaction in fuel cells, a facile photoassisted method was employed for the direct deposition of palladium nanoparticles onto graphitic carbon nitride for the efficient reduction of oxygen. The synthesized Pd-g-C_3N_4 nanocomposite exhibited robust electrocatalytic behavior toward the ORR in 0.1 M KOH solution, where the desirable four electron pathway was achieved. In addition, the developed catalyst demonstrated a significantly improved tolerance against methanol as well as enhanced stability in comparison to the commercial benchmark platinum-loaded carbon catalysts.

Acknowledgements

I would like to extend my sincere gratitude to my advisor, Professor Aicheng Chen, for his guidance throughout the course of this PhD studies. I would like to thank my committee members, Drs. Alla Reznik and Robert Mawhinney for taking the time to review my PhD thesis and for their insightful comments. I would like to thank Dr. Francis Appoh for his encouragement and support throughout my PhD studies.

I acknowledge Ontario Trillium Scholarship provided by the government of Ontario and Lakehead University for international PhD students in Canada. I also want to take this opportunity to thank both faculty and the staff members of Department of Chemistry, Instrument Lab and Graduate Studies for their support and encouragement. I would like to take this opportunity to thank all other members of the research group, past and present, who have lent me their assistance and expertise.

I acknowledge Canadian Centre Electron Microscopy at McMaster University for obtaining the TEM images and the Surface Interface Ontario/Chemical Engineering & Allied Chemistry at the University of Toronto for carrying out the XPS analysis.

Last, but not least, I would like to thank all of my family and friends from the bottom of my heart for their continuous support and encouragement.

List of Figures

List of Tables

List of Abbreviations and Symbols

AC	Activated Carbon
ACF	Activated Carbon Fiber
Ar	Argon
BET	Brunauer-Emmett-Teller
Cd	Cadmium
CA	Carbon Aerogels
CNF	Carbon Nanoflower
CNT	Carbon Nanotube
CA	Chronoamperometry
COF	Covalent Organic Framework
CV	Cyclic Voltammetry
DFT	Density Functional Theory
DOE	Department of Energy
DMFCs	Direct Methanol Fuel Cells
DWNT	Double Walled Carbon Nanotube
EDS	Energy-dispersive X-ray Spectroscopy
GCE	Glassy Carbon Electrode
g-C_3N_4	Graphitic Carbon Nitride
GO	Graphite Oxide
HCS	Hollow Carbon Sphere
ICP-AES	Inductively Coupled Plasma Atomic Emission Spectroscopy

MOF	Metal Organic Framework
MWNT	Multi Walled Carbon Nanotube
N	Nitrogen
N-HEG	Nitrogen Doped Hydrogen Exfoliated Graphene
OMC	Ordered Mesoporous Carbon
ORR	Oxygen Reduction Reaction
Pd	Palladium
PEM	Proton Exchange Membrane
rGO	Reduced Graphene Oxide
RDGCE	Rotating Disc Glassy Carbon Electrode
SEM	Scanning Electron Microscopy
SN	Silica Nanotubes
SWNT	Single Walled Carbon Nanotube
TGA	Thermo Gravimetric Analysis
TPD	Temperature Programmed Desorption
TC	Template Carbon
TEM	Transmission Electron Microscopy
XRD	X-ray Diffraction Spectroscopy
XPS	X-ray Photoelectron Spectroscopy

Table of Contents

Chapter 1: Introduction and Thesis Scope

Increasing global energy demands have shown that an economy that is based solely on fossil fuels, such as oil and coal, results in a significant increase in carbon dioxide emissions. There is a critical need for the development of non-fossil fuel energy resources. Sustainable alternatives, including solar, wind, geothermal, and fuel cells, are currently under active investigation. Fuel cells are considered to be a promising alternative green energy technology with applications spanning numerous areas, including portable power, transportation, and stationary power generation.[1,2,3] However, before this is possible, several scientific challenges associated with hydrogen fuel cell technologies must be resolved. One of these is the storage of hydrogen at ambient pressures and temperatures to enable the commercialization of fuel cell applications. An additional issue for fuel cells is the development of high-performance cathode electrocatalysts that reduce the high overpotential that is present during the oxygen reduction reaction (ORR).[4,5]

1.1 Hydrogen Production: Although hydrogen is the most abundant element on earth, it is not typically found as molecular H_2 but rather, it is chemically bound in water, and to a limited extent in hydrocarbons and carbohydrates. Therefore, hydrogen must be produced as a synthetic fuel from hydrogen containing sources. Currently the majority of the hydrogen is generated from natural gas, employing a process referred to as steam reforming.[6] For sustainability, the hydrogen should be produced from the electrolysis of water using the energy derived from renewable and non-fossil resources such as solar, wind, geothermal, tidal/wind, and biomass. However, the cost of producing hydrogen through such means is currently several times higher than from natural gas; hence, cost reduction constitutes a major challenge.[7]

1.2 Hydrogen Storage

Another crucial challenge facing the widespread use of hydrogen as a fuel, particularly for mobile applications, pertains to the localized storage of hydrogen in an efficient, safe, and cost effective way. In order to be comparable with conventional gasoline or diesel based vehicles, hydrogen fuel cell vehicles must attain a range of ~500 km before requiring refuelling. Typically, only about 5 kg of hydrogen is required to cover this distance; however, due to the low density of hydrogen (0.089 g/l), this would occupy a volume of ~56,000 litres under ambient conditions. The challenge is to safely contain this 5 kg (56,000 l) of hydrogen in a system that is lightweight and compact enough to be comparable to the gasoline tank of a conventional automobile (~30-35 litres).[8] For both stationary and mobile applications, compact and safe hydrogen storage is key if H_2 is to be used as a fuel.[9] Three primary hydrogen storage options encompass compressed gas, cryogenic liquid, and chemical hydrogen storage.

Liquefied Hydrogen*:* H_2 may be stored in a liquid form at -253 °C. The volumetric energy density of liquid H_2 (70 g/L H_2) is high compared to an 800 bar H_2 (g) tank. However, its application is hindered by safety, energy efficiency, and handling considerations. The use of liquid hydrogen is further hampered by continuous loss (~1% per day) of hydrogen through boil-off. Therefore this storage method is not considered viable for application in automobliles at a large scale.[10,11]

High-Pressure Gas Tanks*:* Most common high-pressure cylinders are loaded to a maximum of 200 bar H_2 pressure. Newly developed lightweight nanocomposite tanks allow increases in pressure of up to 800 bar, from which a relatively high gravimetric (5.5 Wt.% H_2) and volumetric (37 g/L H_2) energy density may be achieved. For onboard hydrogen storage, the current state of the art includes 350 and 700 bar pressurized tanks, where the primary research effort in this direction focuses on decreasing the weight and cost of the tank.[10,11,12] Solid state materials have the capacity to

reversibly release and take up hydrogen, and there are two mechanisms by which hydrogen may bind with materials.

Physisorption*:* In this process molecular hydrogen is weakly adsorbed onto the surface of a material through van der Waals interactions. Carbon based materials, such as carbon nanotubes, fibers, fullerenes, and activated carbon have been investigated for hydrogen storage.[13,14,15]

Metal hydrides*:* The second class of solid state hydrogen storage media are materials in which atomic hydrogen (H) is absorbed by metal or metal alloys to form metal hydrides. Metal hydrides are often classified according to the nature of the bonding between hydrogen and the metal.[15] Significant advances in metal hydrides are discussed in more detail in the following chapter.

1.3 Oxygen Reduction Reaction: Oxygen is the most abundant element in the Earth's crust. The oxygen reduction reaction is also the most critical reaction in life processes, such as biological respiration, and in energy converting systems, such as fuel cells. In proton exchange membrane fuel cells, including direct methanol fuel cells, ORR is the reaction that occurs at the cathode. Normally, the ORR kinetics are very slow; hence, the development of high-performance cathode catalyst is required in order to reduce the high overpotential that is present during the oxygen reduction reaction. At present, Pt-based materials comprise the most practical catalysts. Although Pt demonstrates the highest activity among pure metals in cathodic oxygen reduction reactions, it remains an unsatisfactory candidate for the production of commercially viable fuel cells, due to its sluggish reaction and exorbitant expense.[16,17] Various studies have been conducted toward the identification of catalyst materials that might serve as a substitute for Pt, either partially or completely.[18] For the oxygen reduction reaction, Pd-alloys have also demonstrated improved performance when compared to Pt, particularly in the presence of methanol. Even though the cost

of Pd is lower in comparison to Pt, the price of Pd remains above acceptable levels for large-scale commercial applications.[5]

1.4. Thesis scope

The aim of my PhD thesis is to design and study the electrochemical activity of advanced Pd-based nanomaterials toward a sustainable hydrogen economy. The specific objectives of my PhD project are two-fold: (i) to synthesize Pd-based nanomaterials/nanocomposites; and (ii) to study their electrochemical performance for hydrogen storage, spillover, and for the oxygen reduction reaction. Spillover is defined as the transport of a species, adsorbed or formed on a surface, to another surface, which does not adsorb or form this species under similar conditions. The incorporation of more economical metals (e.g., Ag, Cd, Ni, Sn) into Pd may enhance the kinetic and thermodynamic properties of hydrogenation and dehydrogenation.[19] Further, by depositing small amounts of Pd-containing nanoparticles into cost-effective supporting materials such as carbon, graphene, and carbon nitride, might potentially enhance thermodynamic and kinetic properties sufficiently to obtain a practical hydrogen storage material at low temperatures and pressures for commercial hydrogen storage applications.

Chapter 2 of this thesis introduces significant issues that are associated with Pd based nanomaterials, and the importance of these nanomaterials for the sustainable development of a hydrogen based economy. A specific focus on recent advancements are highlighted and discussed in regard to palladium based nanomaterials for hydrogen storage and the oxygen reduction reaction, as well as the effects of hydrogen spillover on various adsorbents, including carbons, metal organic frameworks, covalent organic frameworks, and other nanomaterials.

Chapter 3 introduces basic materials, methods, and characterisation techniques, as well as the synthesis methods that are employed to fabricate various Pd-based nanomaterials or nanocomposites.

In Chapter 4 the successful synthesis of a novel Cd@Pd nanostructure with a Cd core and Pd shell is described, which exhibited a high capacity for hydrogen sorption and storage. The effect of capping agent on this core shell formation was systemically investigated, as well as the impact of the composition on hydrogen sorption. By forming Cd as the core and Pd as the shell, the Pd served not only as a catalyst for hydrogen sorption, but also protected the Cd core from corrosion, which is very important for applications in catalysis.

In Chapter 5 of this thesis, the effects of in situ annealing on Pd thin films for electrochemical hydrogen uptake at room temperature were actively investigated. Alterations in the crystal size and lattice parameters under high temperatures following annealing were studied in detail. The morphological and structural changes, as well as lattice parameters, played a critical role in the uptake of hydrogen into the Pd thin foil.

Chapter 6 introduces a green method for the simultaneous synthesis of Pd nanoparticles and reduced graphene oxide nanocomposites using one step electrochemical reduction approach for hydrogen spillover and storage. Experimental results revealed that the prepared nanocomposites exhibited significantly improved performance toward hydrogen sorption and storage, in contrast to reduced graphene oxide and pure Pd nanoparticles.

As aforementioned, an additional objective of this PhD project was the development of Pd-based electrocatalysts as a cathode for efficient ORR in fuel cells.

Chapter 7 introduces a novel method for the deposition of Pd nanoparticles onto graphitic carbon nitride using a photochemical reduction approach for the oxygen reduction reaction in alkaline fuel

cells. There was an immense improvement in ORR activity when Pd was deposited onto g-C_3N_4. In contrast to a commercial Pt/C catalyst, the developed Pd-g-C_3N_4 nanocomposite demonstrated excellent methanol tolerance and high ORR stability.

Chapter 8 presents the comparative analysis of hydrogen storage capacities of materials that were synthesised using different methods that were mentioned in chapter 4 to 6. Concluding remarks and summary of the thesis.

References:

1. A. Chen. Electrocatalysis and photoelectrochemistry based on functional nanomaterials. *Can. J. Chem.* **2014,** 92, 581-597.

2. H. Zhang, M. Jin, Y. Xia. Enhancing the catalytic and electrocatalytic properties of Pt-based catalysts by forming bimetallic nanocrystals with Pd. *Chem. Soc. Rev* **2012,** 41, 8035-8049.

3. S. Guo, E. Wang. Noble metal nanomaterials: Controllable synthesis and application in fuel cells and analytical sensors. *Nano Today* **2011,** 6, 240-264.

4. S. K. Konda, M. Amiri, A. Chen. Photoassisted deposition of palladium nanoparticles on carbon nitride for efficient oxygen reduction. *J. Phys. Chem. C* **2016,** 120, 14467-14473.

5. A. Chen, C. Ostrom. Palladium-based nanomaterials: synthesis and electrochemical applications. *Chem. Rev.* **2015,** 115, 11999-12044.

6. N. A. Al-Mufachi, N. V. Rees, R. Steinberger-Wilkens. Hydrogen selective membranes: A review of palladium-based dense metal membranes. *Rene. Sus. Ener. Rev.* **2015,** 47, 540-551.

7. K. Zeng, D. Zhang. Recent progress in alkaline water electrolysis for hydrogen production and applications. *Prog. Energ. Combust. Sci.* **2010,** 36, 307-326.

8. L. Schlapbach. Technology: Hydrogen-fuelled vehicles. *Nature* **2009,** 460, 809-811.

9. S. Dutta, A review on production, storage of hydrogen and its utilization as an energy resource. *J. Indus. Eng. Chem.* **2014,** 20, 1148-1156.

10. P. P. Edwards, V. L. Kuznetsov, W. I. F. David. Hydrogen energy. *Philos. T. Roy. Soc. A.* **2007,** 365, 1043-1056.

11. K. Hirose. Materials towards carbon-free, emission-free and oil-free mobility: hydrogen fuel-cell vehicles-now and in the future. *Philos. T. Roy. Soc. A.* **2010,** 368, 3365-3377.

12. J. Tollefson. Hydrogen vehicles: Fuel of the future. *Nature* **2010,** 464, 1262-1264.

13. L. Schlapbach, A. Zuttel. Hydrogen-storage materials for mobile applications. *Nature* **2001,** 414, 353-358.

14. J. Yang, A. Sudik, C. Wolverton, D. J. Siegel. High capacity hydrogen storage materials: attributes for automotive applications and techniques for materials discovery. *Chem. Soc. Rev.* **2010,** 39, 656-675.

15. S. K. Konda, A. Chen. Palladium based nanomaterials for enhanced hydrogen spillover and storage. *Mater. Today* **2016,** 19, 100-108.

16. Y. J. Wang, N. Zhao, B. Fang, H. Li, X. T. Bi, H. Wang. Carbon-supported Pt-based alloy electrocatalysts for the oxygen reduction reaction in polymer electrolyte membrane fuel cells: particle size, shape, and composition manipulation and their impact to activity. *Chem. Rev.* **2015,** 115, 3433-3467.

17. A. Chen, P. Holt-Hindle. Platinum-based nanostructured materials: synthesis, properties, and applications. *Chem. Rev.* **2010,** 110, 3767-3804.

18. L. Zhang, J. Zhang, D. P. Wilkinson, H. Wang. Progress in preparation of non-noble electrocatalysts for PEM fuel cell reactions. *J. Power Sources* **2006,** 156, 171-182.

19. B. D. Adams, A. Chen. The role of palladium in a hydrogen economy. *Mater. Today* **2011,** 14, 282-289.

Chapter 2: Literature Review

2.1 Introduction

Hydrogen has the potential to be a principal energy carrier. It has attracted significant attention not only because of its high energy density, but also because of the technological problems involved with its storage and release.[1,2] Since hydrogen is gaseous at ambient temperature and pressure, its confined storage is impractical. It is clear that the key challenge in developing this technology is centered on the viable storage of hydrogen. Presently hydrogen may be stored by different techniques such as within compressed tanks, in liquefied form, and as solid state hydrides. Currently, however, none of these storage methods have met the demands for onboard vehicular applications.[3-7] For transportation applications, the US Department of Energy (DOE) has set ≥ 7.5 wt.% as the system capacity targets for onboard hydrogen storage in fuel cell applications in vehicles under ambient temperature and a maximum pressure of 12 bar.[8,9] Solid-state materials have been considered as potential candidates for hydrogen storage, over other storage techniques.[10] The hydrogen storage capacities of various solid state hydrides are displayed in Fig. 1.1[9]. Hydrogen may be stored as either molecular hydrogen (physisorption), or as atomic hydrogen (chemisorption). The storage of molecular hydrogen relies on weak physisorption, and results in lower hydrogen capacities under mild conditions, whereas chemisorption can occur under ambient conditions, but utilizes materials that are very expensive. In some cases, the hydrogen sorption phenomena are irreversible, albeit higher temperatures can facilitate the release of the adsorbed hydrogen.[11,12]

---

*Most of the results presented in this chapter have been published in *Materials Today*, **2016,** 19, 100-108

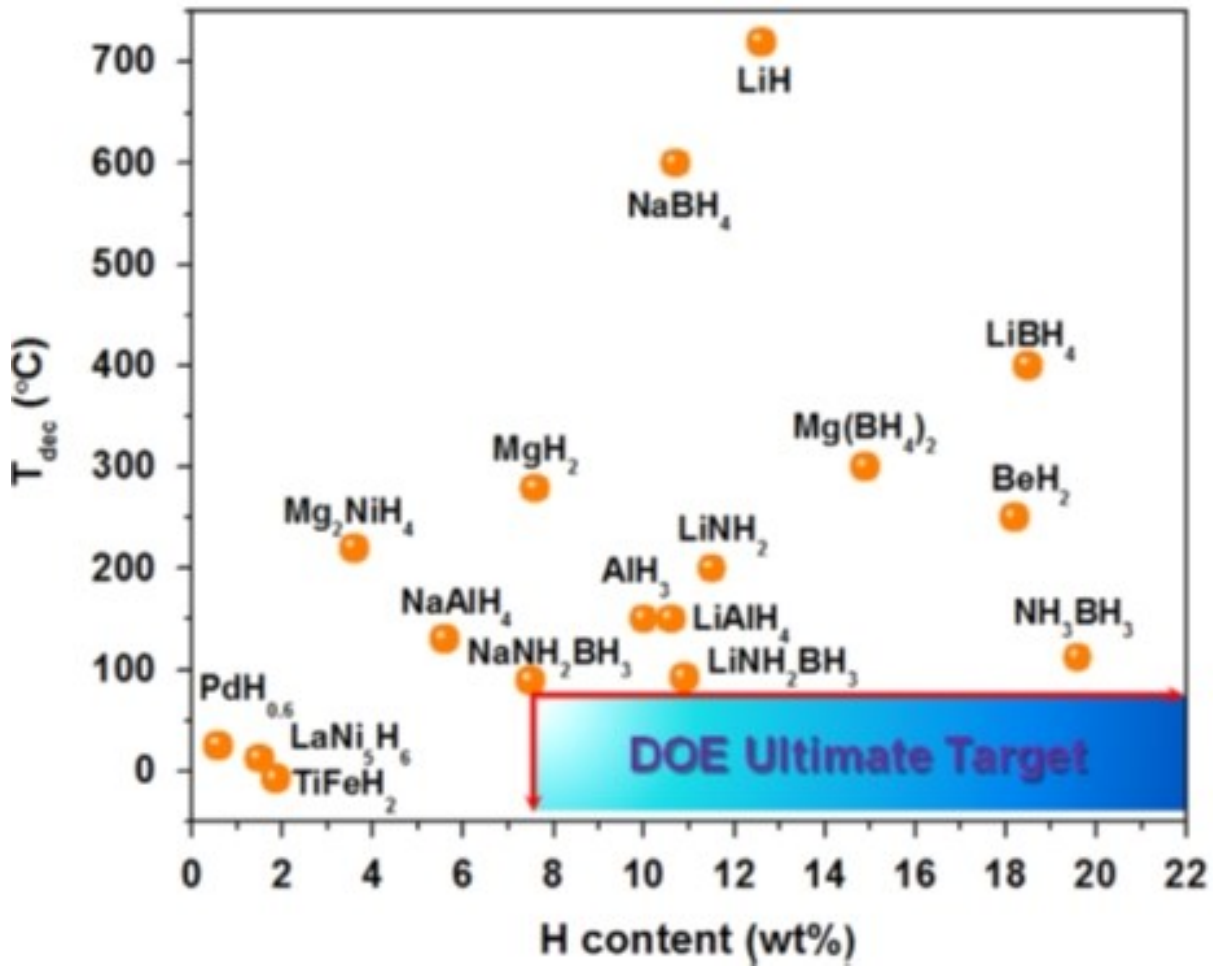

Figure. 1.1 Overview of various solid-state hydrides, plot of decomposition temperatures (under 1 bar H_2 pressure) as function of heavy-metric hydrogen content. The ultimate DOE target is shown in the shadowed bar. (Reprinted with permission from Reference 9 © 2015 Elsevier).

2.2 Significance of Pd in Hydrogen Storage

An inherent affinity and selectivity for hydrogen, rapid sorption kinetics and hydride formation reversibility are exhibited by Pd, which enable its integration into various hydrogen technologies. Pd is considered to be unique material with a strong affinity to hydrogen, owing to both its catalytic and hydrogen absorbing properties[13,14] and it plays important role in a hydrogen economy encompassing hydrogen production, purification, storage and in fuel cells. Adams et al., have discussed the roles played by Pd in hydrogen economy in their review paper.[15] Intensive investigations of Pd hydrides have been conducted in various fields of fundamental science and technology. In contrast to their bulk counterparts, nanostructured materials appear to exhibit more rapid charging and discharging kinetics, extended life cycles, and size tunable thermodynamics.[16,17] Many investigations of hydrogen storage employing bulk Pd or Pd based nanoparticles have been carried out recently.[18] In particular, Pd nanoparticles have been studied as an exemplar model for the elucidation of the hydrogen-storage properties of metallic nanoparticles.

The absorption of hydrogen by Pd results in the formation of two phases. At low hydrogen concentrations (solid solution) the alpha phase appears, whereas at higher hydrogen concentrations (metal hydride) the beta phase appears. A schematic phase diagram of palladium hydride is depicted in Fig. 2.2.[19] Hydrogen concentrations and equilibrium pressures for the formation of Pd hydrides were reported to decrease with smaller nanoparticle dimensions.[20] In addition to size, the morphologies of metallic nanoparticles have also been critical to materials chemistry, in that their intrinsic properties are strongly correlated with their geometries.[21,22] Recent work by Li et al. has demonstrated that the morphology of Pd may play a critical role in the storage capacity of hydrogen, and that temperature plays a critical role in its uptake, absorption, and diffusion.[23]

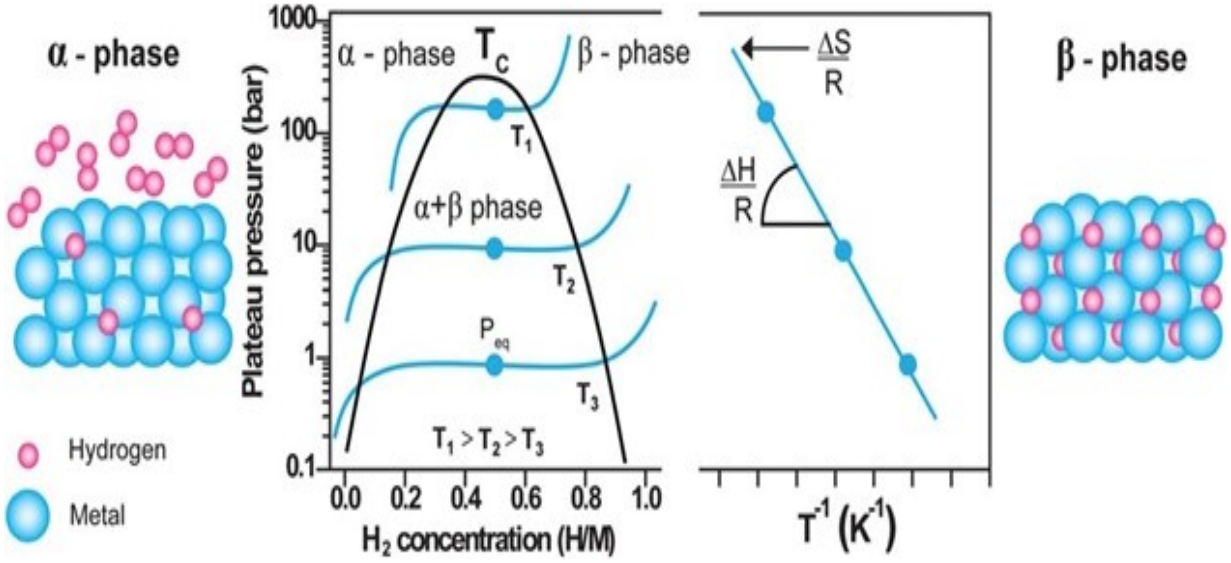

Figure. 2.2 (Left) Pressure-composition isotherm plot of metal to metal hydride phase transition. (right) Van't Hoff plot related to the phase transition from metal to metal hydride. Schematic representation of alpha-phase (left) and beta-phase (right) of metal hydride are also shown. (Reprinted with permission from Reference 19 © 2011 Royal Society of Chemistry)

Phase transitions of individual palladium nanocrystals during hydrogen absorption and desorption were investigated using in situ electron energy-loss spectroscopy under an environmental transmission electron microscope. Palladium nanocrystals undergo extreme transitions between α and β phases, where surface effects dictate the size dependence of hydrogen absorption pressures.[16] A major disadvantage associated with the use of pure Pd is hydrogen embrittlement. This occurrence is related to the cracking of the membrane upon large expansion of the lattice constant. In order to reduce hydrogen embrittlement, Pd is alloyed with other metals, which results in the expansion of the Pd lattice, thus Pd becomes less influenced by

hydrogen. A number of studies were carried out using a combination of Pd based alloys such as PdPt, PdCd, PdRu, PdRh, PdAg, PdCdAg to control hydrogen embrittlement.[18, 24-29] In their work, T. Hango et al. investigated the effect of grain structure on hydrogen embrittlement using pure Pd (99.9%), which was processed by high pressure torsion (HPT) to form an ultrafine-grained (UFG) structure. Tensile tests revealed that, unlike coarse-grained samples in which hydrogen-induced embrittlement and hardening occurred, hydrogen-induced softening and elasticity occurred in the HPT-processed UFG sample.[30]

2.3 Hydrogen Spillover

It was observed by Khoobiar in 1964 that WO_3 was reduced by H_2 to blue WO_{3-x} when it came into contact with a platinum (Pt) catalyst. The presence of blue color was due to the chemisorptive dissociation of H_2 molecules on the surface of Pt particles that migrated to the yellow WO_3 particles, reducing them to blue WO_{3-x} particles.[31] Subsequently, Boudart et al. coined the term "spillover" to describe the migration of H atoms from the metal particles to the substrate, explaining that H atoms spill over from hydrogen-rich to hydrogen-poor surfaces.[32] Extensive investigations as to the nature of hydrogen spillover were undertaken, particularly as it relates to the partial electron transfer from the hydrogen species to the solid material.[33] Hydrogen spillover has since emerged as one of the most promising techniques for the achievement of high-density hydrogen storage at close to ambient conditions within lightweight, solid-state materials. Spillover is defined as "the transport of active species that have sorbed or formed on a first surface, migrated onto another surface that does not sorb or form active species under the same conditions". Thus, the adsorbed species gain access to a different surface phase (accepting surface) that is in contact with the original adsorbing and activating surface. Spillover is critical in adsorption, and as a mechanistic step in heterogeneous catalysis.[34-37] The process of hydrogen spillover involves three

primary steps: (i) chemisorptive dissociation of gaseous hydrogen molecules on a transition metal catalyst; (ii) migration of hydrogen atoms from the catalyst to the substrate; and (iii) diffusion of hydrogen atoms onto substrate surfaces. The migration of H atoms from catalysts to substrates, as well as H atom diffusion within the substrates, may be mapped out by calculating minimum energy pathways. A simple and effective technique was developed for the creation of carbon bridges that served to improve the contact between a spillover source and a secondary receptor. As shown in Fig. 2.3, a Pd-C catalyst served as the hydrogen atom source via dissociation and primary spillover, whereas super activated carbon (AX-21), or single-walled carbon nanotubes (SWNTs) functioned as secondary spillover receptors. By carbonizing a bridge forming precursor in the presence of these components, the hydrogen adsorption volume was increased by a factor of 2.9 for the AX-21 receptor, and 1.6 for the SWNT receptor, at 298 K at 100 kPa and 10 MPa, indicating that the enhancement factor was a weak function of pressure. Reversibility was demonstrated through desorption and re-adsorption at 298 K. The bridge-building process appeared to be receptor specific, where optimization might yield an even greater enhancement.[38] Further, the effect of surface contacts between Pd and the carbon support and the thermodynamics involved were demonstrated by Bhat et al.[39] A greater proportion of Pd/carbon contacts for Pd nanoparticles embedded within a microporous carbon matrix induced the efficient 'pumping' of hydrogen from the β-PdHx. It was also discovered that the thermal cleaning of carbon surface groups prior to exposure to hydrogen further enhanced the hydrogen pumping power of the microporous carbon substrate. In brief, this study highlighted that the stability of the β-PdHx phase supported on carbon is contingent on the degree of contact between the Pd catalysts and carbon supports, as well as the nature of the carbon surface.[39]

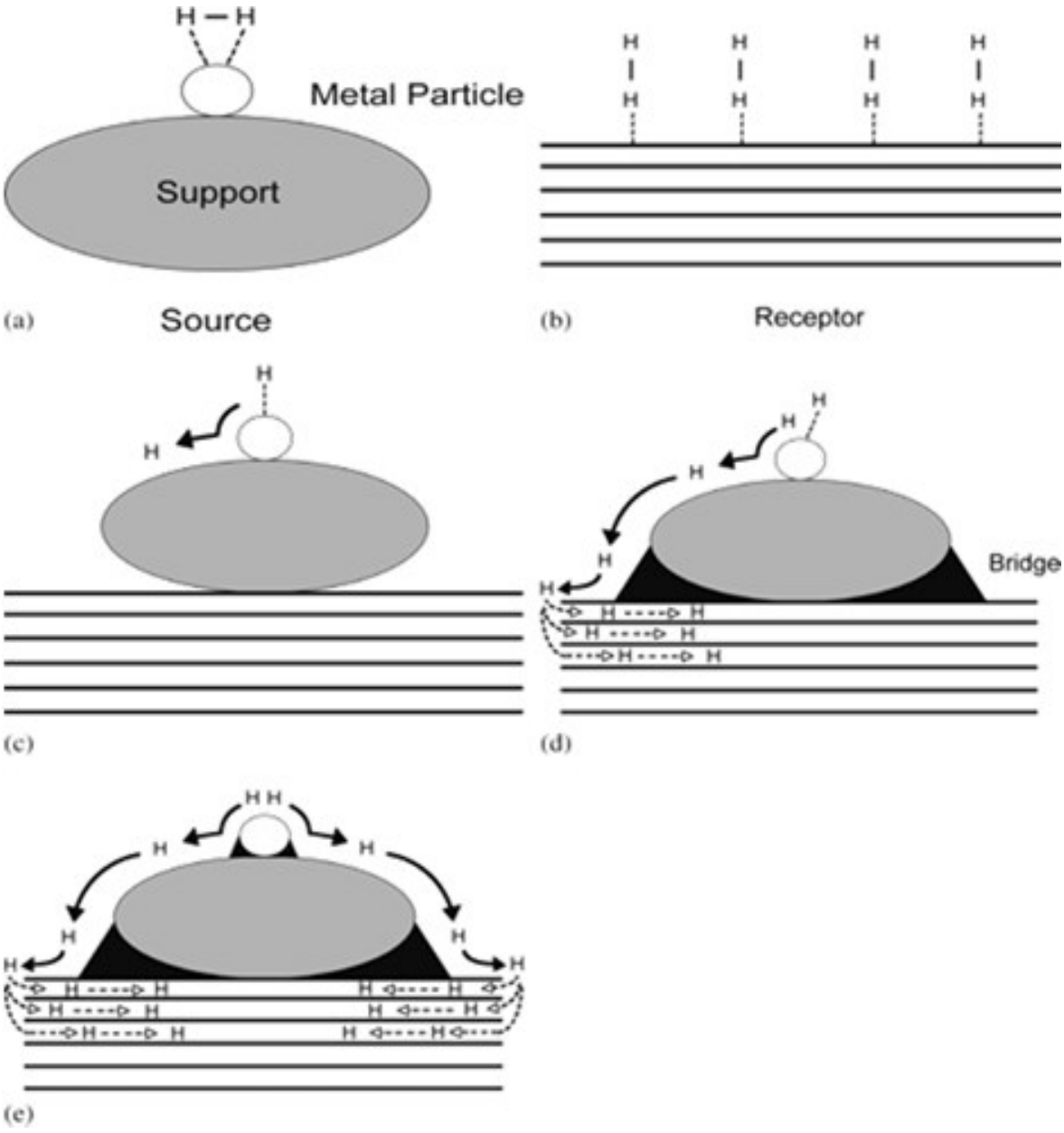

Figure. 2.3 Hydrogen spillover in a supported catalyst system: (a) adsorption of hydrogen onto a supported metal nanoparticle; (b) low-capacity receptor; (c) primary spillover of atomic hydrogen to the support; (d) secondary spillover to the receptor enhanced by a physical bridge; (e) primary and secondary spillover enhancement by improved contacts and bridges. (Reprinted with permission from Reference 38. © 2005 American Chemical Society).

2.4 Experimental and Theoretical Studies of Hydrogen Spillover

Hydrogen spillover has been studied extensively, particularly in the field of catalysis. Direct evidence for the spillover of atomic hydrogen at room temperature may be studied using different techniques. The inelastic neutron scattering (INS) method is uniquely capable of revealing the state of hydrogen, in either atomic or molecular form. The INS results indicate a direct quantitative evaluation of the volume of hydrogen adsorbed on activated carbon in atomic form via spillover. Atomic hydrogen spillover was observed from a Pd catalyst, to activated carbon fibers loaded at 77 K with 2.5 wt % H_2. It was found that new C-H bonds were formed at the expense of physisorbed H_2, during prolonged in situ exposure to 1.6 MPa hydrogen at 20°C. This verified the atomic nature of H species that were formed in the presence of a Pd catalyst and of their subsequent spillover and binding to a carbon support.[40] A similar observation by Tsao et al. illustrated that the modification of molecular hydrogen in Pt-doped activated carbon samples provided evidence that significant populations of hydrogen atoms may diffuse to a carbon surface at room temperature during the spillover process.[41] For comparison, a material known to exhibit hydrogen spillover at room temperature (Pt/C) was also studied with the hydrogen-deuterium scrambling reaction, where the isotherms were reversible. For desorption, sequential doses of H_2 and D_2 at room temperature, and subsequent temperature programmed desorption (TPD), yielded product distributions that were strong indicators of a surface diffusion controlled reverse spillover process.[42] Spectroscopic study has provided evidence of atomic hydrogen spillover from chemisorption sites in a Cu-TDPAT to Pt/C catalyst.[43] An in situ diffuse reflectance Fourier-transform Infrared spectroscopic study indicated that the hydrogen was stored in the form of CH_x ($x = 1, 2$) species, in the case of a Pd-Ni catalyst supported on MWCNTs.[44] A number of theoretical studies have been carried out to elucidate the kinetics and energetics of hydrogen

spillover. Density functional theory (DFT) calculations have shown evidence for the transfer of hydrogen atoms from metal nanoparticles to an adsorbent surface.[45-49]

2.5 Effects of Surface Area on Hydrogen Storage

High surface area carbon materials are promising for the low-temperature storage of hydrogen via physisorption, where surface area is a critical structural parameter of porous adsorbent materials. Linear relationships between hydrogen storage capacity and surface area have been observed for the family of carbon based adsorbents. This is because an adsorbent that possesses a higher surface area provides additional available/accessible surface sites per sample mass. Among activated carbons, commercially available super-activated carbons (e.g., AX-21 and Maxsorb possessing surface areas of 2800 $m^2 g^{-1}$ and 3300 $m^2 g^{-1}$, respectively) at room temperature have exhibited high hydrogen storage capacities of ~0.6 and 0.67 Wt.% at 10 MPa.[50] Chemically activated carbon with hydrogen adsorption capacities of 1.2 and 2.7 Wt.% have been obtained at 20 and 50 MPa at 298K, whereas at 77 K, the level of hydrogen adsorption was dependant on the surface area and the total micropore volume of the activated carbon. Hydrogen adsorption capacities of 5.6 Wt.% at 4 MPa and 77 K have been attained by chemically activated carbons,[51] where the surface area of mesoporous carbon was increased from 833 to 2700 $m^2 g^{-1}$, subsequent to KOH activation.[52] The trend of H_2 uptake vs surface area revealed that hydrogen storage via graphene materials did not exceed 1 Wt.% at 12 MPa H_2 at ambient temperature. A linear increase in hydrogen adsorption vs surface area was observed at 77 K with a maximal observed value of ~5 Wt.% for a 2300 m^2/g sample. It may be concluded that bulk graphene samples, obtained through the use of graphite oxide exfoliation and activation, follows the standard of other nanostructured carbon hydrogen uptake trends and do not demonstrate hydrogen storage parameters as have been reported in several previous studies. Nevertheless,

graphene remains as one of the optimal materials for the physisorption of hydrogen, particularly at low temperatures.[53] Most studies on MOF storage capacity have been focused at 77 K, and significant storage capacities were achieved on MOFs with high surface areas. MOF-177 with a surface area of 4500 $m^2 g^{-1}$ has the capacity to store 7.5 Wt.% H_2 at 7 MPa. MOF-210 with the highest surface area (6240 $m^2 g^{-1}$) can store 7.9 Wt.% at 5 MPa. At room temperature, however, the storage capacities of MOFs were substantially lower. MOF-177 and UMCM-2 were reported to store 0.6 Wt.% and 0.8 Wt.% hydrogen, respectively, at 10 MPa. A common feature for the storage performance of MOFs at both cryogenic and ambient temperatures was that higher surface areas led to higher storage capacities. Hydrogen storage capacities are also influenced by more complex factors, such as doping methods, metal particle size and distribution, as well as interfacial contacts between the metals and supports.[54]

2.6 Hydrogen Spillover in Pd-based Nanostructured Materials

As support materials, carbon based adsorbents have garnered much attention due to their attributes, including that they are lightweight, have high surface areas, tailorable structures, and hold potential for diverse applications due to their intriguing electrical, mechanical, and optical properties.[55-57] In recent years, there has been a rapidly developing research thrust in the area of hydrogen storage through spillover on carbons, via the addition of catalysts. A fundamental understanding is required as relates to factors that affect both H_2 spillover and hydrogen storage capacities, as well as strategies for improving storage performance.[58] One of the primary challenges toward the realization of solid state hydrogen storage is that the storage capacity of adsorbents is significantly lower at ambient temperatures than at cryogenic temperatures.[59] A survey of commercial microporous carbon materials for hydrogen storage was carried out by Zlotea et al., which revealed that for similar adsorbents, synthesis procedures and pre-treatment

might lead to significant differences in adsorption capacity. It was learned that even for identical samples from the same source, different laboratories obtained dissimilar results due to variances in measurement methodologies and analytical procedures.[60] For instance, reports on hydrogen uptake of CNTs are much controversy. A 4.2 wt.% of H_2 storage capacity for purified SWCNTs under a pressure of 10-MPa and at room temperature was reported by Liu et al. in 1999,[61] which was much higher than that they reported in 2010 (less than 1.7 wt.%).[62] The overestimated H_2 storage capacity was mainly due to the limited amount and nonuniformity of CNT samples, poor understanding on the intrinsic characteristics and influence of temperature fluctuations and sample volume on the measured hydrogen storage capacity, and improper measurement equipment and methodology employed at the initial stages of the studies on hydrogen uptake in CNTs as described by the authors.[62] The robustness of interactions through which hydrogen is bound within materials is a key constraint to tunability, as is the structural-chemical control over the rate at which hydrogen is taken up and released.

Nanoporous carbonaceous materials may serve as convenient “hosts” in which they are useful for the storage, separation, and investigation of various sequestered molecules under strong confinement. Novel carbon-based nanomaterials, such as carbon nanofibers (CNF), carbon nanotubes (CNT), single-walled carbon nanotubes (SWNTs), double-walled carbon nanotubes (DWNTs), multiwalled carbon nanotubes (MWNTs), doped fullerenes and ordered porous carbons have been regarded as promising media for the efficient reversible storage and separation of chemical species.[63] At room temperature, CNF decorated with Pd nanoparticles have achieved hydrogen storage capacities approaching 0.59 and 1.38 Wt.% at 9 and 7.7 MPa, respectively.[64,65] Various classes of CNTs have been employed as support materials, with Pd as the catalyst, where hydrogen storage capacities varied from 0.035 to 4.5 Wt.% of hydrogen.[66-70] With PdNi and PdPt

serving as catalysts on MWNT supports at room temperature, the hydrogen sorption capacities were 2.3 and 2.0 Wt.% at 1.5 and 2 MPa.[71,72] A maximum hydrogen storage capacity of 0.7 Wt.% was obtained at 9 MPa at 298 K in a Pd loaded MAXSORB sample, while the capacities for raw carbon nanotubes and MAXSORB under the same pressure were 0.21 and 0.42 Wt.%., respectively.[68] A Pd doped graphene carbon composite demonstrated a storage capacity of 0.82 Wt.% of hydrogen at 8MPa under 298 K.[73] Several studies have been conducted using different types of porous carbon materials at close to room temperature, under different pressures; however, to date none of these materials have attained the high capacities that have been set for vehicular hydrogen storage.[74-82] Recent work in our group has shown that PdCd and PdCdAg catalysts on PAC200 substrates exhibited enhanced hydrogen storage capacities, which were achieved at room temperature under ambient pressure.[29,74]

MOFs have become of great interest due to their broad range of potential applications, particularly in the field of heterogeneous catalysis, and for gas storage.[83,84] These nanomaterials have provided enticing solutions to the hydrogen storage problem due to the physisorptive nature of their interactions. The rapid release kinetics of MOFs has served to sustain their stature as a frontrunner for hydrogen storage. Advances in bridging the gaps between physi- and chemisorptive materials, such as metal hydrides, have also provided dramatic boosts in hydrogen uptake capacities, thus providing researchers with even more exciting work for the future. Enhanced storage capacities coupled with rapid hydrogen uptake have been demonstrated with Pd nanocrystals, encapsulated within a HKUST-1 (copper (II) 1,3,5-benzenetricarboxylate) MOF, which was double the storage capacity of bare Pd nanocrystals. The kinetics of hydrogen absorption within the Pd nanocrystals was also enhanced by the MOF coating.[85] In the case of MOFs, the dimensions of Pd nanoparticles have an impact on hydrogen uptake.[86] The

insertion of Pd nanoparticles into the MOF 101 (Cr) pores, while simultaneously ensuring good contact, resulted in the ambient temperature hydrogen uptake of the framework due to the formation of palladium hydride.[87] By solution infiltration of Pd into MOF-5, the surface area was decreased from 2885 $m^2 g^{-1}$ to 958 $m^2 g^{-1}$; however, the hydrogen absorption capacity was increased from 1.15 to 1.85 Wt.%.[88] When MIL-100(Al) was employed as a host for the synthesis of Pd nanoparticles (~2.0 nm) that were embedded within its pores, as described by Zlotea et al.,[89] it exhibited one of the highest metal contents (10 wt %) without the degradation of the porous host. The textural properties of MIL-100(Al) were strongly modified by Pd insertion, leading to significant changes in its gas sorption properties.[89]

The synthesis of Pd nanoparticles within a porous MOF, incorporating redox active organic linkers, was undertaken by Cheon et al.,[90] by simple immersion of the MOF solid. Here, the hydrogen storage capacity was dependant on the volume of Pd nanoparticles that were loaded within the MOF for the duration of immersion. The hydrogen capacities are reported were far lower than reported by other methods.[90] Recent work by Kalidindi et al.,[91] has shown that COFs are new class of templates for metal nanoparticles, as they have synthesized a three-dimensional covalent Pd@COF-102 hybrid material. The Pd@COF-102 hybrid material is a rare example of a metallic nanoparticle-loaded porous crystalline material that has a narrow size distribution without the presence of larger agglomerates. At room temperature, the uptake of these samples was superior to that of similar systems, such as Pd@MOFs. Studies indicated that the H_2 capacities were enhanced by a factor of 2–3 through impregnation with Pd on COF-102 at room temperature under a pressure of 20 bars. The significantly higher reversible hydrogen storage capacity that comes from decomposed products of the employed organometallic Pd precursor suggests that this discovery may be relevant to the spillover phenomenon in metal/MOFs and related systems.[91]

Pd doped double-walled silica nanotubes show promise as a hydrogen storage material at room temperature.[92] Similar work by Chen et al.,[93] has shown that when titanium dioxide nanotubes were used as support materials, improved hydrogen sorption was observed.[93] Studies on new boron and nitrogen based hydrides illustrate how hydrogen release and uptake properties may be improved.[94] Several works have been carried out with graphene as a support materials using Pd as a catalyst for hydrogen storage.[78,95-98] Among these, nitrogen doped Pd decorated graphene exhibited very high hydrogen capacities of up to 4.4 Wt.% at 298 K and 4 MPa.[95] Very recent work by Zhong et al.,[99] have proposed three dimensional carbon aerogel (CA) as a promising support material for hydrogen uptake. The effects of different Pd loads on the hydrogen uptake capacities of CAs were investigated, where the results showed that Pd doping imparted a negative effect on hydrogen uptake capacity at 77 K. At 298 K, the hydrogen uptake capacity was contingent on the Pd content and nanoparticle size in the low pressure region (<1 MPa). The hydrogen uptake capacity of the 4.8 Wt.% Pd/CA was ~0.11 Wt.% at 1MPa and 298 K. At higher pressures (>1 MPa), the pore volume controls the capacity for hydrogen uptake.[99]

Significant improvements in hydrogen storage capacities have been achieved at ambient temperatures and pressure via the hydrogen spillover effect by design and utilization of nanostructured materials. A summary of the hydrogen spillover and storage capacities of Pd based nanomaterials is shown in Table 2.1. It is recommended that several aspects including catalysts and supports with high surface areas should be further developed to improve hydrogen storage capacity by spillover.

Table 2.1. Metal hydrides and their hydrogen spillover and storage properties.

Metal Catalyst	Catalyst in (Wt.%)	Support	Surface area (m^2/g)	T (K)	P (MPa)	Wt.% of H	Ref
Pd	3	CNF	150	298	9	0.59	64
Pd	2	CNF	-	298	7.7	1.38	65
Pd	-	CNT	-	298	0.1	7	66
Pd	-	CNT	89	298	5	0.87	67
Pd	31.5	SWNT	232	298	9	0.51	68
Pd	2	DWNT	209	298	3	2.0	69
Pd	20	CNT	-	298	10.7	3.5-4.5	70
$PdNi_{18}$	5.5	MWNT	-	298	1.5	2.3	71
PdPt	-	MWNT	212	298	2	2.0	72
Pd	49	Maxsorb AC	199	298	9	0.7	68
Pd/GS	-	AC	3328	298	8	0.82	73
Pd	-	AC-ox1	824	298	8	0.37	75
Pd	2	ACF	1878	298	2	0.23	76
Pd	10	AC	-	303	5	0.53	77
Pd	10	AX-21	2466	298	10	1.38	78
Pd	10	AX-21-O	2362	298	10	0.98	78
Pd	18.4-24.5	C-nanosheet	80-230	298	0.11	0.1-0.26	79
Pd	10	OMC	342	298	30	0.80	80
Pd/Ni	10.2/6.5	TC	874	298	0.5	0.027	81
Pd	10	TC	712	298	0.5	0.05-0.08	82
Pd	-	MIL 101 (Cr)	-	298	4.5	0.23	87
Pd	1	MOF-5	958	77	0.1	1.86	88
Pd	10	MIL-100 (Al)	380	77	4	1.3	89
Pd	3	MOF	242	298	9.5	0.3	90
Pd	9.5	COF-102	1419	298	2	0.42	91
Pd	5,10,15	SN	160-264	298	3.5	0.15-1.9	92
Pd	10	GO	687	298	10	0.95	78
Pd	20	N-HEG	-	298	4	4.4	95
Pd	-	HCS	150	298	2.4	0.36	96
Pd	-	N-Graphene	146	298	2	1.9	97
Pd	1	g-C_3N_4	26	298	4	2.6	98
Pd	4.8	CA	499	298	1	0.11	99

2.7 Oxygen Reduction Reaction

The potential applications of fuel cells are extensive as they have the capacity to provide clean energy and sustainable power.[100] Fuel cells directly utilizes fuels (e.g., hydrogen, methanol, formic acid) and oxygen and effectively convert their chemical energy into electricity with a high power density.[101] The difficult challenges associated with fuel cells relate to the development of highly active electrocatalysts to reduce the high overpotential at the cathode during the ORR.[102]

Platinum (Pt) is considered as one of the preeminent electrocatalysts for ORR. Unfortunately, the limited availability and expense of Pt are major constraints that limit its wide commercial applications.[103] There have been significant advancements made in the elucidation of ORR on Pt-based nanomaterials; however, they still struggle with severe stability and consistency issues, together with crossover and poisoning effects in the cathodic compartments of the direct methanol fuel cell, which result in a decrease in the performance of the catalysts.[104] Therefore, it is necessary to identify alternate new materials and methodologies to overcome costs related issues and to enhance the catalytic performance of electrocatalysts.[105]

Graphitic carbon nitride (g-C_3N_4) has a planar structure, similar to graphite.[106] It includes both pyridinic and graphitic nitrogen moieties, where each C atom is connected to three N atoms. Additionally, g-C_3N_4 may be facilely produced at a large scale with low cost. Recent studies have shown that C_3N_4 is an effective photocatalyst with enhanced visible light response.[107] In contrast, the activity of C_3N_4 as an electrocatalyst for ORR was observed to be very low due to its poor conductivity. To further enhance the electrocatalytic activity of g-C_3N_4, different carbon-based materials are integrated as a co-support; meanwhile, metal nanomaterials are employed as catalysts to improve charge-transfer as well as the electrochemical behaviour of carbon nitrides.[108]

Pd based nanomaterials have gained remarkable attraction in miscellaneous research studies, comprising catalysis and sensors.[109, 110] It may serve as an attractive alternative in the development of non-platinum catalysts with catalytic activity similar to Pt.[111] Recent studies have shown that the active sites for ORR strongly depend on the surface structure of Pd. Kondo et al.[112] have shown that the Pd(100) electrode surface exhibited over three times increase in current density in comparison with the Pt(110) surface for ORR.[112] It was reported that in acidic media, pure Pd activity is higher than that of all other noble metals, except Pt; however, the tendency of Pd dissolution in acidic media decreases the stability of the electrode. On the other hand, it is known that in alkaline solutions Pd exhibits high stability and electrocatalytic activity toward ORR due to a reduced anion poisoning effect.[113] Density functional theory (DFT) calculations based on oxygen adsorption and vacancy formation energies indicated that the use of Pd as a co-catalyst might play an important role in ORR in case of catalytic behaviour as well as long-term stability.[114]

2.8 Summary and Outlook

Hydrogen storage by spillover is an atomic hydrogen adsorption process, where the surface adsorption sites of the adsorbent determine the storage capacity. It is understood that an adsorbent that possesses a higher number of surface adsorption sites for hydrogen atoms, should have a higher hydrogen spillover capacity. In this regard, carbonaceous compounds are one of the most studied classes of materials. To date, however, at ambient temperature and pressure, the hydrogen storage capacity of carbonaceous materials is still below the DOE onboard vehicular targets. Although the optimization of surface area and pore size may improve hydrogen storage at ambient temperature, actual developments may not be possible through the modification of structural properties alone. An auspicious strategy for enhancing the strength of the interaction of hydrogen with sorbents at ambient temperatures and pressures may be attained by the doping of carbon,

MOFs, COFs and other nanostructured materials with metallic nanoparticles that are capable of promoting spillover. However, more fundamental research and the development of advanced techniques are required to completely understand the kinetics of hydrogen spillover and oxygen reduction as it relates to sustainable hydrogen economy.

References

1. N. L. Garland, D. C. Papageorgopoulos. J. M. Stanford. Hydrogen and fuel cell technology: progress, challenges, and future directions. *Energy Procedia* **2012**, 28, 2–11.

2. A. Chen, P. Holt-Hindle. Platinum-based nanostructured materials: synthesis, properties, and applications. *Chem. Rev.* **2010**, 6, 3767-3804.

3. L. Schlapback. Technology: hydrogen-fuelled vehicles. *Nature* **2009**, 460, 809−811.

4. A. Züttel. Materials for hydrogen storage. *Mater. Today* **2003**, 6, 24-33.

5. U. Eberle, M. Felderhoff, F. Schüth. Chemical and physical solutions for hydrogen storage. *Angew. Chem. Int. Edit*. 48 **2009**, 48, 6608−6630.

6. I. P. Jain, P. Jain, A. Jain. Novel hydrogen storage materials: a review of lightweight complex hydrides. *J. Alloy Compd*. 503 (2) (2010) 303-339.

7. M. D. Paster. R. K. Ahluwalia, G. Berry, A. Elgowainy, S. Laesher, K. McKenney, M. Gardiner. Hydrogen storage technology options for fuel cell vehicles: wee-towheel costs, energy efficiencies, and greenhouse gas emissions. *Int. J. Hydrogen Energ.* **2011**, 36, 14534−14551.

8. Targets for onboard hydrogen storage systems for light-duty vehicles, US department of energy (DOE). (Office of energy efficiency and renewable energy and the freedomCAR and fuel partnership) September **2009**.

9. Y. Jia, C. Sun, S. Shen, J. Zou, S. S. Mao, X. Yao. Combination of nanosizing and interfacial effect: future perspective for designing Mb-based nanomaterials for hydrogen storage. *Renew Sust. Energ Rev.* **2015,** 44, 289-303.

10. B. Sakintuna, F. L. Darkrim, M. Hirscher. Metal hydride materials for solid hydrogen storage: a review. *Int. J. Hydrogen Energ.* **2007**, 32, 1121-1140.

11. R. Prins. Hydrogen spillover. Facts and fiction. *Chem. Rev*. **2012**, 112, 2714-2738.

12. H. Reardon, J. M. Hanlon, R. W. Hughes, A. G. Jopek, T. K. Mandal, D. H. Gregory. Emerging concepts in solid state hydrogen storage; the role of nanomaterials design. *Energ. Environ Sci.* **2012**, 5, 5951-5979.

13. A. Chen. Electrocatalysis and photoelectrochemistry based on functional nanomaterials. *Can. J. Chem*. **2014**, 92, 581-597.

14. B. D. Adams, R.M. Asmussen, C. K. Ostrom, A. Chen. Synthesis and comparative study of nanoporous palladium-based bimetallic catalysts for formic acid oxidation. *J. Phys. Chem. C* **2014**, 118, 29903-29910.

15. B. D. Adams, A. Chen. The role palladium in a hydrogen economy. *Mater. Today* **2011**, 14, 282-289.

16. A. Baldi, T. C. Narayan, A. L. Koh, J. A. Dionne. In situ detection of hydrogen-induced phase transitions in individual palladium nanocrystals. *Nat Mater*. **2014**, 13, 1143-1148.

17. P. Chen, M. Zhu. Recent progress in hydrogen storage. *Mater. Today* **2008**, 11, 36-43.

18. M. Yamauchi, H. Kobayashi, H. Kitagawa. Hydrogen storage mediated by Pd and Pt nanoparticles. *Chem. Phys. Chem*. **2009**, 10, 2556-2576.

19. R. Bardhan, A. M. Ruminski, A. Brand, J. J. Urban. Magnesium nanocrystals-polymer composites: a new platform for designer hydrogen storage. *Energ. Environ Sci*. **2011**, 4, 4882-4895.

20. M. Yamauchi, R. Ikeda, H. Kitagawa, M. Takata. Nanosize effects on hydrogen storage in palladium. *J. Phys. Chem. C* **2008**, 112. 3294-3299.

21. Z. N. Xu, J. Sun, C. S. Lin, X. M. Jiang, Q. S. Chen, S. Y Peng, M. S. Wang, G. C. Guo. High-performance and long-lived Pd nanocatalyst directed by shape effect for CO oxidative coupling to dimethyl oxalate. *ACS Catal*. **2013**, 3, 118-122.

22. D.-T. Phan, G.-S. Chung. Effects of Pd nanocube size of Pd nanocube-graphene hybrid on hydrogen sensing properties. *Sensors Actuat. B: Chem.* **2014**, 204, 437-444.

23. G. Li, H. Kobayashi, S. Dekura, R. Ikeda, Y. Kubota, K. Kato, M. Takata, T. Yamamoto, S. Matsumura, H. Kitagawa. Shape-dependent hydrogen storage properties in Pd nanocrystals: which does hydrogen transfer prefer, octahedron (111) or cube (100). *J. Am. Chem. Soc.* **2014**, 136, 10222−10225.

24. B. D. Adams, G. Wu, S. Nigro, A. Chen. Facile synthesis of Pd-Cd nanostructures with high capacity for hydrogen storage. *J. Am. Chem. Soc.* **2009**, 131, 6930-6931.

25. B. D. Adams, C. K. Ostrom, A. Chen. Hydrogen electrosorption into Pd-Cd Nanostructures. *Langmuir* **2010**, 26, 7632-7637.

26. K. Kusada, H. Kobayashi, R. Ikeda, Y. Kubota, M. Takata, S. Toh, T. Yamamato, S. Matsumura, N. Sumi, K. Sato, K. Nagaoka, H. Kitagawa. Solid solution alloy nanoparticles of immiscible Pd and Ru elements neighbouring on Rh: changeover of the thermodynamic behavior for hydrogen storage and enhanced co-oxidizing ability. *J. Am. Chem. Soc.* **2014**, 136, 1864-1871.

27. M. D. Ong, B. W. Jacobs, J. d. Sugar, M. E. Grass, Z. Liu, G. M. Buffleben, W,. M. Cliff, M. E. Langham, P. J. Cappillino, D. B. Robinson. Effect of rhodium distribution on thermal stability of nanoporous palladium-rhodium powders. *Chem. Mater*. **2012**, 24, 996-1004.

28. S. Chen, B. D. Adams, A. Chen. Synthesis and electrochemical study of nanoporous Pd-Ag alloys for hydrogen sorption. *Electrochim. Acta* **2010**, 56, 61-67.

29. C. K. Ostrom, A. Chen. Synthesis and electrochemical study of trimetallic nanoparticles for enhanced hydrogen storage. *J. Phys. Chem. C* **2013**, 117, 20456-20467.

30. T. Hongo, K. Edalati, H. Iwaoka, M. Arita, J. Matsuda, E. Akiba, Z. Horita. High-pressure torsion of palladium: hydrogen-induced softening and plasticity in ultrafine grains and hydrogen-induced hardening and embrittlement in coarse grains. *Mater Sci. Eng. A* **2014**, 618, 1–8.

31. S. Khoobiar. Particle to particle migration of hydrogen atoms on Platinum-alumina catalysts from particle to neighbouring particles. *J. Phys. Chem*. **1964**, 68, 411-412.

32. M. Boudart, M.A. Vannice, J.E. Benson, Adlineation, portholes and spillover. *Z. Phys. Chem. Neue. Folge*. **1969**, 64, 171-177.

33. U. Roland, T. Braunschweig, F. Roessner. On the nature of spilt-over hydrogen. *J. Mol. Catal. A: Chem*. **1997**, 127, 61-84.

34. W.C. Conner, Jr. J.L. Falconer. Spillover in heterogeneous catalysis. *Chem. Rev*. **1995**, 95, 759-788.

35. Y. Hao, x. Wang, N. Perret, F. C. Lizana, M. A. Keane. Support effect in the gas phase hydrogenation of butyronitrile over palladium. *Catal. Struc. Reactivity* **2015**, 1, 4-10.

36. H. Zhou, J. Zhang, X.-F. Yan, X.-P. Shen, A.-H. Yuan. Spillover enhanced hydrogen storage on Pt-doped MOF/graphene oxide composite produced via an impregnation method. *Inorg. Chem. Commun*. **2015**, 54, 54-56.

37. D. D. Do, S. L. Johnathan, Y. Zeng, C. Fan, V. T. Nguyen, T. Horikawa, D. Nicholson. The interplay between molecular layering and clustering in adsorption of gases on graphitized thermal carbon black–spill-over phenomenon and the important role of strong sites. *J. Colloid. Interf. Sci*. **2015**, 446, 98–113.

38. A. J. Lachawiec, Jr. G. Qi, R.T. Yang. Hydrogen storage in nanostructured carbons by spillover: bridge-building enhancement. *Langmuir* **2005**, 21, 11418-11424.

39. V. V. Bhat, C.I. Contescu, N.C. Gallego. The role of destabilization of palladium hydride in the hydrogen uptake of Pd-containing activated carbons. *Nanotechnology* **2009**, 20, 204011-204020.

40. C. I. Contescu, C. M. Brown, Y. Liu, V. V. Bhat, N. C. Gallego. Detection of hydrogen spillover in palladium-modified activated carbon fibers during hydrogen adsorption. *J. Phys. Chem. C* **2009**, 113 5886–5890.

41. C.-S Tsao, Y. Liu, H.-Y. Chuang, H.-H. Tseng, T.-Y. Chen, C.-H. Chen, M.-S. Yu, Q. Li, A. Lueking, S.-H Chen. Hydrogen spillover effect of Pt-doped activated carbon studied by inelastic neutron scattering. *J. Phys. Chem. Lett***. 2011**, 2, 2322–2325.

42. A. J. Lachawiec, Jr. R.T. Yang. Isotope tracer study of hydrogen spillover on carbon-based adsorbents for hydrogen storage. *Langmuir* **2008**, 24 6159-6165.

43. C.-Y Wang, J. L. Gray, Q. Gong, Y. Zhao, J. Li, E. Klontzas, G. Psofogiannakis, G. Froudakis, A. D. Leuking. Hydrogen storage with spectroscopic identification of chemisorption sites in Cu-TDPAT via spillover from a Pt-activated carbon catalyst. *J. Phys. Chem. C* **2014**, 118, 26750−26763.

44. L. Gao, E. Yoo, J. Nakamura, W. Zhang, H. T. Chua. Hydrogen storage in Pd-Ni doped defective carbon nanotubes through the formation of CH_X ($X = 1, 2$). *Carbon* **2010**, 48 3250–3255.

45. Q. Li, H. Wang, H. Xia, S. Wei, j. Yang. Density functional study of hydrogen adsorption and diffusion Ni-doped graphene and graphene oxide. *Int. J. Quantum Chem*. **2014**, 114, 879–884.

46. O. V. Pupysheva, A.A. Farajian, B.I. Yakobson. Fullerene nanocage capacity for hydrogen storage. *Nano. let*. **2008**, 8 767-774.

47. N. Park. S. Hong, G. Kim, S.-H. Jhi. Computational study of hydrogen storage characteristics of covalent-bonded graphenes. *J. Am. Chem. Soc*. **2007**, 129, 8999-9003.

48. E. Ganz, M. Dornfeld. Energetics and thermodynamics of the initial stages hydrogen storage by spillover on prototypical metal-organic framework and covalent-organic framework materials. *J. Phys. Chem. C* **2014**, 118, 5657−5663.

49. J.-H. Guo, H. Zhang, Y. Tang, X. Cheng. Hydrogen spillover mechanism on covalent organic frameworks as investigated by initio density functional calculation. *Phys. Chem. Chem. Phys*. **2013**, 15, 2873-2881.

50. L. Wang. N.R. Stuckert, H. Chen, R. T. Yang. Effects of Pt particle size on hydrogen storage on Pt-doped metal organic framework IRMOF- 8. *J. Phys. Chem. C* **2011**, 115, 4793-4799.

51. M. Jorda´-Beneyto, F. Suarez-Garcia, D. Lozano-Castello, D. Cazorla-Amoros, A. Linarwes-Solano. Hydrogen storage on chemically activated carbons and carbon nanomaterials at high pressures. *Carbon* **2007**, 45, 293–303.

52. M. Choi, R. Ryoo. Mesoporous carbons with KOH activated framework and their hydrogen adsorption. *J. Mater. Chem*. **2007**, 17, 4204-4209.

53. A. G. Klechikov, G. Mercier, P. Merino, S. Blanco, C. Merino, A. V. Talyzin. Hydrogen storage in bulk graphene-related materials. *Micropor. Mesopor. Mat*. **2015**, 210, 46-51.

54. L. Wang, A. J, Lachawiec, R. T. Yang. Nanostructured adsorbents for hydrogen storage at ambient temperature: high-pressure measurements and factors influencing hydrogen spillover. *RSC. Adv*. **2013**, 3, 23935–23952.

55. A. D. Lueking, R.T. Yang. Hydrogen spillover to enhance hydrogen storage-study of the effect of carbon physicochemical properties. *Appl. Catal A: Gen*. **2004**, 265, 259–268.

56. Y. Xia, Z. Yang, Y. Zhu. Porous carbon-based materials for hydrogen storage: advancement and challenges. *J. Mater. Chem. A* **2013**, 1, 9365–9381.

57. M. Sevilla, R. Mokaya. Energy storage applications of activated carbons: supercapacitors and hydrogen storage. *Energ. Environ. Sci*. **2014**, 7, 1250-1280.

58. L. Wang, R.T. Yang. Hydrogen storage on carbon-based adsorbents and storage at ambient temperature by hydrogen spillover. *Catal Rev: Sci. Eng*. **2010**, 52, 411-461.

59. J. Yang, A. Sudik, C. Wolvetron, D. J. Siegel. High capacity hydrogen storage materials: attributes for automotive applications and techniques for materials discovery. *Chem. Soc. Rev*. **2010**, 39, 656-675.

60. C. Zlotea, P. Moretto, T. Steriotis. A round robin characterisation of the hydrogen sorption properties of a carbon based material. *Int. J. Hydrogen Energ*. **2009**, 34, 3044-3057.

61. C. Liu, Y. Y. Fan, M.Liu, H. T. Cong, H. M. cheng, M. S. Dresselhaus. Hydrogen storage in single-walled carbon nanotubes at room temperature. *Science* **1999**, 286, 1127-1129.

62. C. Liu, Y. Chen, C.-Z. Wu, S.-T. Xu, H.-M Cheng. Hydrogen storage in carbon nanotubes revisited. *Carbon* **2010**, 48, 452-455.

63 P. Kowalczyk, L. Brualla, A. Zywocinski, S.K. Bhatia. Single-walled carbon nanotube: efficient nanomaterials for separation and on-board vehicle storage of hydrogen and methane mixture at room temperature?. *J. Phys. Chem. C* **2007**, 111, 5250-5257.

64. C.-K. Back, G. Sandi, J. Prakash, J. Hranisavljevic. Hydrogen sorption on palladium-doped sepiolite-derived carbon nanofibers. *J. Phys. Chem. B* **2009**, 110, 16225–16231.

65. M. Marella, M. Tomaselli. Synthesis of carbon nanofibers and measurements of hydrogen storage. *Carbon* **2006**, 44, 1404–1413.

66. A. Reyhani, S. Z. Mortazavi, S. Mirershadi, A. Z. Moshfegh. P. Parvin, A. N. Golikand. Hydrogen storage in decorated multiwalled carbon nanotubes by Ca, Co, Fe, Ni, and Pd nanoparticles under ambient conditions. *J. Phys. Chem. C* **2011**, 115, 6994–7001.

67. K. Wenelska, B. Michalkiewicz, X. Chen, E. Mijowska. Pd nanoparticles with tunable diameter deposited on carbon nanotubes with hydrogen storage capacity. *Energy* **2014**, 75, 549-554.

68. A. Anson, E. Lafuente, E. urriolabeitia, R. Navarro, A. M. Benito, W. K. Maser, M. T. Martinez. Hydrogen capacity of palladium-loaded carbon materials. *J. Phys. Chem. B* **2006**, 110, 6643–6648.

69. H. Wu, D. Wexler, A. R. Ranjibartoreh, H. Liu, G. Wang. Chemical processing of double-walled carbon nanotubes for enhanced hydrogen storage. *Int. J. Hydrogen Energ*. **2010**, 35, 6345–6349.

70. S-C. Mu, H.-L. Tang, S.-H. Qian, M. Pan, R.-Z. Yuan. Hydrogen storage in carbon nanotubes modified by microwave plasma etching and Pd decoration. *Carbon* **2006**, 44, 762–767.

71. J. Ren, S. Liao, J. Liu. Hydrogen storage of multiwalled carbon nanotubes coated with Pd-Ni nanoparticles under moderate conditions. *Chin. Sci. Bull*. **2006**, 51, 2959–2963.

72. S-W. Hwang, S.-U. Rather, M. Naik, C. S. Soo, K.-as. Nahm,. Hydrogen uptake of multiwalled carbon nanotubes decorated with Pt-Pd alloy using thermal vapour deposition method. *J. Alloy Compd*. **2009**, 480, L20–L24.

73. C.-H. Chen, T.-Y. Chung, C.-C. Shen, M.-S. yu, C.-S Tsao, G.-N. Shi, C.-C. Huang, M.-D. Ger, W.-L. Lee. Hydrogen storage performace in palladium-doped graphene/carbon composites. *Int. J. Hydrogen Energ*. **2013**, 38, 3681-3688.

74. B. D. Adams, C. K. Ostrom, S. Chen, A. Chen. High-performance Pd-based hydrogen spillover catalysts for hydrogen storage. *J Phys Chem. C* **2010,** 114, 19875–19882.

75. T.-Y. Chung, C.-S. Tsao, H.-P. Tseng, C.-H. Chen, M.-S. Yu. Effects of oxygen functional groups on the enhancement of the hydrogen spillover of PD-doped activated carbon. *J. Colloid Interf. Sci*. **2015**, 441, 98–105.

76. C. I. Contescu, C. M. brown, Y. Liu, V. V. Bhat, N. C. Gallego, detection of hydrogen spillover in Palladium-modified activated carbon fibers during hydrogen adsorption. *J. Phys. Chem. C* **2009**, 113, 5886–5890.

77. C.-C. Huang, H.-M. Chen, C.-H. Chen. Hydrogen adsorption on modified activated carbon. *Int. J. Hydrogen Energ*. **2010**, 35, 2777–2780.

78. L. Wang, F.H. Yang, R.T. Yang. Effect of surface oxygen groups in carbons on hydrogen storage by spillover. *Ind. Eng. Chem. Res.* **2009**, 48, 2920–2926.

79. Z.-L. Hu. M. Aizawa, Z.-M. Wang, N. Yoshizawa, H. Hatori. Synthesis and characteristics of graphene oxide-derived carbon nanosheets-Pd nanosized particle composites. *Langmuir* **2010**, 26, 6681–6688.

80. D. Saha, S. Deng. Hydrogen adsorption on ordered mesoporous carbon doped with Pd, Pt, Ni, and Ru. *Langmuir* **2009**, 25, 12550–12560.

81. R. Campesi, F. Campesi, E. Leroy, M. Hirscher, R. Gadiou, C. Vix-Guteri, M. Latroche. In situ synthesis and hydrogen storage properties of PdNi alloy nanoparticles in an ordered mesoporous carbon template. *Micropor. Mesopor. Mat.* **2009**, 117, 511–514.

82. R. Campesi, F. Cuevas, R. Gadiou, E. Leroy, M. Hirscher, C. Vix-Guteri, M. Latroche. Hydrogen storage properties of Pd nanoparticle/carbon template composite. *Carbon.* **2008**, 46, 206–214.

83. J. Sculley, D. Yuan, H.-C. Zhou. The current status of hydrogen storage in metal-organic frameworks-updated. *Energy Environ Sci.* **20**11, 4, 2271-2735.

84. C. Rösler, R. A. Fischer. Metal-organic frameworks as hosts for nanoparticles. *Cryst. Eng. Comm.* **2015**, 17,199-217.

85. G. Li, H. Kobayashi, J. M. Taylor, R. Ikeda, Y. Kubota, K. Kato, M. Takata, T. Tomokazu, S. Toh, S. Matsumura, H. Kitagawa. Hydrogen storage in Pd nanocrystals covered with a metal-organic framework. *Nat. Mater.* **2014**, 13, 802-806.

86. I. Gutiérrez, E. Díaz, S. Ordóñez. Consequences of cavity size palladium addition on the selective hydrogen adsorption in isoreticular metal-organic frameworks. *Thermochimica. Acta* **2013**, 567, 79-84.

87. P. A´. Szila´gyi, E. Callini, A. Anastasopol, C. Kwakernaak, S. Sachdeva, R. Van de krol, H. Geerlings, A. Borqschulte, A. Zuttel, B. Dam. Probing hydrogen spillover in Pd@MIL-101(Cr) with a afocus on hydrogen chemisorption. *Phys. Chem. Chem. Phys*. **2014**, 16, 5803-5809.

88. M. Sabo, A. Henschel, H. Frode, E. Klemm, S. Kaskel. Solution infiltration of palladium into MOF-5: synthesis, physisorption and catalytic properties. *J. Mater. Chem*. **2007**, 17, 3827–3832.

89. C. Zlotea, R. Campesi, F. Cuevas, E. Leroy, P. Dibandjo, C. Volkringer, T. Loiseau, G. Férey, M. Latroche. Pd nanoparticles embedded into a metal-organic framework: synthesis, structural characteristics, and hydrogen sorption properties. *J. Am. Chem. Soc*. **2010**, 132, 2991–2997.

90. Y. E. Cheon, M.P. Suh. Enhanced hydrogen storage by palladium nanoparticles fabricated in a redox-active metal-organic framework. *Angew. Chem. Int. Edit*. **2009**, 48, 2899–2903.

91. S. B. Kalidindi, H. Oh, M. Hirscher, D. Esken, C. Wiktor, S. Turner, G. Van Tendeloo, R. A. Fischer. Metal@COFs: covalent organic frameworks as templates for Pd nanoparticles and hydrogen storage properties of Pd@COF-102 hybrid material. *Chem. Eur. J*. **2012**, 18, 10848 – 10856.

92. J. H. Jung, J. A. Rim, S. J. Lee, S. J. Cho, S. Y. Kim, J. K. Kang, Y. M. Kim, Y. J. Kim. Pd-doped double-walled silica nanotubes as hydrogen storage material at room temperature. *J. Phys. Chem. C* **2007**, 111, 2679–2682.

93. S. Chen, C. Ostrom, A. Chen. Functionalization of TiO_2 nanotubes with palladium nanoparticles for hydrogen sorption and storage. *Int. J. Hydrogen Energ*. **2013**, 38, 14002-14009.

94. L. H. Jepsen, M. B. Ley, Y.-S. Lee, Y. W. Cho, M. Dornheim, J. O. Jensen, Y. Filinchuk, J. E. Jorgensen, F. Besenbacher, T. R. Jensen. Boron-nitrogen based hydrides and reactive composites for hydrogen storage. *Mater. Today* **2014**, 17, 130-135.

95. V. B. Parambhath, R. Nagar, S. Ramaprabhu. Effect of nitrogen doping on hydrogen storage capacity of palladium decorated graphene. *Langmuir* **2012**, 28, 7826−7833.

96. K. Wenelska, B. Michalkiewicz, J. gong, T. tang, R. Kalenczuk, X. Chen, E. Mijowska. In situ deposition of Pd nanoparticles with controllable diameters in hollow carbon spheres for hydrogen storage. *Int. J. Hydrogen Energ*. **2013**, 38, 16179-16184.

97. B. P. Vinayan, K. Sethupathi, S. Ramaprabhu. Facile synthesis of triangular shaped palladium nanoparticles decorated nitrogen doped graphene and their catalytic study for renewable energy applications. *Int. J. Hydrogen Energ*. **2013**, 38, 2240-2250.

98. A. A. S. Nair, R. Sundara, N. Anitha. Hydrogen storage performance of palladium nanoparticles decorated graphitic carbon nitride. *Int. J. Hydrogen Energ*. **2015**, 40, 3259-3267.

99**.** M. Zhong, Z. Fu, L. Yuan, H. Zhao, J. Zhu, Y. He, C. Wang, Y. Tang. A solution-phase synthesis method to prepare Pd-doped carbon aerogels for hydrogen storage. *RSC. Adv*. **2015**, 5, 20966–20971.

100. L. Dai, Y. Xue, L. Qu, H.-J. Choi, J.-B. Baek. Metal-free catalysts for oxygen reduction reaction. *Chem. Rev.* **2015,** 115, 4823-4892.

101. M. del Cueto, P. Ocón, J. M. L. Poyato. Comparative study of oxygen reduction reaction mechanism on nitrogen-, phosphorus-, and boron-doped graphene surfaces for fuel cell applications. *J. Phys. Chem. C* **2015,** 119, 2004-2009.

102. M. Govindhan, A. Chen. Simultaneous synthesis of gold nanoparticle/graphene nanocomposite for enhanced oxygen reduction reaction. *J. Power. Sources* **2015,** 274, 928-936.

103. C. Sealy. The problem with platinum. *Mater. Today* **2008,** 11, 65-68.

104. N. Zhang, H. Yan, X. Chen, L. An, Z. Xia, D. Xia. Origins for the synergetic effects of $AuCu_3$ in catalysis for oxygen reduction reaction. *J. Phys. Chem. C* **2015,** 119, 907-912.

105. Y. Holade, N. E. Sahin, K. Servat, T. W. Napporn, K. B. Kokoh. Recent advances in carbon supported metal nanoparticles preparation for oxygen reduction reaction in low temperature fuel cells. *Catalysts* **2015,** 5, 310-348.

106. S. M. Lyth, Y. Nabae, S. Moriya, S. Kuroki, M.-a. Kakimoto, J.-i. Ozaki, S. Miyata. Carbon nitride as a nonprecious catalyst for electrochemical oxygen reduction. *J. Phys. Chem. C* **2009,** 113, 20148-20151.

107. M. Xu, L. Han, S. Dong. Facile fabrication of highly efficient g-C_3N_4/Ag_2O heterostructured photocatalysts with enhanced visible-light photocatalytic activity. *ACS Appl. Mater. Interfaces* **2013,** 5, 12533-12540.

108. A. Chen, C. Ostrom. Palladium-based nanomaterials: synthesis and electrochemical applications. *Chem. Rev.* **2015,** 115, 11999-12044.

109. S. K. Konda, C. K. Ostrom, A. Chen. Synthesis and electrochemical study of Cd@Pd core/shell nanomaterials for hydrogen sorption and storage. *Int. J. Hydrogen. Energ.* **2015,** 40, 16365-16374.

110. L. Arroyo-Ramírez, R. Montano-Serrano, T. Luna-Pineda, F. R. Román, R. G. Raptis, C. R. Cabrera, Synthesis and characterization of palladium and palladium–cobalt nanoparticles on vulcan XC-72R for the oxygen reduction reaction. *ACS Appl. Mater. Interfaces* **2013,** 5, 11603-11612.

111. J. S. Jirkovský, A. Björling, E. Ahlberg. Reduction of oxygen on dispersed nanocrystalline CoS_2. *J. Phys. Chem. C* **2012,** 116, 24436-24444.

112. S. Kondo, M. Nakamura, N. Maki, N. Hoshi. Active sites for the oxygen reduction reaction on the low and high index planes of palladium. *J. Phys. Chem. C* **2009,** 113, 12625-12628.

113. W.-P. Zhou, K. Sasaki, D. Su, Y. Zhu, J. X. Wang, R.R. Adzic, Gram-scale-synthesized Pd_2Co-supported Pt monolayer electrocatalysts for oxygen reduction reaction. *J. Phys. Chem. C* **2010,** 114, 8950-8957.

114. S. J. Hwang, S. J. Yoo, J. Shin, Y.-H.Cho, J. H. Jang, E. Cho, Y.-E. Sung, S. W. Nam, T.-H. Lim, S.-C. Lee, S.-K. Kim. Supported core@shell electrocatalysts for fuel cells: close encounter with reality. *scientific reports* **2013,** 3, 1309.

Chapter 3: Materials and Methods

3.1 Introduction

An overview of Pd-based nanomaterials that may be employed in hydrogen storage and oxygen reduction reaction were presented in previous chapters, as well as a discussion of the underlying challenges for commercial applications. In this chapter, the main experimental methodologies and techniques employed to synthesize and characterize materials will be described briefly. Details of the experimental procedures and equipment pertaining to each specific study are presented in Chapters 4-8.

3.2 Experimental

3.2.1 Materials

Sulfuric acid (99.999%); potassium hydroxide; sodium acetate; sodium borohydride (≥98%); $Pd(NO_3)_2$; $Cd(NO_3)_2$ (≥99%); 2-propanol (≥99.5%); graphene oxide (4mg/mL); urea (99.99%); methanol 50% (v/v), and Nafion® perfluorinated ionexchange resin (10 wt.% dispersion in water), were purchased from Sigma-Aldrich.

Palladium foil with a thickness of 0.55 mm were received from Sigma-Aldrich and were cut into 0.5 cm x 0.5 cm squares. Pt wire (99.9%, 0.5 mm diameter) were used as received from Alfa-Aesar. Rotating disc glassy carbon electrodes (RDGCEs) with surface area of 0.1964 cm^2 were purchased from Pine Research Instrumentation.

The water was purified with the NANOpure® DiamondTM UV ultrapure water purification system and used for cleaning purposes and the preparation of all samples and solutions. Gases utilised in this thesis are ultrapure argon (99.99%) and hydrocarbon free Oxygen (99.99%).

3.2.2 Instruments and Electrochemical Experiments

The surface morphology and composition of the prepared catalysts were characterized using scanning electron microscope (JEOL 5900LV) and transmission electron microscope (JEOL 2010). The EDX pattern and elemental mapping of the samples was recorded via the EDX technique using a Hitachi Su-70 Schotty. The crystalline phase of the synthesised samples were obtained using X-ray diffraction (PW1050-3710 diffractometer with a Cu K_α (λ = 1.5405 Å) radiation source). X-ray photoelectron spectroscopy studies were done using a Thermo Scientific K-α XPS spectrometer. All samples were run at a takeoff angle (relative to the surface) of 90°. A monochromatic Al K_α X-ray source was utilized, with a spot area of 400 μm. Charge compensation was provided, and the position of the energy scale was adjusted to place the main C 1s feature (C−C) at 284.6 eV. All data analysis was performed using XPSPEAK 4.1 software. Thermogravimetric analysis was performed (SDTQ600) in a dried air atmosphere with a heating rate of 10 °C per minute. Fourier transformer infrared spectroscopy measurements were performed using a Bruker TENSOR27 FTIR spectrometer (Bruker Optics, Germany) with a DTGS detector and a KBr beam splitter in the range from 400 to 4000 cm^{-1} at a resolution of 4 cm^{-1}. The N_2 gas adsorption and desorption studies were conducted using a Quantachrome Nova 2200 surface area and pore size analyzer. All of the samples were initially degassed at 250°C for 3 h under vacuum. Inductively coupled plasma atomic emission spectroscopy was employed to determine the concentrations of metal ions in the solutions prior to and following the photochemical reduction experiment.

The catalytic activity and electrochemical performance of all catalysts were investigated using a VoltaLab Potentiostat PGZ301. A three-electrode cell system was employed in all the electrochemical studies. The counter electrode was a polycrystalline Pt coil, which was flame

annealed prior to the experiments. The reference electrode utilized was a silver/silver chloride (Ag/AgCl). All measurements were conducted at room temperature (22 ± 2°C).

3.2.3 Fabrication of Electrodes

3.2.3.1 Fabrication of Nanomaterials

The synthesis of the Cd:Pd and Cd@Pd nanostructure can be divided into two steps: (i) formation of the Cd core nanoparticles; (ii) development of the shell by subsequent reduction of the Pd precursors, where the Cd nanoparticles act as "seeds". Initially Cd cores were prepared by adding 5.0 mL of 0.02 M $Cd(NO_3)_2$ solution into 25.0 mL of 0.5 M sodium acetate solution and being stirred for 90 min. Then the mixed solution was added dropwise into 50.0 mL of a 0.4 M sodium borohydride solution at room temperature, and stirred for 3 h. To synthesize the Cd:Pd and Cd@Pd nanoparticles, stoichiometric volumes of a 0.02 M $Pd(NO_3)_2$ precursor were added dropwise into the Cd core solution to obtain the desired ratios of Cd:Pd and Cd@Pd nanoparticles. After three hours of stirring, the obtained colloidal solution was centrifuged at 12,000 rpm for 15 min and rinsed several times with water. The final product was dried in a vacuum oven overnight at 45^{o}C. Pd@Cd(1:2) core/shell nanostructures were synthesised using same approach as Cd@Pd core/shell nanoparticles, where Pd acted as core and Cd as the shell. For comparison purposes Pd nanoparticles were prepared by adding 5.0 mL of 0.02 M $Pd(NO_3)_2$ solution into 25.0 mL of 0.5 M sodium acetate solution and being stirred for 90 min. Then the mixed solution was added dropwise into 50.0 mL of a 0.4 M sodium borohydride solution at room temperature, and stirred for 3 h. The solution was centrifuged at 12,000 rpm for 15 min and rinsed several times with water. The final product was dried in a vacuum oven overnight at 45^{o}C.

3.2.3.2 In-situ Heat Treatment of Pd Thin Foil

The heating of Pd thin foil was carried out in an Anton-Paar HTK-1200 high temperature oven chamber. The sample holder made of aluminium oxide (corundum) which contribute to extra peaks in the XRD pattern. The sample holder is motor-powered in order to adjust the height and the incidence of the sample comparatively to the incident X-ray beam. Argon gas was passed through out the in-situ XRD temperature experiments to avoid the formation of oxide on the surface of the Pd thin film. The temperature sensor in HTK 1200N is located right beneath the sample in a protective ceramic sample holder. In this experiments the temperatures of the Pd foils were raised at a ramp speed of 10 °C per minute and heated to their respective temperature, once the chamber attains the specific temperature the XRD patterns were recorded. The samples were cooled down at a ramp rate of 5 °C per minute. Once the samples attained room temperature, the samples were taken out of the in-situ chamber and the XRD patterns were recorded using spinning stage XRD to avoid corundum peaks which were present during in-situ treatment. After XRD all samples were stored in argon atmosphere at room temperature for the electrochemical measurements.

3.2.3.3 Synthesis of Pd/rGO Nanocomposite

The fabrication of Pd/rGO nanocomposites was achieved via the in situ electrochemical reduction of the GO and Pd precursors. The GCE surface was polished with alumina powder (0.5 μm) followed by sonication in pure water for 1 min. A 20 μL mixture of GO (0.5 mg/mL), $Pd(NO_3)_2$ (10mM) and Nafion (0.5%) was cast on the GCE and then allowed to air dry. The in situ formation of Pd NPs and rGO nanocomposites on the GCE was achieved using cyclic voltammetry (CV) in 0.1 M Na_2SO_4 (pH 7) by cycling the electrode potential between +0.5V and -1.2V (vs Ag/AgCl) at 10mVs for ten cycles. For comparison, Pd NPs and rGO were prepared individually using the identical electrochemical approach under similar conditions.

3.2.3.4 Synthesis of g-C_3N_4 and Pd-g-C_3N_4

Urea (99.99%) was employed in this work to synthesize the g-C_3N_4 nanomaterials. In a typical reaction, 15.0 g urea was added to 20.0 ml of distilled water. The solution was stirred for 30 min until all of the urea was dissolved, and then heated to 400 °C. The solid products obtained were heated further at 450 °C in a closed chamber oven for 3 h.[22] The Pd NPs were directly deposited onto g-C_3N_4 using a facile photo-assisted reduction process. To deposit Pd NPs onto the g-C_3N_4, 10.0 mM $Pd(NO_3)_2$ and 1.0 mg of synthesized g-C_3N_4 were added in 5 mL of ultrapure water and sonicated for 15 min. Subsequently, 5 mL of 50% (v/v) methanol was added to the above solution, thereafter it was deaerated for 20 min with ultrapure argon gas. The solution was then irradiated by UV-Visible light for 60 min and finally rinsed with ultrapure water several times and centrifuged and dried in a vacuum oven at 40 °C overnight. The mass of the Pd NPs (10%) loaded onto the carbon nitride was indirectly measured using inductively coupled plasma atomic emission spectroscopy (ICP-AES) and further confirmed by TGA.

3.3 Summary

This chapter has presented the materials used in this Ph.D. thesis. The experimental procedures and techniques used for fabrication and characterization of Pd thin foil and Pd-based nanomaterials were discussed in detail. The following chapter will present a synthesis and electrochemical study of Cd@Pd core/shell nanomaterials for hydrogen sorption and storage.

References

1. S. K. Konda, A. Chen. One step synthesis of Pd and reduced graphene oxide nanocomposite for enhanced hydrogen sorption and storage. *Electochem. Commun.* **2015,** 60, 148–152.

2. S. K. Konda, C. K. Ostrom, A. Chen. Synthesis and electrochemical study of Cd@Pd core/shell nanomaterials for hydrogen sorption and storage. *Int. J. Hydrogen. Energ*. **2015**, 40, 16365-16374.

3. S. K. Konda, M. Amiri, A. Chen, Photo-assisted deposition of palladium nanoparticles onto carbon nitride for efficient oxygen reduction. *J. Phys. Chem. C.* **2016**, 120, 14467−14473.

Chapter 4: Synthesis and Electrochemical Study of Cd@Pd Core/Shell Nanomaterials for Hydrogen Sorption and Storage

4.1 Introduction

One proposed solution toward the amelioration of the global energy crisis is thought to be the establishment of a hydrogen economy; however, its realization is still quite distant. Hydrogen is not naturally occurring on earth, but it is a fundamental component of the universe. The hydrogen must be artificially produced and the storage of hydrogen is challenging, as under atmospheric conditions its energy density is 1/3000 less than that of gasoline.[1,2] The discovery of hydrogen storage materials with long term sustainability toward enabling our energy future is one of the most challenging problems to be overcome in the establishment of a hydrogen economy.[3,4] Hydrogen is set to be become a key energy in bridging the gap between intermittent renewables and rapidly depleting fossil fuels.[5] Current potential hydrogen storage technologies encompass high pressure gas, cryogenic tanks, metal hydrides, complex hydrides and metal organic frameworks.[6-12] In recent years, significant attention has gravitated to metal hydride materials due to their unique storage attributes, which may readily take up and release large volumes of hydrogen.[13-15]

Recently, it has been demonstrated that bimetallic core/shell nanocatalyst possess superior catalytic properties, which are not attainable via their bimetallic alloy and monometallic counterparts.[16,17] The design and establishment of nanostructured core/shell boundaries have been observed to enable major alterations in physical and chemical

---

*The results presented in this chapter have been published in the *International Journal of Hydrogen Energy* **2015**, 40, 16365-16374.

properties that play critical roles in technological applications.[18-26] The relationship between a core and shell may be regarded as a type of phase separation, which involves a core that is encapsulated by a metallic shell.[27] The enhanced stability and compatibility of core/shell nanostructured materials may be achieved through the kinetic trapping of a core nanoparticle that is surrounded by a metallic shell, which might alter the functionality and properties of the core, as well as the shell, resulting in the provision of a natural vehicle toward obtaining multifunctional materials.[28] The catalytic performance of nanostructured core/shell materials may be effectively tuned by optimizing their size, structure, and composition.[29-31] However, further efforts are still required to fully elucidate the intimate relationship between hybrid material structures and their electrocatalytic properties.[32] The electronic surface properties of the core/shell nanoparticles may be modified by the lattice strain that is established within these core/shell nanostructures, as well as the heterometallic bonding interactions between the core/shell nanoparticles.[33] The size and structure of palladium plays an important role in its uptake of hydrogen during electrochemical sorption.[34] Pd has the capacity to reversibly store a very large volumetric amount of hydrogen at room temperature and is proven to be extremely stable;[35] however, the poor gravimetric capacity and exorbitant cost of Pd make it unsuitable for use as the sole metal for hydrogen storage.[36,37] Our recent studies have shown that Cd and Pd have robust electronic interactions, which significantly boost the hydrogen electrosorption properties of Pd.[38,39] The enhanced hydrogen spillover effect was achieved through the modification of the electronic structure of Pd via the presence of Cd, as the interaction between Cd-H is much lower than that of Pd-H.[40] The low cost and abundance of Cd make it an attractive candidate material for combining with Pd. The coating of a cost effective core material with

a more expensive Pd shell material is thus economically favourable. Although Cd is used in many applications, such as coatings, pigments, batteries, plating alloys, and as a stabilizer for plastics, it is considered to be a potential environmental hazard. It is anticipated that the hazardous nature of Cd might be suppressed via its incorporation as a core material.

In the present study, Pd and CdPd nanoparticles as well as Cd@Pd and Pd@Cd core/shell nanomaterials having various compositions were synthesized and studied for hydrogen sorption. To the best our knowledge, this is the first report on a core/shell nanostructure with Cd as the core and Pd as the shell. The effects of a capping agent on the formation of the core/shell, as well as on hydrogen sorption and storage were studied. Five different catalyst compositions (Pd, CdPd(1:1), Cd@Pd(1:2), Pd@Cd(1:2) and Cd@Pd(1:3)) were selected and prepared for systematic investigation. The objective of this study was to determine the ideal catalyst composition of a nanometric core/shell entity for improved hydrogen sorption and storage. Our studies have shown that a Cd@Pd core/shell nanomaterial with an optimized composition of 1:2 significantly enhances hydrogen sorption and storage capacity, in comparison to pure Pd and CdPd nanoparticles. Palladium serves not only as a catalyst for hydrogen sorption, but also protects the Cd core from corrosion due to the formation of the Cd@Pd core/shell nanostructure.

In this chapter, when I started my PhD, Cassandra K. Ostrom assisted with the initial electrochemical experiments like CV (Fig. 4.5) and CA (Fig. 4.8). All the material characterisation, analysis and rest of the electrochemical studies were performed by me.

4.2 Experimental

4.2.1 Materials

Sodium acetate was employed as a capping agent and sodium borohydride was used as a reducing agent. $Cd(NO_3)_2.4H_2O$ and $Pd(NO_3)_2.xH_2O$ were used as metallic precursors for the synthesis of the Pd, CdPd, Cd@Pd and Pd@Cd nanoparticles. All chemicals were purchased from Aldrich. Pure water (18.2 MΩ cm) was obtained from a NANOpure Diamond UV ultrapure water purification system and was used in the preparation of all samples and solutions.

4.2.2 Fabrication of Nanomaterials

The synthesis of the Cd:Pd and Cd@Pd nanostructure can be divided into two steps: (i) formation of the Cd core nanoparticles; (ii) development of the shell by subsequent reduction of the Pd precursors, where the Cd nanoparticles act as "seeds". Initially Cd cores were prepared by adding 5.0 mL of 0.02 M $Cd(NO_3)_2$ solution into 25.0 mL of 0.5 M sodium acetate solution and being stirred for 90 min. Then the mixed solution was added dropwise into 50.0 mL of a 0.4 M sodium borohydride solution at room temperature, and stirred for 3 h. To synthesize the Cd:Pd and Cd@Pd nanoparticles, stoichiometric volumes of a 0.02 M $Pd(NO_3)_2$ precursor were added dropwise into the Cd core solution to obtain the desired ratios of Cd:Pd and Cd@Pd nanoparticles. After three hours of stirring, the obtained colloidal solution was centrifuged at 12,000 rpm for 15 min and rinsed several times with water. The final product was dried in a vacuum oven overnight at 45^{o}C. Pd@Cd(1:2) core/shell nanostructures were synthesised using same approach as Cd@Pd core/shell nanoparticles, where Pd acted as core and Cd as the shell. For comparison purposes Pd nanoparticles were prepared by adding 5.0 mL of 0.02 M $Pd(NO_3)_2$ solution into 25.0 mL of 0.5 M sodium acetate solution and being stirred for 90 min. Then the mixed solution was added

dropwise into 50.0 mL of a 0.4 M sodium borohydride solution at room temperature, and stirred for 3 h. The solution was centrifuged at 12,000 rpm for 15 min and rinsed several times with water. The final product was dried in a vacuum oven overnight at 45°C.

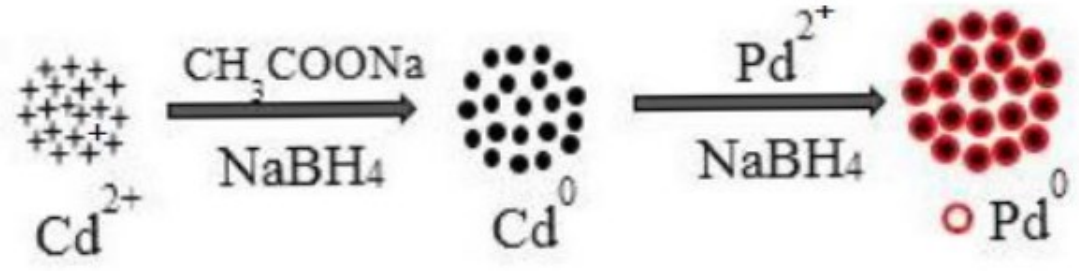

Scheme 1. Schematic Illustration of the Fabrication of the Cd@Pd Core/Shell Nanostructures.

4.2.3 Preparation of Electrodes

The working electrodes used in this study were glassy carbon electrodes (GCEs) (0.1964 cm^2 surface area), which were coated with the synthesized nanoparticles. Prior to coating, the GCE surface was polished to a high sheen. The coating solution was prepared by dispersing 1.0 mg of the fabricated nanoparticles in 1.0 mL of 40% isopropanol, which was then sonicated for 20 min to obtain uniform nanoparticle dispersion. This was followed by the addition of 10 µL Nafion with further sonication for an additional 20 min. A total of eight coats of 10 µL aliquot solutions were applied to the GCE surface and allowed to dry overnight.

4.2.4 Instruments

The surface morphologies of the synthesized samples were characterized using JEOL 2010 transmission electron microscopy (TEM). X-ray diffraction patterns were recorded using a Pananalytical Xpert Pro Diffractometer with a Ni filtered monochromatic Cu K_α (1.5406 Å, 2.2 KW Max). X-ray photoelectron spectrophotometry (XPS) was performed using a Thermo

Scientific K-Alpha XPS spectrometer. The samples were run at a takeoff angle (relative to the surface) of 90°. A monochromatic Al Kα X-ray source was employed with a spot size of 400 μm. The position of the energy scale was adjusted to position the main C1s feature (C-C) at 284.6eV. All data acquisition was enabled by XPSPEAK 4.1 software. The nanomaterial's composition was examined by energy dispersive X-ray spectrometry (EDX). Inductively coupled plasma atomic emission spectroscopy (ICP-AES) was employed to determine the concentrations of the precursors in solution, prior to, and following the reduction of $NaBH_4$.

4.2.5 Electrochemical Studies

An assessment of the electrochemical performance of the electrodes for hydrogen adsorption/absorption was carried out using cyclic voltammetry (CV) and chronoamperometry (CA), which involved a three-electrode cell system and a Volta Lab PGZ402 potentiostat. The counter electrode used was a Pt wire coil (10 cm^2), which was cleaned prior to each experiment via flame annealing and quenching with NANOpure water. The reference electrode was comprised of silver-silver chloride (Ag/AgCl) in 1 M KCl. All electrode potentials mentioned from this point forward are with respect to the Ag/AgCl electrode. The working electrodes were prepared by coating a GCE with the synthesized nanoparticles. Prior to the electrochemical experiments, ultrapure argon gas (99.999%) was bubbled through a 0.5 M H_2SO_4 electrolyte solution for approximately 15 min, and the argon was continuously passed over the solution during the electrochemical measurements. CA was performed to completely saturate the films with hydrogen, where the electrode potential was held at a range of -50 to -230 mV for 3 min. Linear Voltammetry (LV) was carried out immediately after CA at a scan rate of 10 mV/s for the desorption of

hydrogen. Data acquisition and analysis were performed using VoltMaster 4 software; and all experiments were carried out at room temperature.

4.3 Results and Discussion

4.3.1 Surface Analysis

The surface morphologies of the Pd, CdPd(1:1), Cd@Pd(1:2), Cd@Pd(1:3) nanoparticles prepared in the presence of the capping agent and the Cd@Pd(1:2) sample fabricated in the absence of the capping agent were characterized using a TEM. Fig. 4.1 presents the typical TEM and high-resolution TEM (HRTEM) images of the Pd nanoparticles and the Cd@Pd(1:2) nanoparticles. As seen in Fig. 4.1b, the average particle size of the formed Cd@Pd(1:2) core/shell nanomaterials was ~6.0 nm, which is slightly smaller than that of the Pd nanoparticle (Fig. 4.1a). For comparison, the TEM images of the CdPd(1:1) and Cd@Pd(1:3) nanoparticles prepared in the presence of the capping agent and the Cd@Pd(1:2) sample fabricated in the absence of the capping agent are displayed in Fig. 4.2. The particles formed in the absence of the capping agent were significantly larger, demonstrating the effective usage of the capping agent in the present study. The lattice spacing distance d between the adjacent planes was calculated using the HRTEM images where the lattice fringes were clearly observed. In the case of the Pd nanoparticles (Fig. 4.1c), the value of d = 0.229 nm may be attributed to the Pd{111} plane. The Cd@Pd(1:2) core/shell structure (Fig. 4.1d) exhibits two distinctive d values: 0.256 nm of the Cd{100} plane and 0.233 nm which may be ascribed to the Pd{111} plane.[41]

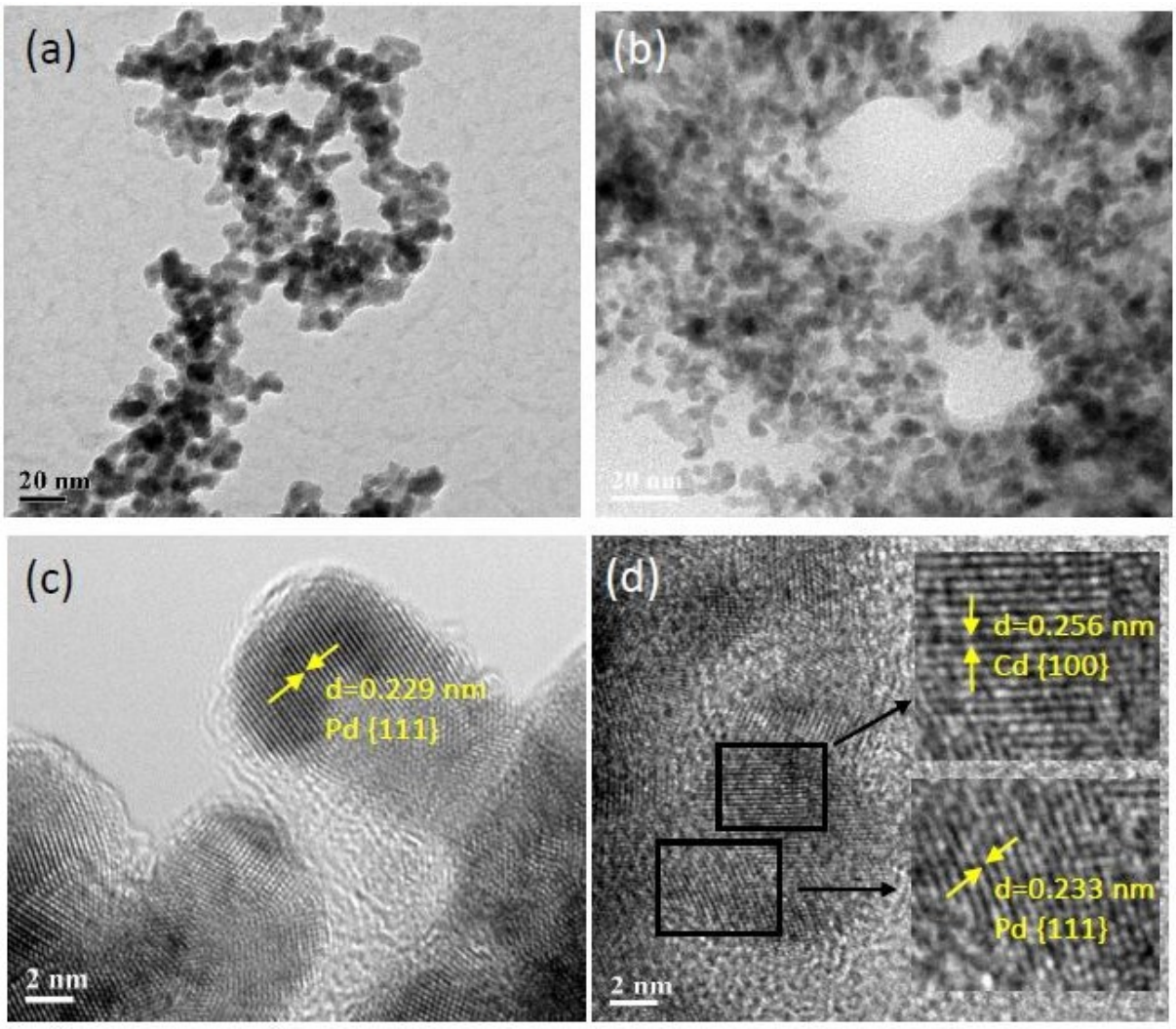

Figure. 4.1 TEM and HRTEM images of the Pd nanoparticles (a and c) and the Cd@Pd(1:2) core/shell nanoparticles (b and d).

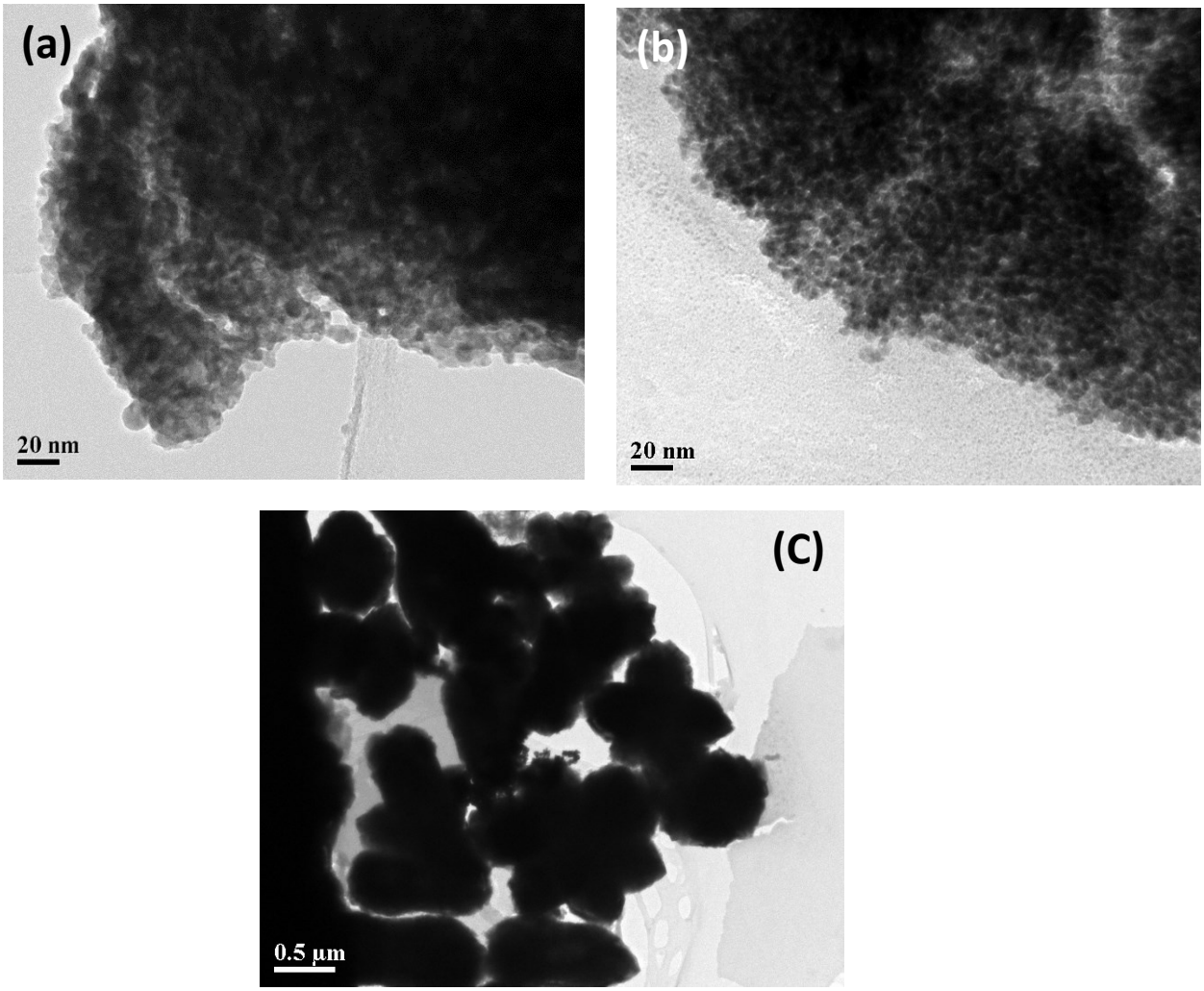

Figure. 4.2 TEM image of (a) CdPd(1:1), (b) Cd@Pd (1:3) nanoparticles synthesised with capping agent and (c) Cd@Pd (1:2) particles synthesised without capping agent.

XRD patterns of the Cd nanoparticles and Pd nanoparticles and the Cd@Pd(1:2) core/shell nanomaterial synthesized in the presence of the capping agent are presented in Fig. 4.3a. It is obvious that all the Cd and Pd peaks observed for Cd and Pd nanoparticles appeared in the XRD pattern of the formed Cd@Pd(1:2) core/shell nanostructure and that there was no significant peak shift, indicating the Pd and Cd phase separation as well as the non-existence of a PdCd alloy. The lattice constant value for the Pd in the case of the Cd@Pd(1:2) nanoparticles was calculated to be 3.90 Å, which is slightly larger than that of the pure Pd nanoparticles (3.89 Å).[42] The small increase in the lattice constant may be attributed to the weak interaction between the Cd core and the Pd shell.

The compositions of the synthesized nanoparticles were examined using both EDX directly and ICP-AES analysis indirectly. The EDX spectra of Pd, Cd and Cd@Pd(1:2) nanoparticles are shown in Fig. 4.3(b), confirming the presence of both Cd and Pd in the Cd@Pd(1:2) nanostructures. A quantitative analysis of these EDX spectra showed that the composition of the prepared catalysts was consistent with the initially added metallic precursors. This was further confirmed by ICP-AES analysis. The solutions containing the metal precursors, prior to and following the preparation of the core/shell nanoparticles, were analysed by ICP-AES for the metal contents of Pd and Cd listed in Table 4.1. In the case of Cd, almost 100% of Cd^{2+} ions were completely reduced; whereas over 99.5% of Pd^{2+} ions were reduced in solution in most cases. Through the subtraction of the final metal concentrations from the initial metal content, it was found that the bulk composition of the formed core/shell nanoparticles was equivalent to the input compositions, showing that the chemical reduction method utilized in this study was efficacious in controlling the compositions of the final products. This is consistent with the EDX analysis.

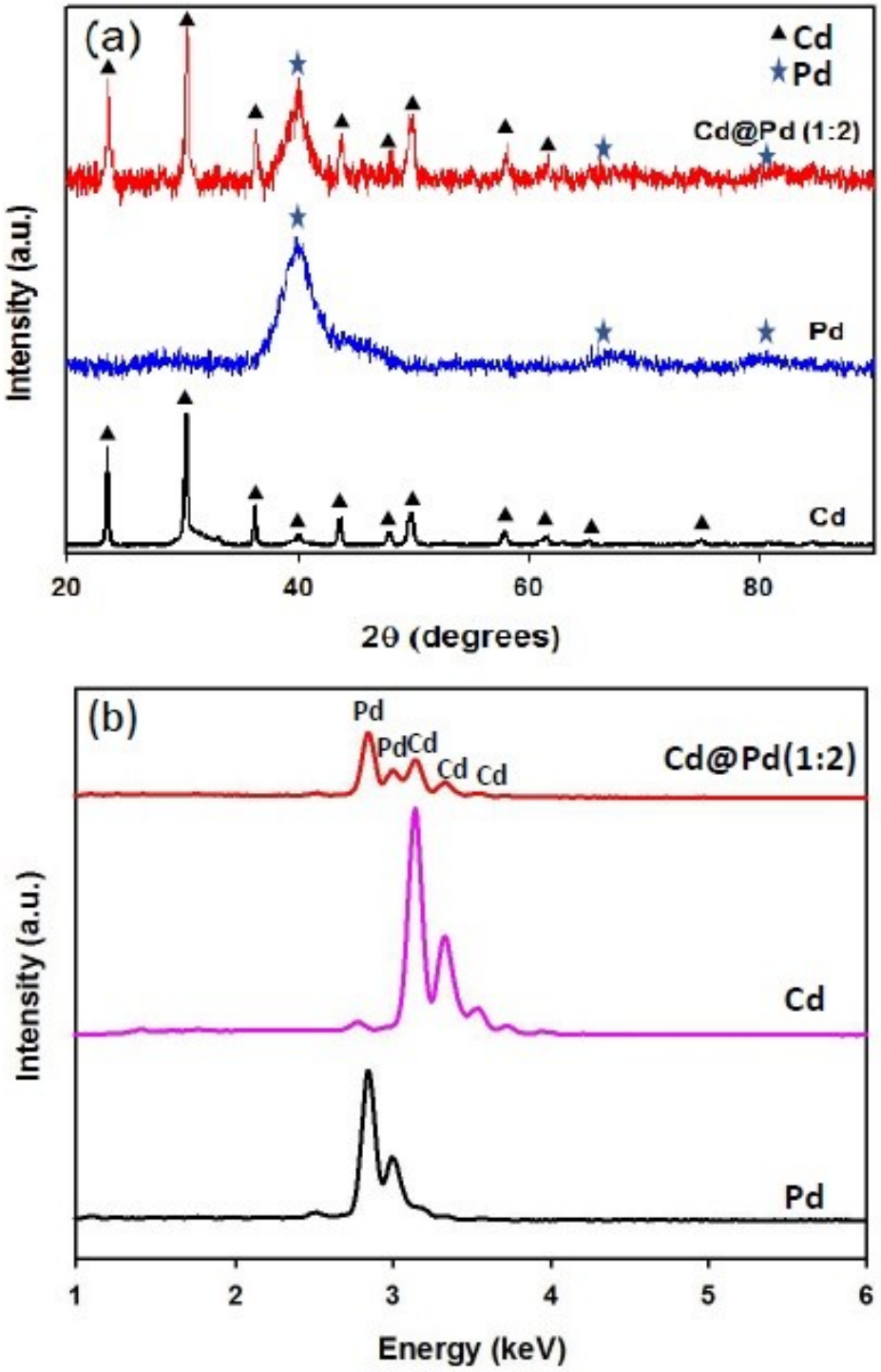

Figure. 4.3 (a) XRD patterns and (b) EDX spectra of the Pd, Cd and Cd@Pd(1:2) nanoparticles.

Table 4.1. ICP-AES results of the concentration of Pd^{2+} and Cd^{2+} remaining in solution prior to and following chemical reduction with sodium borohydride.

Sample	Initial [Pd] (ppm)	Initial [Cd] (ppm)	Final [Pd] (ppm)	Final [Cd] (ppm)	Molar Ratio Cd:Pd
Pd	68.65	0.00	0.0417	0.000	0:100
CdPd (1:1)	66.51	70.25	1.498	0.002	50:50
Cd@Pd (1:2)	129.00	68.12	0.576	0.001	33:67
Cd@Pd (1:3)	187.80	66.12	0.226	0.003	25:75

To investigate the chemical nature of the formed core/shell metallic nanoparticles, an XPS technique was employed, with the results shown in Fig. 4.4. Fig. 4.4a presents the elemental survey scans of the five different samples, revealing the strong Cd and Pd peaks for the CdPd and Cd@Pd nanoparticles, as well as the presence of trace amounts of a Carbon 1s peak at approximately 284 eV, an oxygen 1s peak at approximately 531 eV, which could be due to atmospheric O_2, CO_2, and H_2O absorption during the sample preparation and storage. For all of the samples, Pd 3d doublets and Pd 3p peaks were observed at ~335.4 and 560.0 eV, respectively. The Cd 3d doublet peaks appeared at 406 eV for the core/shell nanoparticles. The high resolution spectra of Pd 3d in the case of pure Pd nanoparticles and the Cd 3d and Pd 3d regions of the Cd@Pd(1:2) sample are displayed in Figs. 4.3b – 4.3d. The binding energies of the Pd $3d_{3/2}$ and Pd $3d_{5/2}$ peaks for the Pd nanoparticles (Fig. 4.4b) were measured at 340.5 and 335.5 eV, respectively. In the case of Cd@Pd core/shell nanoparticles, the Cd 3d doublet peaks (Fig. 4.4c) were measured at 412.2 and 405.5 eV, while the Pd 3d doublet peaks (Fig. 4.4d) appeared at 341.0 and 335.6 eV.

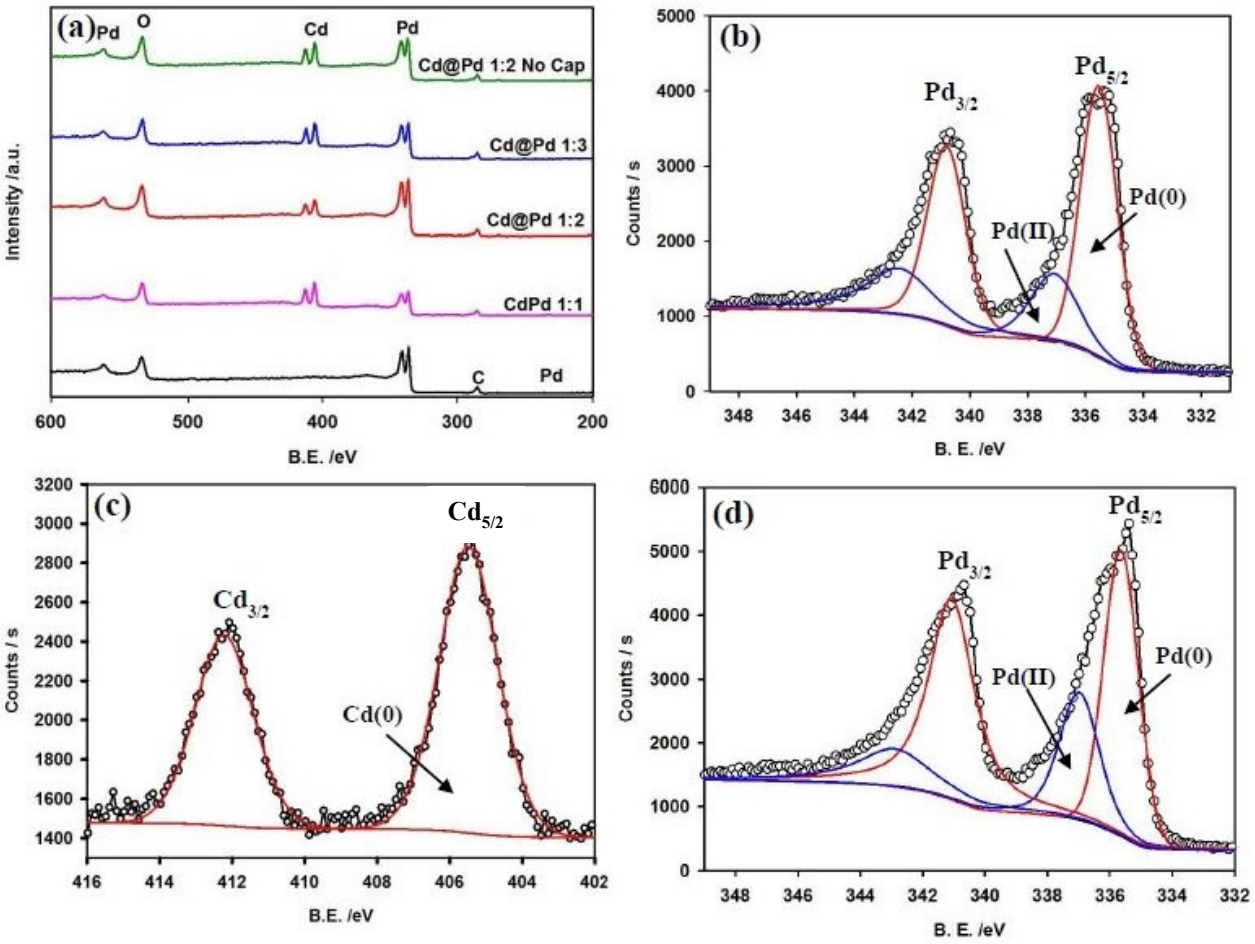

Figure. 4.4 (a) XPS survey scans of the five samples; (b) high resolution spectrum of Pd 3d region of the pure Pd nanoparticles; (c) high resolution spectrum of Cd 3d region; and (d) high resolution spectrum of Pd 3d region of the Cd@Pd(1:2) nanoparticles.

By fitting the high resolution XPS spectra, the oxidation states of the formed Pd and Cd@Pd nanoparticles were determined, revealing that Cd was mainly in its metallic state. For comparison, Table 4.2 presents the binding energy and the Pd oxidations states of Pd, CdPd(1:1), Cd@Pd(1:2) and Cd@Pd(1:3) nanoparticles synthesized in the presence of the capping agent and the Cd@Pd(1:2) particles prepared in the absence of capping agent.

Table 4.2. Binding energy and the Pd oxidations states of all the five samples.

Catalyst	**Species**	**Binding Energy (eV)**		**Relative area peak (%)**
		$Pd_{3/2}$	**$Pd_{5/2}$**	
Pd	Pd(0)	340.5	335.5	65.1
	Pd(II)	342.5	337.1	34.9
Cd:Pd(1:1)	Pd(0)	340.7	335.3	72.9
	Pd(II)	342.9	337.2	27.1
Cd@Pd(1:2)	Pd(0)	341.0	335.6	62.5
	Pd(II)	342.8	336.9	37.5
Cd@Pd(1:3)	Pd(0)	340.8	335.4	70.8
	Pd(II)	342.4	336.8	29.2
Cd@Pd(1:2) No Capping agent	Pd(0)	340.8	335.5	61.3
	Pd(II)	342.6	337.3	38.7

4.3.2 Electrochemical Activity of the Synthesized Pd-based Nanostructures

Fig. 4.5a presents typical CVs of the Cd@Pd(1:2) nanoparticles prepared in the presence (red curve) and absence (green curve) of the capping agent, which were recorded in 0.5 M H_2SO_4, in the electrode potential range of between -225 and 400 mV, at a scan rate of 10 mV/s. Significant differences in hydrogen sorption and desorption were observed from the two CVs when the potentials were scanned from 100 mV to -225 mV. For the Cd@Pd nanoparticles synthesized in the presence of the capping agent, when scanning the electrode potential was from 400 to -225 mV, hydrogen adsorption began at 100 mV. The cathodic current slowly increased when the potential was altered from 100 to -180 mV, and rapidly increased with further negative potential scanning. It is difficult to decouple the absorption process from the adsorption process in the hydrogen region due to the high current that is caused by hydrogen absorption, which dominates and covers the adsorption processes.[43] A large peak centred at -130 mV, followed by a broad shoulder in the range from -100 to 0 mV, appeared due to hydrogen desorption when the electrode potential was scanned from -225 to 400 mV. In contrast, for the Cd@Pd nanoparticles prepared in the absence of the capping agent, the currents for both hydrogen sorption and desorption were much smaller, with a notable hydrogen sorption peak at -200 mV and a broad hydrogen desorption peak at -100 mV. The integrated charges from the CVs for hydrogen desorption were 458 mC and 75 mC for the Cd@Pd nanoparticles, synthesized with and without capping agents, respectively, revealing that the capping agent played an important role in increasing the hydrogen electrosorption capacity. The significant improvement may be attributed to the formation of the uniform and small size of the Cd@Pd nanoparticles with the help of the capping agent, which is consistent with the TEM image shown in Fig. 4.1b.

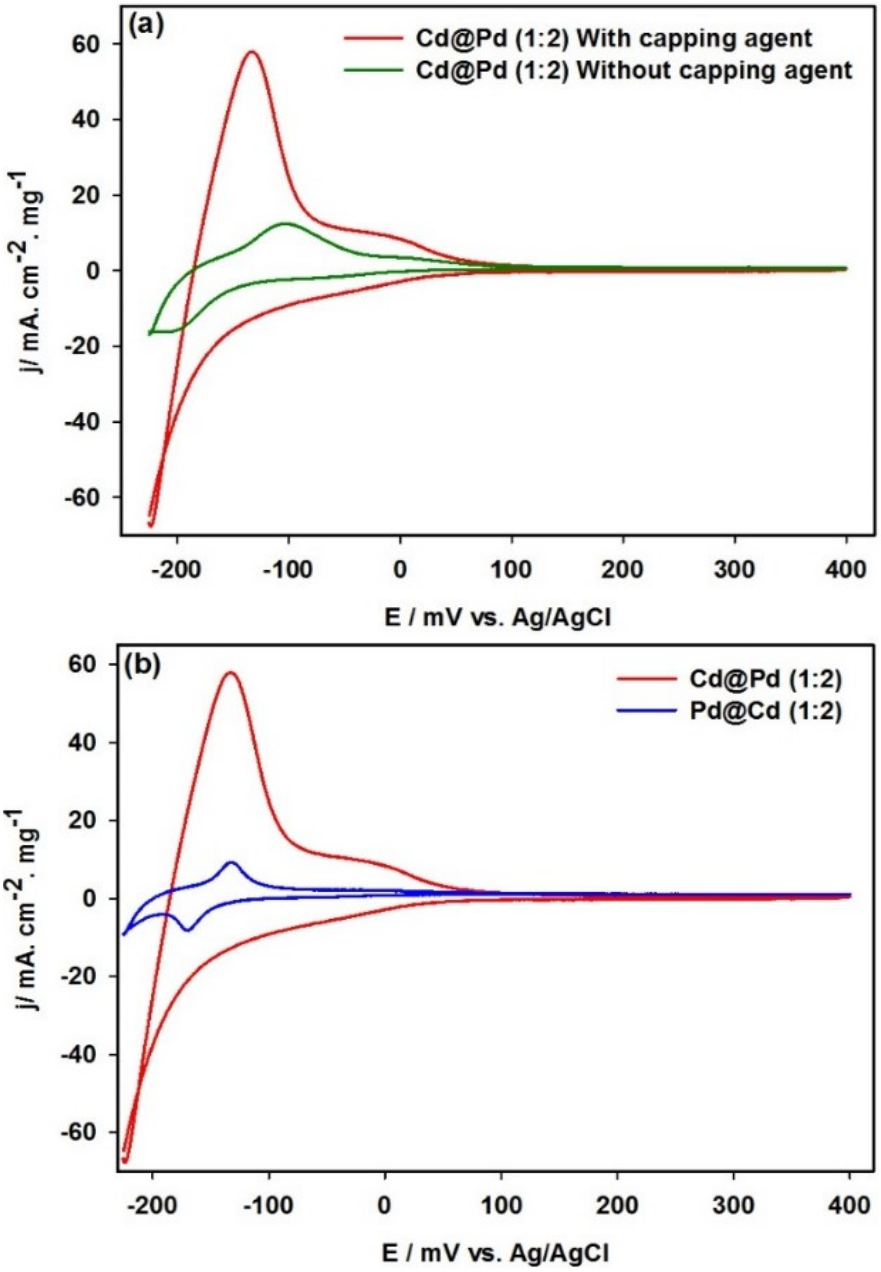

Figure. 4.5 (a) CVs of the Cd@Pd(1:2) core/shell nanomaterials prepared in the presence and absence of the capping agent. (b) CVs of the Pd@Cd(1:2) and Cd@Pd(1:2) core/shell nanostructures synthesized in the presence of the capping agent. Solution: 0.5 M H_2SO_4; Scan rate: 10 mV/s.

To further confirm whether the Cd@Pd(1:2) core/shell structure was formed, we prepared Pd@Cd(1:2) nanoparticles using the identical approach in the presence of the capping agent. It was expected that the hydrogen sorption and desorption charge should be significantly decreased if the Pd@Cd core/shell structure is formed, as Cd would serve as an inactive layer to suppress the hydrogen sorption at the Pd surface. Fig. 4.5b compares the CVs of the Cd@Pd(1:2) and Pd@Cd(1:2) nanoparticles recorded in 0.5 M H_2SO_4 at a scan rate of 10 mV/s. A diminutive but well-defined pair of hydrogen sorption and desorption peaks were observed for the Pd@Cd (1:2) nanoparticles. The charge for hydrogen desorption at the Pd@Cd(1:2) nanoparticles was integrated from the CV to be 5.20 mC, which is only 1.2% of the hydrogen desorption charge of the Cd@Pd(1:2) nanoparticles. These results demonstrate that the Cd@Pd(1:2) and Pd@Cd(1:2) core/shell structures were successfully formed under experimental conditions employed in this study. As the Pd@Cd(1:2) core/shell nanostructures shows negligible amounts of hydrogen desorption charge in comparison to Cd@Pd(1:2) core/shell nanostructures, as well as Cd is exposed on the surface, no further electrochemical experiments and characterisation methods were performed with regard to Pd@Cd(1:2) core/shell nanostructure.

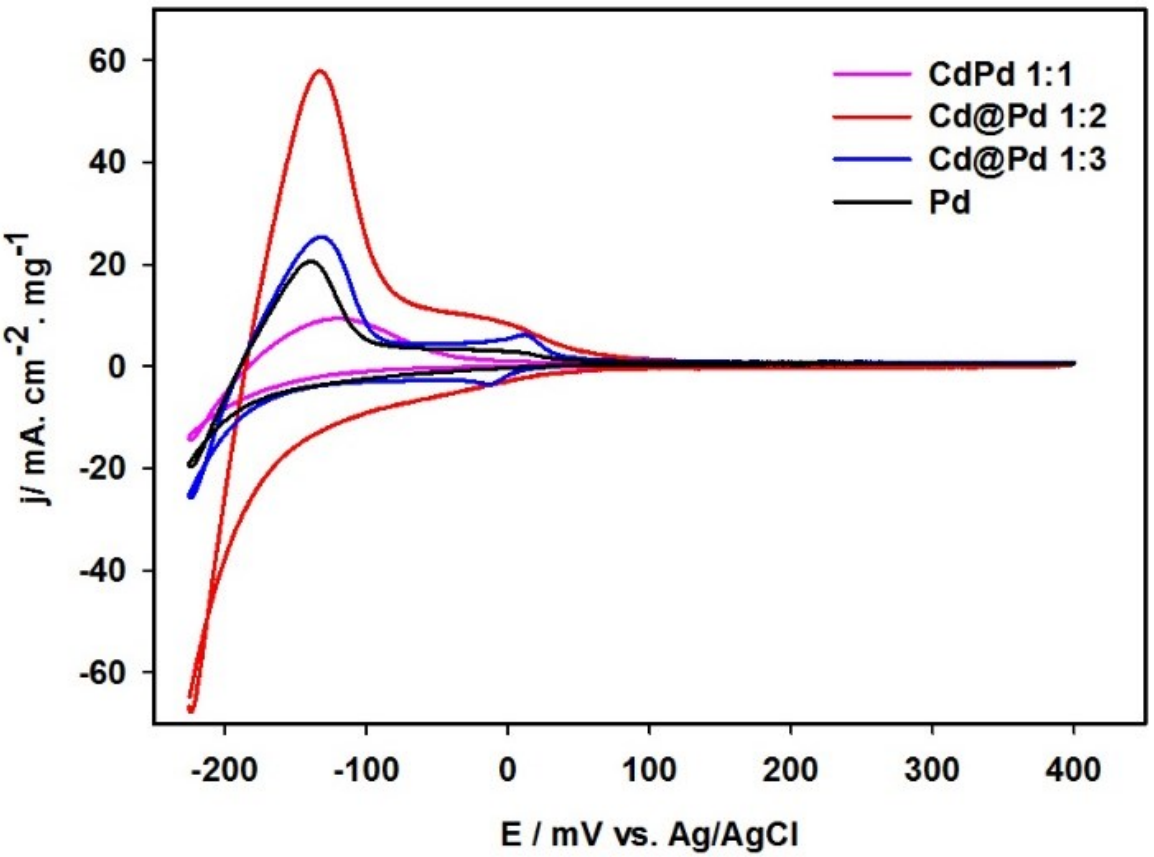

Figure. 4.6 CVs of the synthesized Pd, CdPd(1:1), Cd@Pd(1:2) and Cd@Pd(1:3) nanomaterials recorded in 0.5 M H_2SO_4 at a scan rate of 10 mV/s.

To optimize the formed Pd based nanostructures, nanoparticles with different ratios of Cd to Pd were synthesized in the presence of a capping agent. Fig. 4.6 depicts the CVs of the pure Pd, CdPd(1:1) and Cd@Pd(1:2 and 1:3) core/shell nanoparticles recorded in 0.5 M H_2SO_4 at a scan rate of 10 mV/s. The CV of the PdCd(1:1) nanoparticles was different from the other CVs presented in Fig. 4.6; but similar to the CVs of the PdCd alloyed nanodentrites and nanoparticles.[39] A very broad peak located in the electrode potential range from -200 to –50 mV for hydrogen desorption was observed. The peak current was lower than that of the pure Pd nanoparticles (black curve). These results showed that PdCd nanoparticles, rather than core/shell nanostructures, were formed with Cd:Pd ratio of 1:1

using the identical synthesis approach. When the Cd:Pd ratio was increased to 1:2, a Cd@Pd core/shell structure was formed, resulting in a significant increase in hydrogen sorption and desorption. When the ratio was further increased to 1:3, the current density of the large hydrogen desorption peak, centred at around -130 mV, was significantly decreased, and a small pair of hydrogen adsorption and desorption peaks appeared at ~ 0.0 mV. This might be attributed to a decrease in the surface area per unit Pd mass, as well as the decrease of the interaction between the Cd core and the Pd surface, as the addition of Pd might simply increase the thickness of the shell. The integrated charge densities for hydrogen desorption was increased in the following order: PdCd(1:1) [79.8 mC] < Pd [135.0 mC] < Cd@Pd(1:3) [185.0 mC] < Cd@Pd(1:2) [458.0 mC], showing that the 1:2 ratio was the optimized composition of the formation of the Cd@Pd core/shell nanostructure for hydrogen sorption.

4.3.3 Potential and Composition Dependence of Hydrogen Sorption at Pd-based Nanostructures

To investigate the kinetics and the capacity of hydrogen sorption, chronoamperometry was performed at different electrode potentials with varied time periods immediately followed by linear voltammetry, where the electrode potential was scanned from the held potential to 400 mV. It was found that increasing the holding period from 1 to 3 min resulted in an increase of the hydrogen desorption charge measured from the linear voltammogram (LV). However, no further increase of the charge was observed with a further increase of the holding time, revealing that 3 min was sufficient to ensure the complete saturation of hydrogen into the thin film of the nanoparticles and the core/shell nanomaterials, which were coated onto a glassy carbon electrode.

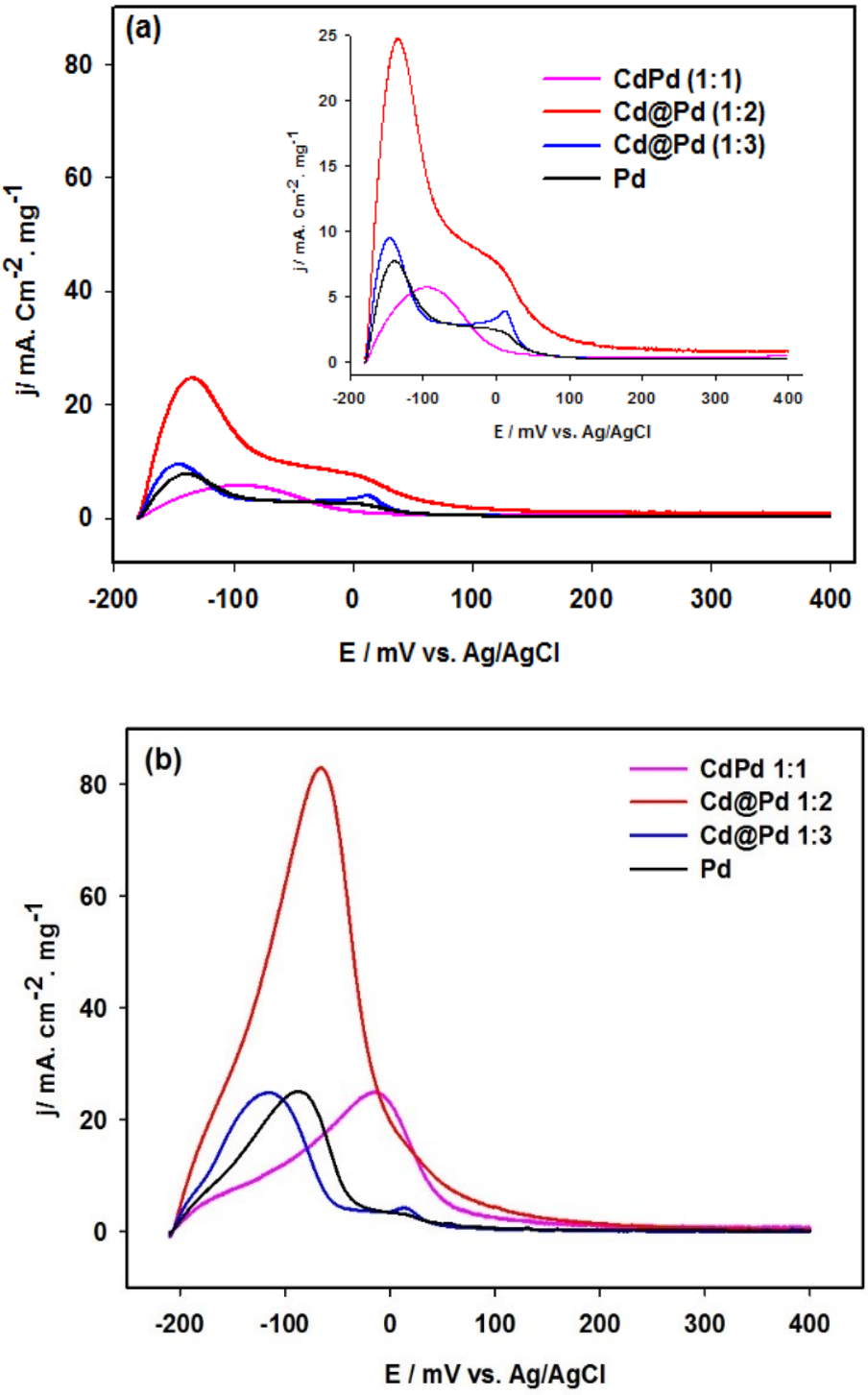

Figure. 4.7 LVs of the synthesized Pd, CdPd(1:1), Cd@Pd(1:2) and Cd@Pd(1:3) nanomaterials after being held at the potential -180 mV (a) and -210 mV (b) for 3 min. Inset shows the expanded version of figure (a). Solution: 0.5 M H_2SO_4; Scan rate: 10 mV/s.

Fig. 4.7a and b present the LVs of the synthesized Pd and CdPd nanoparticles, as well as the Cd@Pd(1:2) and (1:3) core/shell nanostructures, subsequent to being held at -180 and -210 mV for 3 min, respectively. This revealed that the volume of the uploaded hydrogen depended strongly on the composition and structure of the Pd-based nanomaterials and the held electrode potential. The peak potential and peak current density for the hydrogen desorption are listed in Table 4.3. For all four electrodes, a significant increase in the peak current and a dramatic positive shift for the peak potential were observed when the applied electrode potential was decreased from -180 to -210 mV.

Table 4.3. Peak potential and peak current density measured from Fig. 4.6.

Composition	**Held Potential (mV)**	**Peak Potential (mV)**	**Current Density (mA. cm^{-2} mg^{-1})**
Pd	-180	-140	8
	-210	-85	25
CdPd (1:1)	-180	-100	6
	-210	-6	27
Cd@Pd (1:2)	-180	-135	24
	-210	-65	83
Cd@Pd (1:3)	-180	-145	10
	-210	-115	25

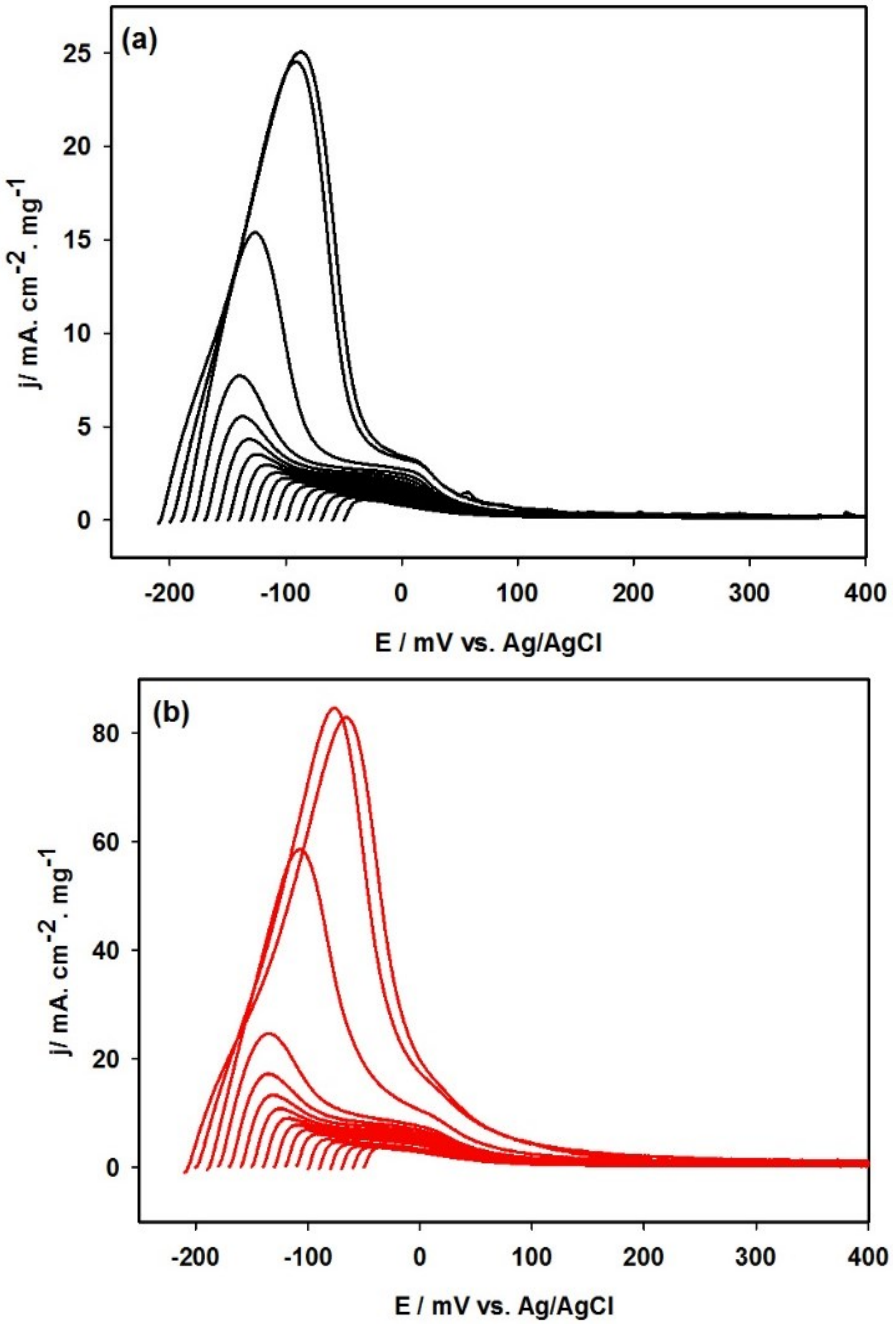

Figure. 4.8 LVs of the pure Pd nanoparticles (a) and the Cd@Pd(1:2) core/shell nanostructures (b) subsequent to holding the different potentials for 3 min. Solution: 0.5 M H_2SO_4; Scan rate: 10 mV/s.

To further investigate the effect of the held electrode potential on hydrogen sorption and storage, Fig. 4.8 presents a series of LVs of the Pd nanoparticles (a) and the Cd@Pd(1:2) nanostructures (b) recorded in 0.5 M H_2SO_4 at a sweep rate of 10 mV/s, following complete saturation with hydrogen for 3 min at potentials that varied from -50 to -210 mV. When the held electrode potential was lowered, from -50 to -180mV, the current for the hydrogen desorption/oxidation peak was slowly increased with a negative shift of the peak potential. Further lowering of the held potential from -180 to -200 mV, the peak current was increased significantly, with a positive shift of the peak potential. While the held potential was lowered, from -200 to -210 mV, the peak current was slightly altered with a small positive shift. Similar behaviours were also observed with the synthesized CdPd(1:1) nanoparticles and the Cd@Pd(1:3) nanomaterials, reflecting the fact that under electrochemical conditions, the volume of hydrogen stored into the Pd-based nanomaterials is potential dependent, where a lower electrode potential corresponds to higher hydrogen pressure in gas phase experiments.[38,44,45]

In order to quantitatively examine the effects of the held potential on the capacity of hydrogen sorption at the Pd, CdPd and Cd@Pd core/shell nanoparticles, the total hydrogen discharge was calculated by integrating the current of the hydrogen desorption/oxidation measured from LV, as displayed in Fig. 4.8. The overall hydrogen oxidation charges (Q_H) for all of the samples at the various held potentials are presented in Fig. 4.9. For all of the samples, Q_H was increased when the held potential was lowered, from -50 to -210 mV. A significant increase in Q_H was observed when the held potential was decreased from -180 to -200 mV, which was due to the phase transition. The adsorption and absorption of hydrogen may result in two different phases (α phase and β phase) in the case of pure Pd.[46]

The α phase appears at low concentrations of hydrogen, where a solid solution is formed. At high concentrations of hydrogen, the β phase appears, where metal hydride is formed, resulting in an increase in the lattice constant. As seen in Fig. 4.8, the electrode potential range of above -180 mV corresponds to the α phase of hydrogen sorption, while the potential range below -200 mV corresponds to the β phase hydrogen sorption. The electrode potentials between -180 and -200 mV represent the α phase and β phase transition region. A comparison of Q_H presented in Fig. 4.9 reveals that the hydrogen sorption of the synthesized Pd based nanomaterials was altered in the following order: CdPd(1:1) < Pd < Cd@Pd(1:3) < Cd@Pd(1:2), showing that the Cd@Pd core/shell nanoparticles with a 1:2 ratio exhibited the highest capacity for hydrogen storage. The Q_H ratios of the Cd@Pd core/shell nanostructures in contrast to the pure Pd nanoparticles at different electrode potentials were calculated and are presented as an inset of Fig. 4.9. The average of the Q_H ratios was further calculated to be 3.40 with a standard deviation of 0.40, showing that by forming the Cd@Pd(1:2) core/shell nanostructures, a 340% increase in the hydrogen storage capacity was achieved in comparison with the pure Pd nanoparticles.

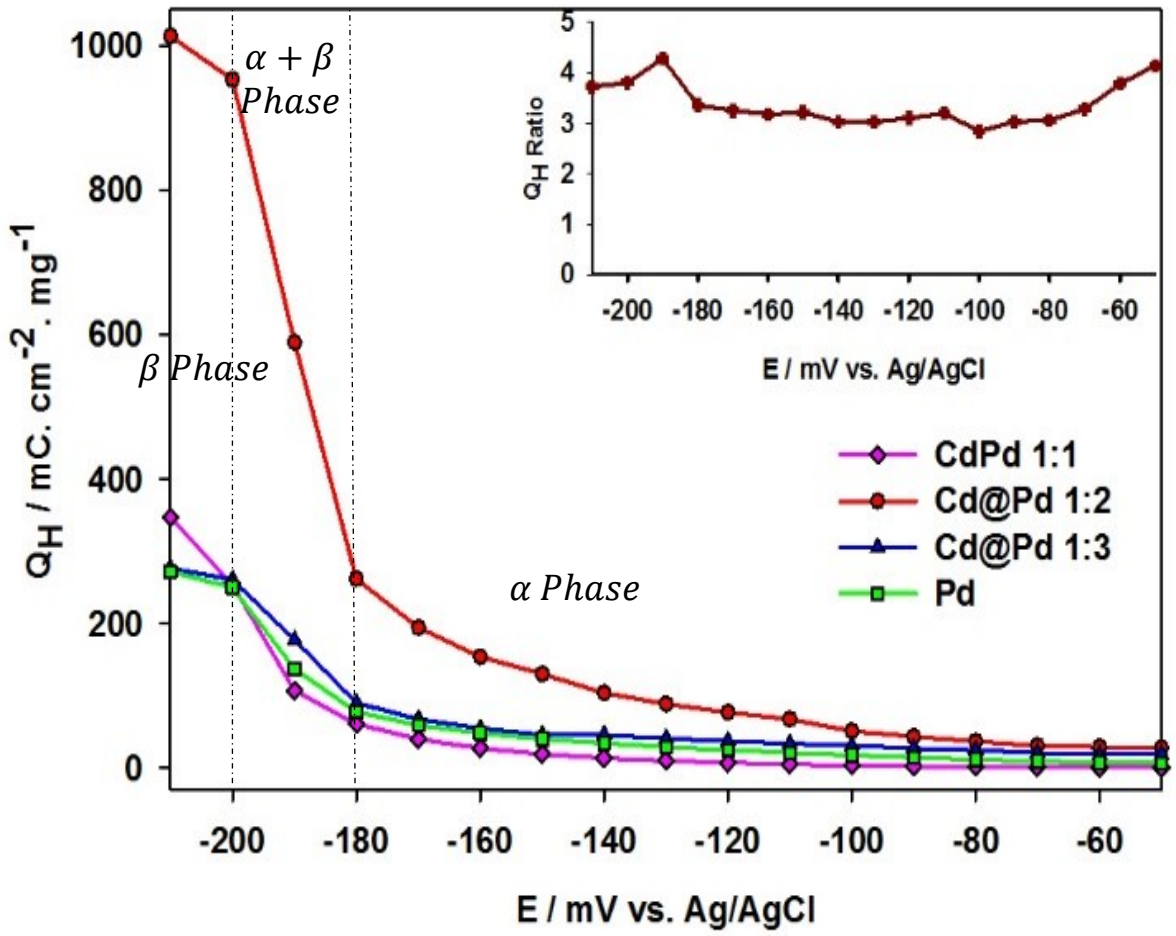

Figure 4.9. The overall hydrogen desorption charge, Q_H, normalized by the mass of Pd versus the held electrode potentials. Inset: Q_H ratio of the Cd@Pd(1:2) core/shell nanostructures to the pure Pd nanoparticles at different electrode potentials.

4.4 Conclusions

In summary, a facile and efficient approach was developed for the synthesis of Cd@Pd core/shell nanostructures. This method is effective for controlling the compositions of the formed core/shell nanoparticles. The effect of a capping agent was investigated, showing that it plays an important role in the formation of the uniform and small size of the Cd@Pd nanoparticles, resulting in a significant improvement in hydrogen sorption and storage. The formation of the Cd@Pd core/shell nanostructure was confirmed by the HRTEM and XRD analysis as well as the cyclic voltammetric studies based upon the electrochemical behaviours of hydrogen sorption and desorption. The capacity for the hydrogen sorption and storage depended strongly on the composition and structure of the formed Pd-based nanomaterials, as well as the applied electrode potential. It was increased in the following order: CdPd(1:1) <Pd <Cd@Pd(1:3) <Cd@Pd(1:2), showing that the Cd@Pd core/shell nanoparticles with a 1:2 ratio exhibited the highest capacity for hydrogen storage. The electrode potential range above -180 mV corresponded to the α phase of hydrogen sorption, while the potential range of below -200 mV corresponded to the β phase hydrogen sorption. A significant increase in the peak current and a dramatic positive shift for the peak potential were due to the α phase and β phase transition when the held electrode potential was lowered, from -180 to -200 mV. Our studies have shown that by forming Cd@Pd core/shell nanostructures with an optimized composition of 1:2, a 340% increase in hydrogen storage was achieved, in comparison with the pure Pd nanoparticles.

References

1. H. Chen, R. T. Yang. Catalytic effects of TiF_3 on hydrogen spillover on Pt/carbon for hydrogen storage. *Langmuir* **2010,** 26, 15394-15398.

2. Y. Xia, Z. Yang, Y. Zhu. Porous carbon-based materials for hydrogen storage: advancement and challenges. *J. Mater. Chem. A*, **2013**, 1, 9365-9381.

3. J.-M. Yan, X.-B. Zhang, T. Akita, M. Haruta, Q. Xu. One-step seeding growth of magnetically recyclable Au@Co core−shell nanoparticles: highly efficient catalyst for hydrolytic dehydrogenation of ammonia borane. *J. Am. Chem. Soc.* **2010**, 132*,* 5326-5327.

4. E. L. González, F. I. Llerena, M. S. Perez, F. R. Iglesias, J.G. Macho. Energy evaluation of a solar hydrogen storage facility: comparison with other electrical energy storage technologies. *Int. J. Hydrogen Energy* **2015**, 40, 5518-5525.

5. M. L. Christian, K.-F. Aguey-Zinsou. Core–shell strategy leading to high reversible hydrogen storage capacity for $NaBH_4$. *ACS Nano* **2012**, 6, 7739-7751.

6. Y. H. Hu, E. Ruckenstein. Hydrogen storage in $LiNH_2/Li_3N$ material for H_2/CO_2 mixture gas as hydrogen source. *Ind. Eng. Chem. Res.* **2007**, 47, 48-55.

7. S. K. Konda, A. Chen. One-step synthesis of Pd and reduced graphene oxide nanocomposites for enhanced hydrogen sorption and storage, *Electrochem. Commun*. **2015**, 60,148-152.

8. J. L. C. Rowsell, O. M. Yaghi. Strategies for hydrogen storage in metal–organic frameworks. *Angew. Chem., Int. Ed.* **2005**, 44, 4670-4679.

9. Z. Xueping, Z. Jiaojiao, L. Shenglin, Q. Xuanhui, L. Ping, G. Yanbei, L. Weihua. A new soild material for hydrogen storage. *Int. J. Hydrogen energy* **2015**, 40, 10502-10507.

10. W.-X. Lim, A.W. Thornton, A. J. Hill, B. J. Cox, J. M. Hill, M. R. Hill. High performance hydrogen storage from Be-BTB metal–organic framework at room temperature. *Langmuir* **2013**, 29, 8524-8533.

11. J. M. B. V. Colbe, G. Lozano, O. Metz, T. B. Cherl, R. D. Bormann, T. Klassen, M. Dornheim. Design, sorption behaviour and energy management in a sodium alanate-based lightweight hydrogen storage tank. *Int. J. Hydrogen Energy* **2015**, 40, 2984-2988.

12. Y. Gao, X. Wu, X. C. Zeng. Design of fullerene-based frameworks for hydrogen storage. *J. Mater. Chem. A*, **2014**, 2, 5910-5914.

13. M. Fichtner. Nanotechnological aspects in materials for hydrogen storage. *Adv. Engineering Mater.* **2005**, 7, 443-455.

14. S. Chen, C. Ostrom, A. Chen. Functionalization of TiO_2 nanotubes with palladium nanoparticles for hydrogen sorption and storage. *Int. J. Hydrogen Energy* **2013**, 38, 14002-14009.

15. P. Jena. Materials for hydrogen storage: past, present, and future. *J. Phys. Chem. Lett.* **2011**, 2, 206-211.

16. H. Kobayashi, M. Yamauchi, H. Kitagawa, Y. Kubota, K. Kato, M. Takata. Atomic-level Pd−Pt alloying and largely enhanced hydrogen-storage capacity in bimetallic nanoparticles reconstructed from core/shell structure by a process of hydrogen absorption/desorption. *J. Am. Chem. Soc.* **2010**, 132, 5576-5577.

17. Z.-L. Wang, J.-M. Yan, H.-L. Wang, Y. Ping, Q. Jiang. Au@Pd core-shell nanoclusters growing on nitrogen-doped mildly reduced graphene oxide with enhanced catalytic performance for hydrogen generation from formic acid. *J. Mater. Chem. A*, **2013**, 1, 12721-12725.

18. J. Ren, N. M. Musyoka, H. W. Langmi, B. C. North, M. Mathe, X. Kang. Fabrication of core-shell MIL-101(Cr)@UiO-66(Zr) nanocresytals for hydrogen storage. *Int. J. Hydrogen Energy* **2014,** 39, 14912-14917.

19. H. Zeng, J. Li, Z. L. Wang, J. P. Liu, S. Sun. Bimagnetic core/shell FePt/Fe_3O_4 nanoparticles. *Nano Lett.* **2004**, 4, 187-190.

20. S. Mandal, P. R. Selvakannan, R. Pasricha, M. Sastry. Ions as UV-switchable reducing agents in the synthesis of Au Core−Ag shell nanoparticles. *J. Am. Chem. Soc.* **2003**, 125, 8440-8441.

21. J. Zou, S. Long, X. Chen, X. Zeng, W. Ding. Prepartion and hydrogen sorption properties of a Ni decorated Mg based Mg@Ni nano-composite. *Int. J. Hydrogen Energy* **2015**, 40, 1820-1828.

22. C. I. Covaliu, I. Jitaru, G. Paraschiv, E. Vasile, S.-Ş. Biriş, L. Diamandescu, V. Ionita, H. Iovu. Core–shell hybrid nanomaterials based on $CoFe_2O_4$ particles coated with PVP or PEG biopolymers for applications in biomedicine. *Powder Technology* **2013**, 237, 415-426.

23. S. Vaidya, A. Patra, A.K. Ganguli. CdS@TiO_2 and ZnS@TiO_2 core–shell nanocomposites: synthesis and optical properties. *Colloids and Surfaces A: Physicochem. Eng. Aspects* **2010**, 363, 130-134.

24. N. M. Sánchez-Padilla, S. M. Montemayor, L. A. Torres, F. J. Rodríguez Varela. Fast synthesis and electrocatalytic activity of M@Pt (M = Ru, Fe_3O_4, Pd) core–shell nanostructures for the oxidation of ethanol and methanol. *Int. J. Hydrogen Energy* **2013**, 38, 12681-12688.

25. K. Zhang, Y. Xiang, X. Wu, L. Feng, W. He, J. Liu, W. Zhou, S. Xie. Enhanced optical responses of Au@Pd core/shell nanobars. *Langmuir* **2009**, 25, 1162-1168.

26. N. M. Sánchez-Padilla, D. Morales-Acosta, M. D. Morales-Acosta, S. M. Montemayor, F. J. Rodrı´guez-Varela. Catalytic activity and selectivity for the ORR of rapidly synthesized M@Pt (M = Pd, Fe_3O_4, Ru) core-shell nanostructures. *Int. J. Hydrogen Energy* **2014**, 39, 16706-16714.

27. H. Kobayashi, M. Yamauchi, H. Kitagawa, Y. Kubota, K. Kato, M. Takata. Hydrogen absorption in the core/shell interface of Pd/Pt nanoparticles. *J. Am. Chem. Soc.* **2008**, 130, 1818-1819.

28. Y. Meng, D. Chen, X. Jiao. Fabrication and characterization of mesoporous Co_3O_4 core/mesoporous silica shell nanocomposites. *J. Phys. Chem. B* **2006**, 110, 15212-15217.

29. L. Wang, Y. Yamauchi. Strategic synthesis of trimetallic Au@Pd@Pt core−shell nanoparticles from poly(vinylpyrrolidone)-based aqueous solution toward highly active electrocatalysts. *Chem. Mater.* **2011,** 23, 2457-2465.

30. W. Niu, G. Xu. Crystallographic control of noble metal nanocrystals. *Nano Today* **2011**, 6, 265-285.

31. S. Chen, B. D. Adams, A. Chen. Synthesis and electrochemical study of nanoporous Pd–Ag alloys for hydrogen sorption. *Electrochim. Acta* **2010**, 56, 61-67.

32. D. Wu, Z. Zheng, S. Gao, M. Cao, R. Cao. Mixed-phase PdRu bimetallic structures with high activity and stability for formic acid electrooxidation. *Phys. Chem. Chem. Phys.* **2012**, 14, 8051-8057.

33. S. Alayoglu, A. U. Nilekar, M. Mavrikakis, B. Eichhorn. Ru-Pt core-shell nanoparticles for preferential oxidation of carbon monoxide in hydrogen. *Nat. Mater.* **2004**, 7, 333-338.

34. H.-P. Liang, N. S. Lawrence, T. G. J. Jones, C. E. Banks, C. Ducati. Nanoscale tunable proton/hydrogen sensing: evidence for surface-adsorbed hydrogen atom on architectured palladium nanoparticles. *J. Am. Chem. Soc.* **2007**, 129, 6068-6069.

35. F. Berger, M. Varga, G. Mulas, Á. Molnár, I. Dékány. Surface characteristics, hydrogen sorption, and catalytic properties of Pd−Zr alloys. *Langmuir* **2003**, 19, 3692-3697.

36. B. D. Adams, A. Chen. The role of palladium in a hydrogen economy. *Mater. Today* **2011**, 14, 282-289.

37. S. K. Konda, A. Chen. Palladium based nanomaterials for enhanced hydrogen spillover and storage. *Mater. Today* **2015**, 19, 100-108.

38. B. D. Adams, C. K. Ostrom, A. Chen. Hydrogen electrosorption into Pd−Cd nanostructures. *Langmuir* **2010**, 26, 7632-7637.

39. B. D. Adams, G. Wu, S. Nigro, A. Chen. Facile synthesis of Pd−Cd nanostructures with high capacity for hydrogen storage. *J. Am. Chem. Soc.* ***2*****009**, 131, 6930-6931.

40. B. D. Adams, C. K. Ostrom, S. Chen, A. Chen. High-performance Pd-based hydrogen spillover catalysts for hydrogen storage. *J. Phys. Chem. C* **2010**, 114*,* 19875-19882.

41. A. W. Hull. X—Ray Crystal analysis of thirteen common metals. *Phys. Rev*, **1921**, 17, 571-588.

42. C. N. Rao, K. K Rao. Effect of temperature on the lattice parameters of some silver-palladium alloys. *Can. J. Phys.* **1964,** 42, 1336.

43. N. Comisso, A. De Ninno, E. Del Giudice, G. Mengoli, P. Soldan. Electrolytic hydriding of $Pd_{79.5}Rh_{20.5}$ alloy. *Electrochim. Acta* **2004**, 49, 1379-1388.

44. A. Żurowski, M. Łukaszewski, A. Czerwiński. Electrosorption of hydrogen into palladium–rhodium alloys. *Electrochim. Acta* **2006**, 51, 3112-3117.

45. A. Chen. Electrocatalysis and photoelectrochemistry based on functional nanomaterials. *Can. J. Chem.* **2014,** 92, 581-597.

46. D. G. Narehood, S. Kishore, H. Goto, J.H. Adair, J. Nelson, H.R. Gutiérrez, P.C. Eklund. X-ray diffraction and H-storage in ultra-small palladium particles. *Int. J. Hydrogen Energy* **2009**, 34, 952-960.

Chapter 5: Significant Enhancement of Electrosorption of Hydrogen into Palladium via a Facile Annealing Process

5.1 Introduction

Metal hydrides have attracted considerable attention across diverse areas of research due to the well-known fact that hydrides may alter a wide range of the properties of metals such as their chemical, physical, and mechanical parameters. However, in a majority of reported results the witnessed changes were reversible and disappeared during the disintegration of the hydride.[1] These occurrences are thought provoking for theoretical studies and may also be efficaciously applied in practice. Metal hydrides have been predominantly identified as auspicious materials for the effective and safe storage of hydrogen.[2-7]

Palladium exhibits excellent features for real-world use as an important catalyst, encompassing an extensive diversity of applications, predominantly in organic coupling reactions,[8] hydrogen purification and storage[9] and in unique materials such as switchable mirrors[10,11] and hydrogen sensors.[12,13] The exceptional characteristics of Pd, comprising its capacity to adsorb great volumetric amounts of hydrogen at ambient temperatures and pressure (following the reversible formation of palladium hydride (PdH_x)), make it a perfect candidate for hydrogen fuel cell applications, specifically, toward the development of a hydrogen based economy.[14-19] The discovery of PdH_x occurred ~150 years ago, which comprises one of the well-studied metal/hydrogen systems. However, changes in the properties of Pd due to metal hydrides are being actively pursued.[20,21]

---

*The results presented in this chapter have been published in the *International Journal of Hydrogen Energy* **2017**, in press. (https://doi.org/10.1016/j.ijhydene.2017.03.199)

In recent years, Schwarz et al.[22] examined the unpredictably opposed performance of binary shear moduli C_{44} and $C'=1/2(C_{11} - C_{12})$ of PdH_x on the atomic portion of H/Pd. This study revealed that the opposed dependency behaviour is primarily due to the co-occurrence of two phases within the crystal referred to as alpha (α) and beta (β).[23,24] It is noteworthy that the sorption of hydrogen into the metallic structure leads to an enlargement of the metal lattice, which ultimately results in the creation of stress within the foil.[25] Internal stresses so developed within the metal can lead to cracking of metallic thin foils.

Annealing comprises a method of heating metals to an exact temperature, and then letting them to cool down at a particular rate, which eliminates internal stresses and results in a superior microstructure of crystals, referred to as grains or crystallites. It offers a well-organized way to manipulate the characteristics of metals by governing the speeds of diffusion and cooling within the microstructure.[26] The properties of the crystallites are the most critical feature that defines the kinetics of the electrosorption of hydrogen into the metals. A complete elucidation of the phase changes that occur during hydride formation is crucial for the development of a successful hydrogen based economy.

In the present study, we investigate the effect of annealing on Pd thin foils for the electrochemical hydrogen uptake. Changes in the crystal size and lattice parameters under high temperatures and following annealing have been studied in detail. The morphological and structural changes, as well as lattice parameters, played an important role in the uptake of hydrogen into the Pd thin foil. Here we address the significant issue of how annealing may affect the phase transition in Pd thin foil behaviour which results in changes in the uptake of hydrogen capacity due to stresses generated during the formation of the hydride. The Pd thin foils that were annealed under various temperatures were subjected to

electrochemical studies using cyclic voltammetry and chronoamperometric techniques for the determination of hydrogen uptake capacities.

In this chapter, Mona Amiri assisted with the spinning stage XRD experiments (Fig. 5.3). Rest of the material characterisation, analysis and the electrochemical studies were performed by me.

5.2 Experimental

5.2.1 Chemicals

The Pd foil used in this study was purchased from Sigma-Aldrich. The thickness of the Pd foil was 0.05 mm with 99.9% purity. Pd thin foil with a 0.175 cm^2 surface area was used for all in-situ temperature experiments. Sulphuric acid (99.999 %) obtained from Sigma Aldrich were used to prepare a 0.5 M H_2SO_4 electrolyte. The electrolyte was prepared using Nanopure® water (18.2 MΩ cm).

5.2.2 In-situ X-ray Diffraction Measurements

XRD patterns were obtained using a Pananalytical Xpert Pro Diffractometer with a Ni filtered monochromatic Cu Kα (1.5406 Å, 2.2 KW Max). The heating of the Pd thin foil was carried out in an Anton-Paar HTK-1200 high temperature oven chamber. A sample holder was made of aluminium oxide. Argon gas was passed throughout the in-situ XRD temperature experiments to avoid the formation of oxides on the surface of the Pd thin foil. The temperature of the Pd foils was increased at a ramp speed of 10 °C per minute; and once the sample attained a specific temperature, the XRD pattern was recorded for ~90 minutes. The sample was then cooled at a ramp rate of 5 °C per minute to room temperature. The sample was removed from the in-situ chamber, whereafter the XRD pattern was recorded using a spinning stage XRD in order to obtain superior peaks and to avoid the corundum peaks that were derived from the sample container

during the in-situ treatment. Following XRD, all of the samples were stored in an argon atmosphere at room temperature for the electrochemical measurements.

5.2.3 Physical Characterization:

The morphologies of the Pd thin foils that were annealed at different temperatures were examined using a JEOL JSM 5900LV field emission scanning electron microscope (FE-SEM). X-ray photoelectron spectrophotometry (XPS) was employed to examine the oxidation states of the Pd thin foil following the electrochemical studies using a Thermo Scientific K-Alpha XPS spectrometer. A monochromatic Al Kα (1486.6 eV) X-ray source was used with a spot size of 400 μm. The binding energy values were calibrated using the C *1s* peak at (C-C) 284.6 eV. All spectra collection and analysis were carried out using XPSPEAK 4.1 software.

5.2.4 Electrochemical Experiments:

The electrochemical behaviours of the heat treated Pd foil electrodes toward hydrogen sorption and storage were characterized using cyclic voltammetry (CV), chronoamperometry (CA), and linear scan voltammetry (LSV). A three-electrode cell system was employed for electrochemical measurements using Volta Lab PGZ402 potentiostat. A Pd thin foil with a surface area of 0.25 cm^2 was connected to a titanium rod and employed as working electrode. Platinum (Pt) wire coil with surface area of 10 cm^2 served as the counter electrode. The Pt wire was flame cleaned prior to analysis by quenching with Nanopure water. Silver/Silver Chloride (Ag/AgCl) in 1 M KCl served as the reference electrode.

The electrode potentials presented henceforth are with respect to the Ag/AgCl electrode. For the electrochemical studies 0.5 M H_2SO_4 was used as the electrolyte. To remove any dissolved oxygen that was present in the electrolyte, ultrapure argon gas (99.999%) was purged for 30 minutes prior to the electrochemical experiments. Argon gas was continuously

passed over the solution throughout the electrochemical measurements. In order to determine the time required for the complete saturation of the Pd thin foil with hydrogen, CA was performed by holding the electrode potential at a range of from -50 to -250 mV vs. Ag/AgCl for 10 minutes. LSV was carried out immediately after CA at a scan rate of 1 mV/s for the desorption of hydrogen. All of the samples were stored in an ultrapure argon environment prior to and following the electrochemical measurements, which were carried out at room temperature (20 ± 2 °C). Data collection and analysis were performed using VoltMaster 4 software.

3. Results and Discussion

5.3.1 Pd Structure and Morphology

Typical SEM images of the Pd thin foil following in-situ heat treatment are displayed in Fig. 5.1, showing that with increased temperatures during annealing, the morphology of Pd surface changed dramatically. The untreated Pd thin foil (Fig. 5.1A) showed a planar structure; while for the sample that was annealed to 300 °C (Fig. 5.1B) the surface became rough, and upon a further increase in temperature to 500 °C, the surface of the Pd thin foils became porous in nature, as pores may be clearly seen in Fig. 5.1C. The samples that were heated to higher temperatures (700 °C) (Fig. 5.1D) displayed larger grain sizes, and were perfectly aligned on the surface primarily due to the slower cooling rates during the in-situ experiments. The Pd thin foil annealed to 1000 °C (Fig. 5.1E) exhibited much larger grain boundaries; whereas the Pd thin foil annealed to 1200 °C (Fig. 5.1F) showed layered structures that were neatly arranged in a specific manner.

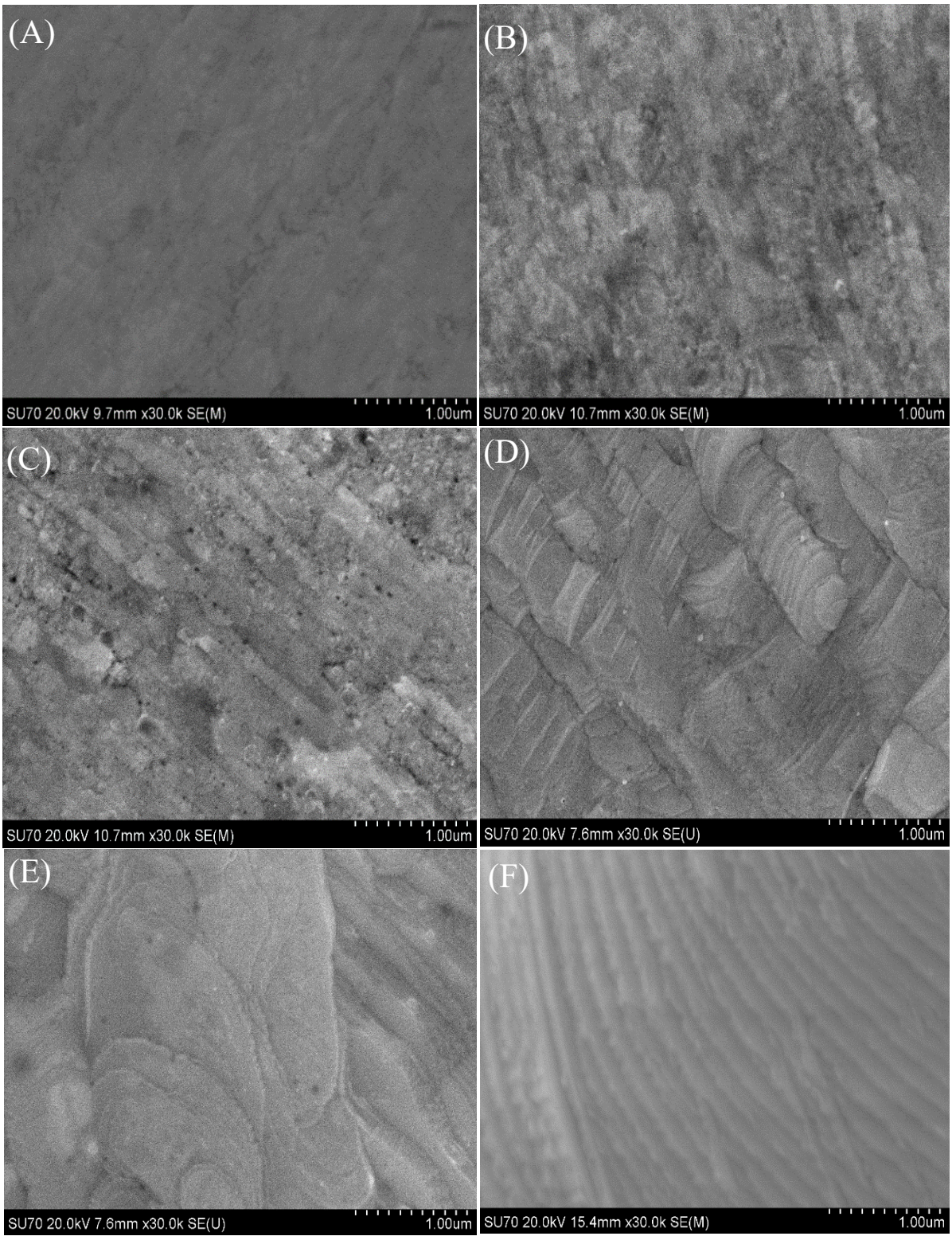

Figure 5.1: SEM images of Pd thin foils before (A) and after annealing at 300 °C (B), 500 °C (C), 700 °C (D), 1000 °C (E) and 1200 °C (F).

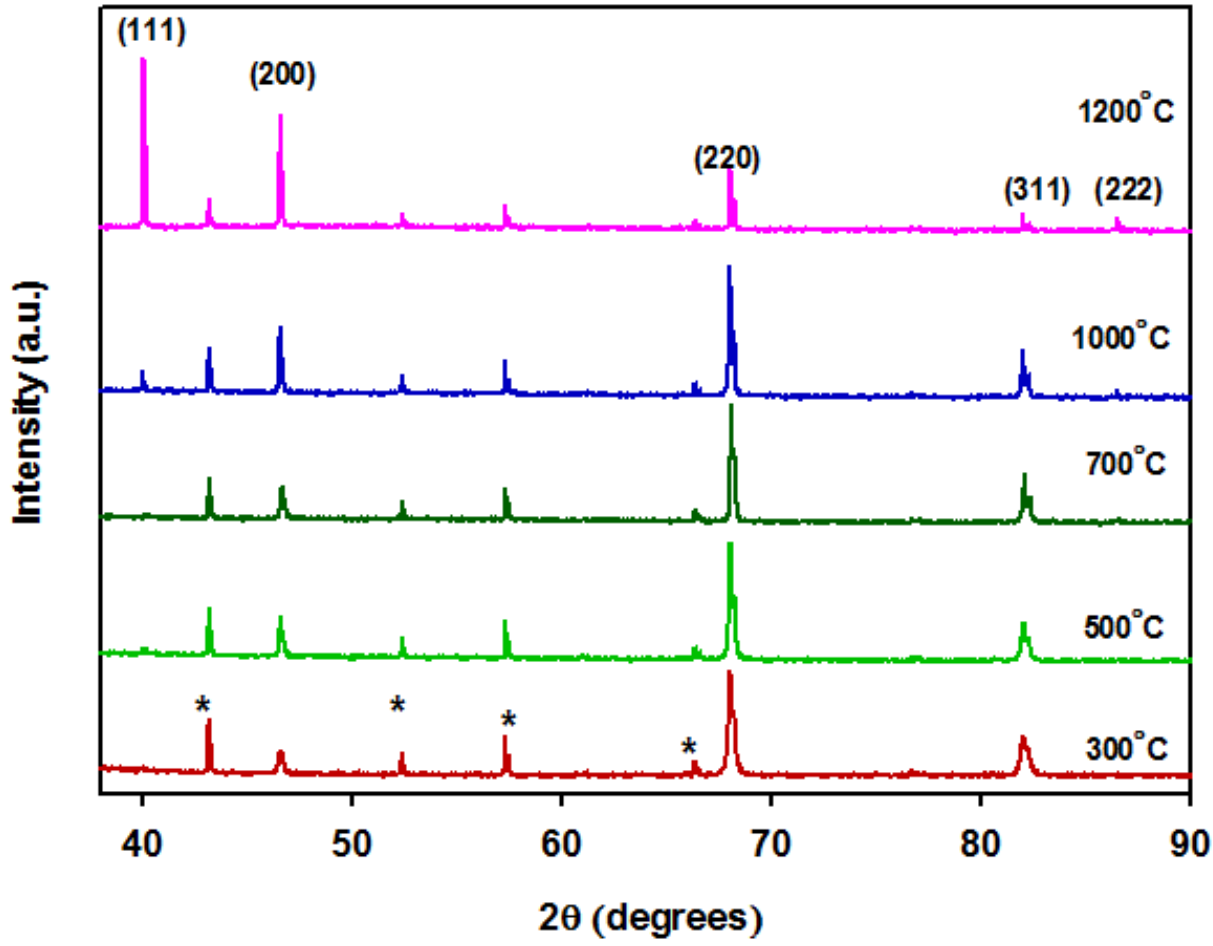

Figure 5.2: In-situ XRD patterns of the Pd thin foil during the annealing treatment at the different temperatures in the presence of Ar. * indicates the presence of corundum peaks which was used as the sample holder during in-situ XRD experiments.

Fig. 5.2 displays the XRD patterns of the Pd thin foil that were recorded during the in-situ experiments at different temperatures. As the temperature increased the peak position was slightly varied. There was a larger increase in peak intensity as the temperature was raised. The 2θ values

at 46.56°, 68.04°, and 82.05° could be indexed to the diffraction of (200), (220), and (311) planes of Pd, respectively.[27] In the case of the Pd thin foil that was heated to 700 °C, a diminutive peak was observed at 40.02°, indicating the presence of a (111) plane. The peak at 40.02° became more pronounced for the samples annealed at 1000 and 1200 °C.

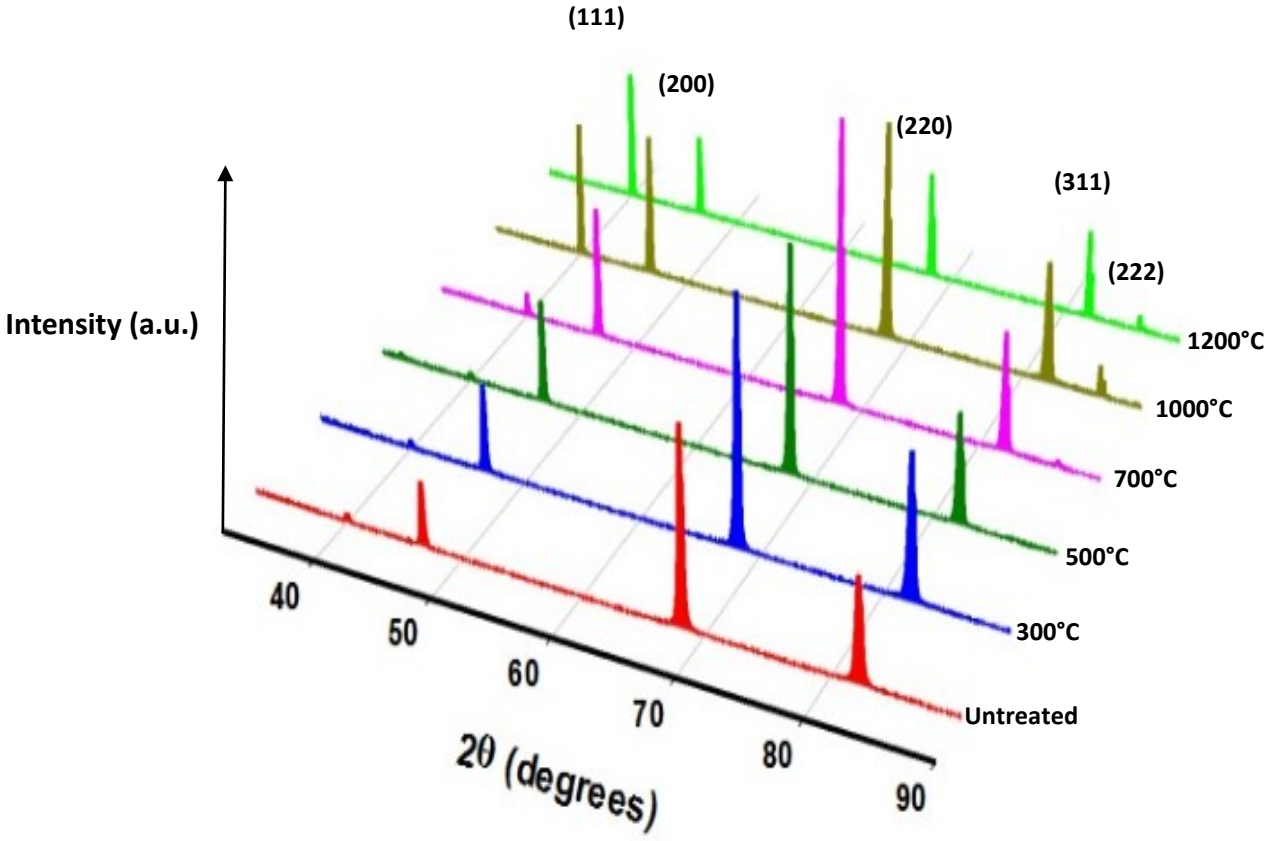

Figure 5.3: XRD patterns of Pd thin foils subjected to the annealing treatment at the different temperature listed on the figure, recorded at room temperature.

Fig. 5.3 displays the XRD patterns of the Pd thin foil that were recorded using a spinning stage XRD, following the in-situ experiments at the high temperatures. Spinning stage XRD provides better resolution of the peaks, and all of them are clearly visible. Subsequent to annealing

there was no change in the peak positions; the 2θ values at 40.02°, 46.56°, 68.04°, and 82.05° could be indexed to the diffraction of (111), (200), (220), and (311) planes of Pd, respectively .[27,28] In the case of the samples that were heated to 700, 1000, and 1200 °C, no peak for the (222) phase was not observed in the in-situ XRD measurement, whereas when using the spinning stage XRD, a diminutive peak was observed at 86.50°. All of the peaks may be referenced to a face-centered cubic Pd unit cell. The crystal size and lattice constant values were calculated using equations (5-1) and (5-2). The Scherrer equation (5-1) relates the broadening of diffraction lines with the crystal domain size and may give a good approximation of the crystallite size in the sample.[29]

$$L = \frac{\alpha\ \lambda}{\beta\ \cos\ \theta} \qquad (5\text{-}1)$$

Where L is the coherence length of the crystal domain and β is the full width in radians at the half maximum intensity (FWHM) measured at angle θ. The wavelength λ of X-ray radiation (Cu Kα = 0.15405 nm) and the constant α (a shape factor) is close to unity. Bragg's law equation can explain the appearance of a diffraction pattern through interferences of X – ray reflections from crystal planes in a sample.

$$n\lambda = 2d\sin\theta \qquad (5\text{-}2)$$

Where n is a positive integer; λ is the wavelength of incident wave; θ represents the incident angle of the incoming X-ray radiation. Bragg's law, as stated above can be used to determine the lattice spacing of a particular cubic system through the following equation:

$$d = \frac{a}{\sqrt{h^2+k^2+l^2}} \qquad (5\text{-}3)$$

Where 'a' is the lattice spacing of the cubic system, and h, k, and l are the miller indices of the Bragg's plane. Combining this relation with Bragg's law:

$$a = \frac{\lambda}{2\sin\theta}\sqrt{h^2 + k^2 + l^2} \quad (5\text{-}4)$$

The crystal size and lattice parameter values of Pd thin foil during in-situ heat treatment under various high temperatures, and following the annealing process were calculated and are listed in Table 5.1.As expected, with the increase in temperature in the in-situ chamber the crystal size of the Pd was increased, and the lattice also expanded from 3.8942 Å (untreated) to 3.9508 Å (1200 °C). However, after annealing the crystal size and the lattice constant were decreased in comparison to the corresponding in situ XRD results measured at the high temperature. Overall there were gradual increases in crystal sizes and lattice constant values with the increase of the annealing temperature. This was primarily due to the rearrangement of crystals or grains during the annealing process.

Table 5.1: Crystal size and lattice constant values of Pd thin foils during in-situ heat treatment and following annealing calculated from Figs. 5.1 and 5.2.

Sample (Pd Foil)	**In-situ Heat Treatment**		**After Annealing**	
	Crystallite Size (nm)	*Lattice Constant (Å)*	*Crystallite Size (nm)*	*Lattice Constant (Å)*
Untreated	37.91	3.8942	37.91	3.8942
300 °C	60.36	3.9070	47.23	3.8955
500 °C	108.60	3.9172	53.47	3.8973
700 °C	135.78	3.9268	57.29	3.8979
1000 °C	154.68	3.9402	62.25	3.9003
1200 °C	180.99	3.9508	95.07	3.8969

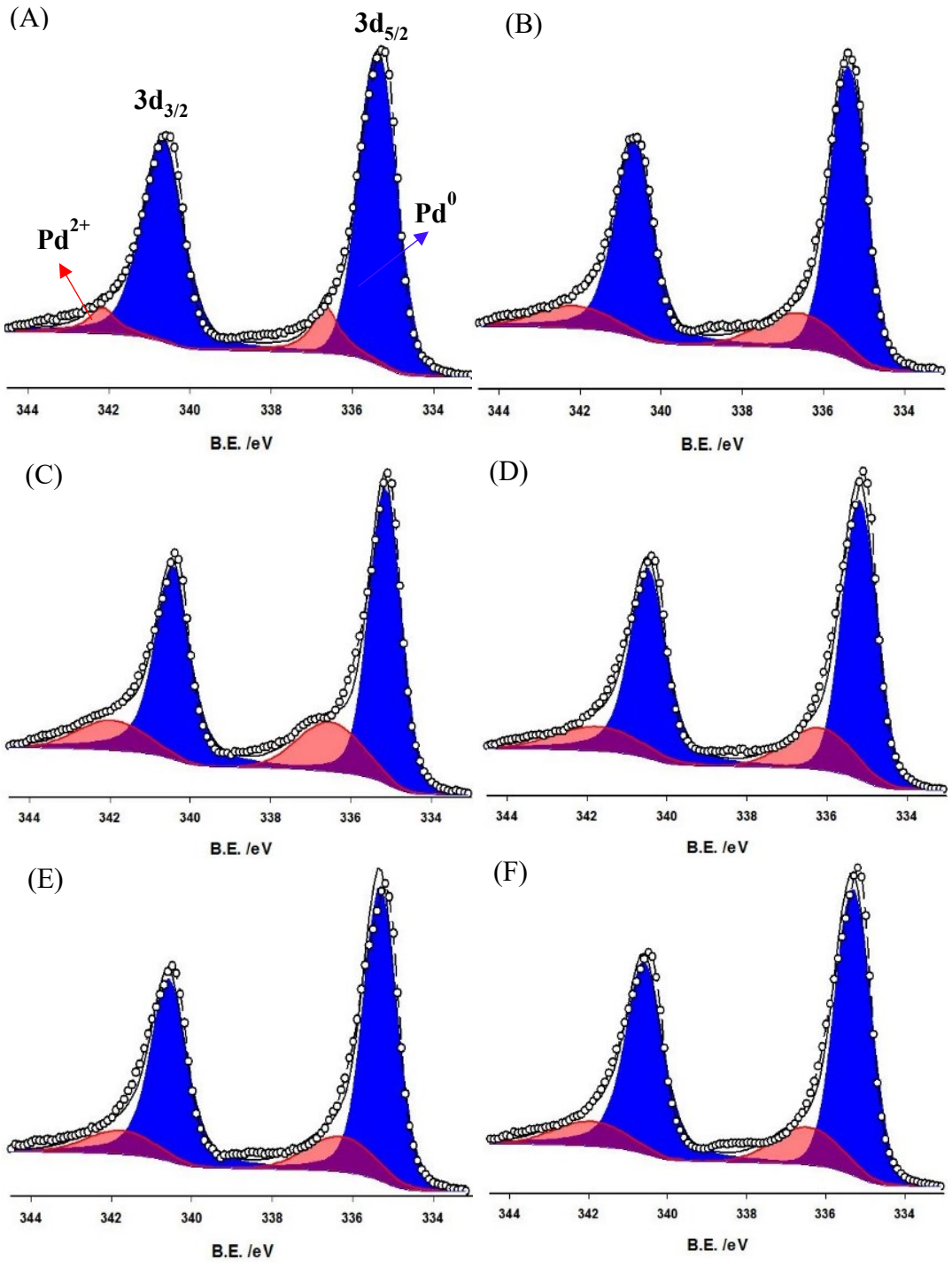

Figure 5.4: XPS spectra of Pd thin foil untreated (A) and annealed at different temperatures: 300 °C (B), 500 °C (C), 700 °C (D), 1000 °C (E) and 1200 °C (F).

A further XPS analysis was employed to determine the chemical nature of the Pd thin foil, which was annealed at various temperatures. Fig. 5.4 displays the 3d region of XPS spectra of the Pd thin foil, showing doublet peaks located at a high binding energy ($3d_{3/2}$) and a low binding energy ($3d_{5/2}$). The binding energies of all the Pd $3d_{3/2}$ and Pd $3d_{5/2}$ peaks (Figs. 5.4A to 5.4F) were measured at ~340.6 and ~335.3 eV, respectively, which were consistent with the values reported in the literature.[30] By using the area under the deconvoluted peaks of the spectra of the Pd thin foil, which was annealed under different temperatures, the oxidation states of Pd, as well as the ratio of metal to metal oxide were estimated. For comparison, Table 5.2 presents the binding energy and the Pd oxidations states of untreated Pd and Pd annealed at different temperatures.

Table 5.2: Binding energy and Pd oxidation states of untreated Pd and Pd annealed at different temperatures.

Sample (Pd Thin Foil)	**Species**	**Binding Energy (eV)**		**Relative area peak (%)**
		$3d_{3/2}$	**$3d_{5/2}$**	
Pd untreated	Pd(0)	340.6	335.3	88.1
	Pd(II)	342.1	336.6	11.9
Pd (300 °C)	Pd(0)	340.6	335.3	81.8
	Pd(II)	342.1	336.6	18.2
Pd (500 °C)	Pd(0)	340.4	335.1	78.1
	Pd(II)	341.9	336.5	21.9
Pd (700 °C)	Pd(0)	340.4	335.1	78.7
	Pd(II)	341.7	336.1	21.3
Pd (1000 °C)	Pd(0)	340.5	335.3	82.5
	Pd(II)	341.7	336.3	17.5
Pd (1200 °C)	Pd(0)	340.5	335.3	81.6
	Pd(II)	341.9	336.4	18.4

5.3.2 Electrosorption of Hydrogen into Pd

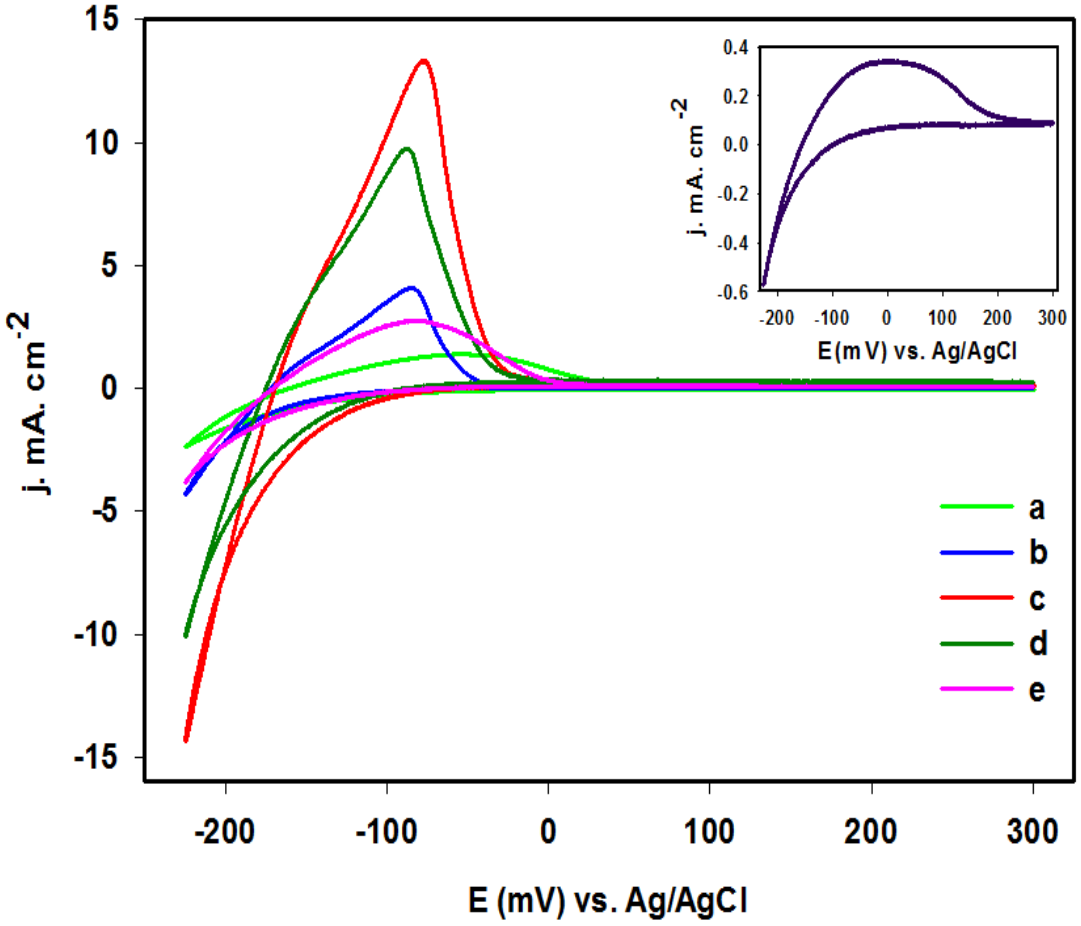

Figure 5.5: CVs of Pd thin foil annealed at 300 °C (a), 500 °C (b), 700 °C (c), 1000 °C (d) and 1200 °C (e), recorded in 0.5 M H_2SO_4 at a scan rate of 1 mV/s. Inset: the CV of the Pd thin foil that was not treated.

Fig. 5.5 displays the CVs of the Pd thin foil prior to and following the annealing recorded in 0.5 M H_2SO_4 between -225 and 300 mV vs. Ag/AgCl at the scan rate of 1 mV/s. Two main regions were observed in these CVs: the potential of -225 to 25 mV relates to the hydrogen adsorption/absorption and desorption region; whereas the potential range between 25 to 300 mV denotes the double-layer region.[31] For all of the samples, when the electrode potential was scanned from 300 to -225 mV, hydrogen adsorption/absorption began at around -80 mV. The cathodic current increased when the potential was scanned from -80 to -225 mV, and no adsorption/absorption peaks were observed. Although it was difficult to distinguish the absorption and the adsorption process, the high current was predominantly produced by the hydrogen absorption, which dominated the hydrogen adsorption process.[32] When the electrode potential was scanned from -225 to 300 mV vs Ag/AgCl, a large peak appeared at -80 mV due to the desorption of hydrogen. The peak current was increased with the increase of the annealing temperature from 300 to 700 °C; but decreased with the further increase in the annealing temperature. All of the orbed hydrogen was completely desorbed below 50 mV vs Ag/AgCl. For comparison, the inset of Fig. 5.5 presents the CV of the untreated Pd thin foil; a small and very broad hydrogen desorption peak was observed, indicating that the annealing process significantly improved the kinetics of hydrogen absorption and desorption.

The total charge of the hydrogen desorption was calculated by integrating the desorption peak and was found to be in the following order: Untreated (56.28 mC) < 300 °C (212.05 mC) < 500 °C (267.12 mC) < 1200 °C (269.13 mC) < 1000 °C (670.77 mC) < 700 °C (819.13 mC), respectively. This indicated that the annealing of the Pd thin foil played an important role in increasing the uptake of hydrogen. Significant changes in the hydrogen sorption capacities were mainly due to the changes in the morphology of Pd thin foil due to annealing at various

temperatures as shown in Fig. 5.1, as well as the changes in the crystal structure and lattice constant values mentioned in Table. 5.1. It was primarily due to the rearrangement of crystals or grains during the annealing process, which resulted in expansion of the lattice.

A chronoamperometry (CA) technique was utilized to determine the time required for the Pd thin foil (not annealed) to completely desorb hydrogen, by holding the electrode potential at a constant -220 mV for different time periods, ranging from 1, 3, 5, 7, 10, and 12 minutes, immediately scanning the electrode potential from -220 to 300 mV vs Ag/AgCl at a 1 mV/s scan rate using a LSV technique, as shown in Fig. 5.6A. It was observed that by successive increments of the holding time, from 1 to 12 minutes, the hydrogen desorption charge current was also increased. Initially, for the one-minute holding time, the hydrogen desorption peak centered at -60 mV. As the holding time increased, the peak was shifted to a more positive potential and the peak also become more broad in nature, which indicated a large quantity of hydrogen desorption taking place. The Q_H was estimated by integrating the hydrogen desorption current from the LSV curves (Fig. 5.6A) recorded after the different holding time. The Q_H versus the holding time plot is depicted in Fig. 5.6B, following the order: $1 < 3 < 5 < 7 < 12 < 10$ minutes, showing that highest hydrogen sorption capacity was attained within a 10-minute holding.

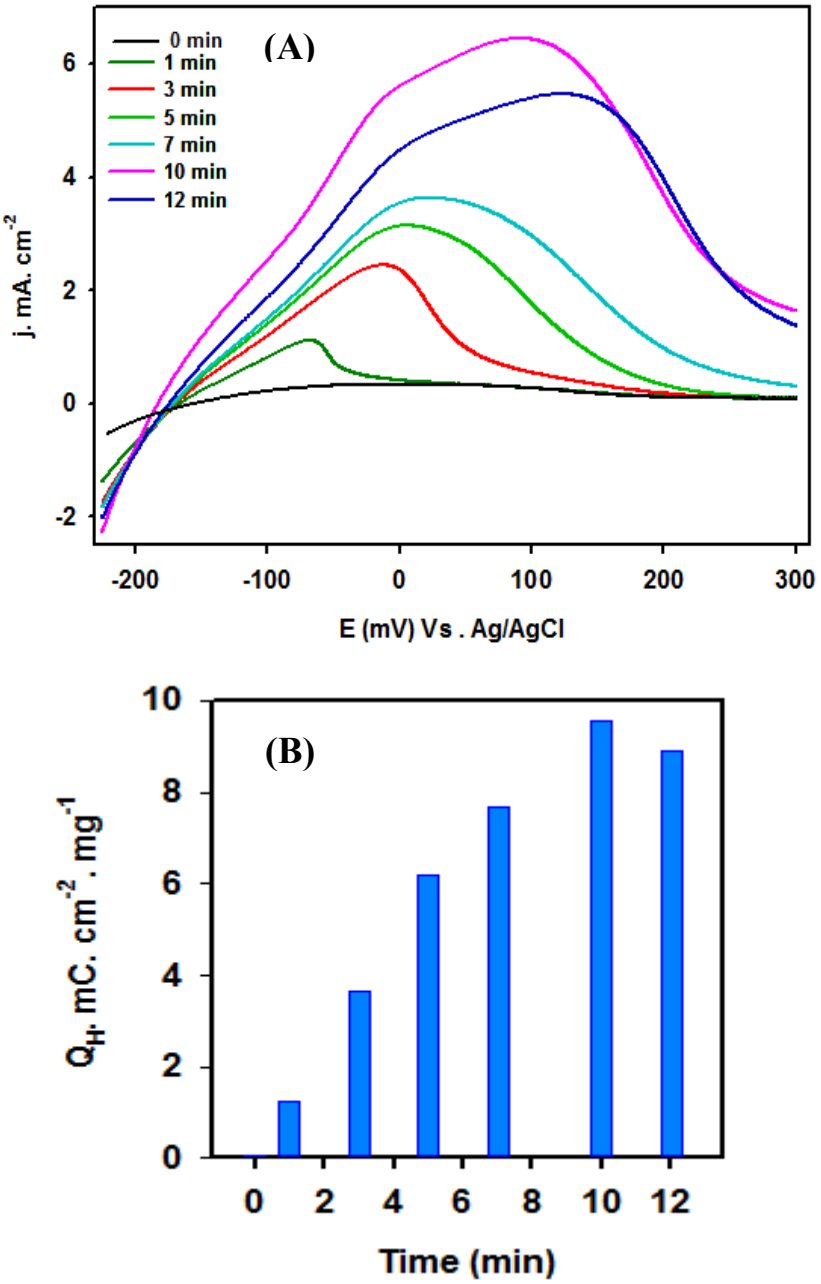

Figure 5.6: (A) LSVs of the Pd thin foil after being held at -220 mV for the different periods of time. Solution: 0.5 M H_2SO_4; Scan rate: 1 mV/s. (B) Hydrogen desorption charge Q_H versus the holding time.

To examine the effects of the held electrode potential on hydrogen sorption capacity, CA was performed with a constant holding time (10 minutes) at various electrode potentials ranging from -50 to -250 mV vs. Ag/AgCl; immediately followed by LSV, where the electrode potential was scanned from the held potential to 300 mV at 1 mV/s scan rate in 0.5 M H_2SO_4. Fig. 5.7A presents the LSV curves of the Pd thin foil that was not annealed, when the held electrode potential was lowered from -50 mV to -170 mV vs Ag/AgCl, where there was an increase in peak intensity. When the held potential was further lowered from -180 mV to -250 mV, there was an increase in the peak current as well as a positive shift in the peak potential. Fig. 5.7B presents the LSV curves of a Pd thin foil after being annealed at 700 °C for ~90 minutes, which were recorded in 0.5 M H_2SO_4 at a 1 mV/s scan rate.

Initially it followed a similar trend as the Pd thin foil, which was not annealed when the electrode potential was held from -50 to -170 mV, but the current density was much higher. Whereas when the held electrode potential was lowered to -180 to -200 mV, the hydrogen desorption current was increased significantly and the peak potentials were shifted positively. Contrastingly, on further lowering of the held potential from -200 to -250 mV, the peak current was slightly increased and almost no peak potential shift was seen. Below -180 mV, the desorption of hydrogen from the Pd thin foil was not complete, this is due to the slower kinetic behaviour of the bulk Pd. whereas complete desorption of hydrogen was seen in case of Pd nanoparticles (Chapter 4). Similar trends were also observed with the other annealed samples, representing the fact that the level of hydrogen uptake capacity into the Pd thin foil was dependent on the applied electrode potential. Under electrochemical environments, the lower potential of the electrode corresponded to a greater hydrogen pressure in the gas-phase analysis.[33,34]

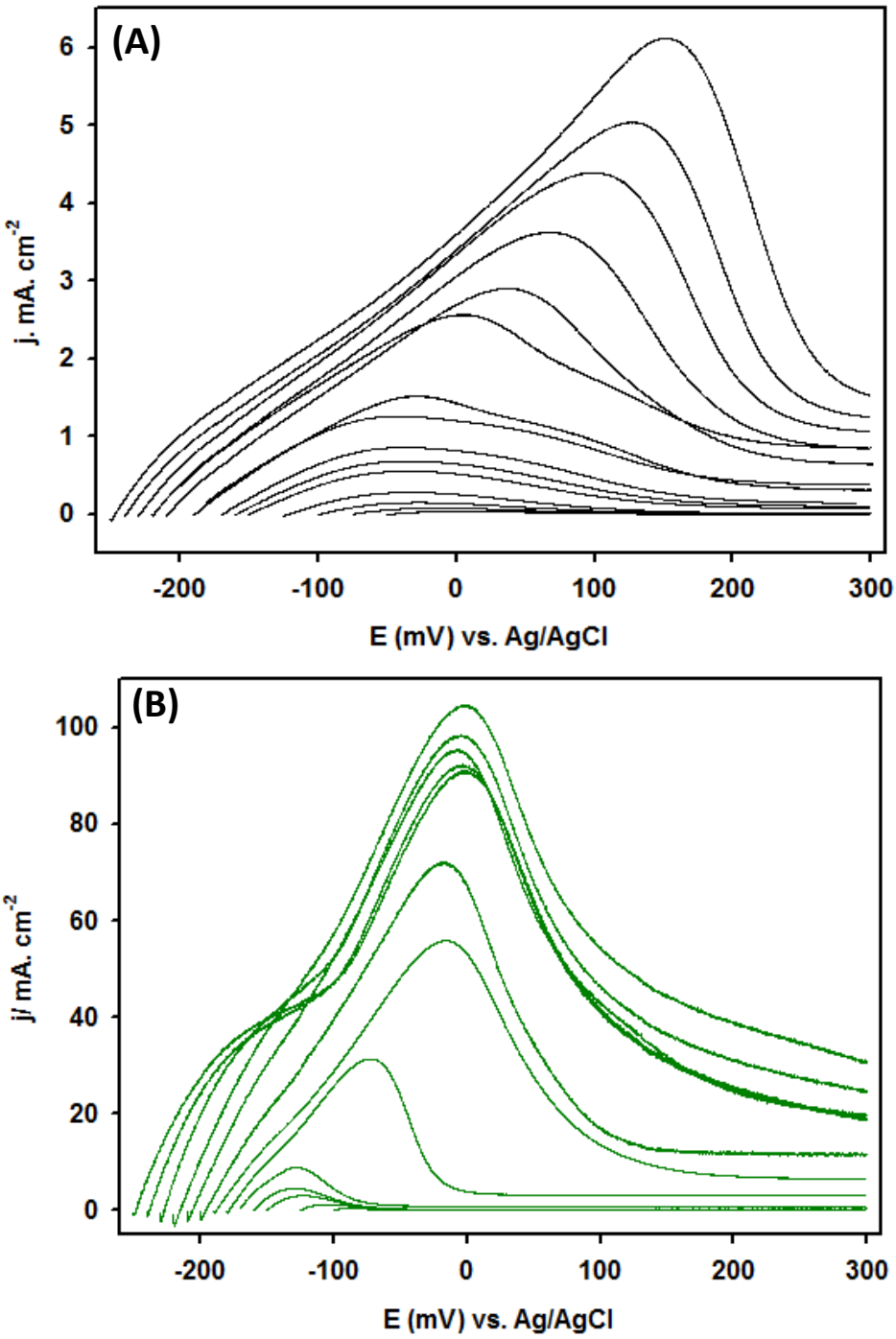

Figure 5.7: LSVs of the untreated Pd foil (A) and the Pd foil annealed at 700 °C (B) recorded after being held at different potentials for 10 minutes.

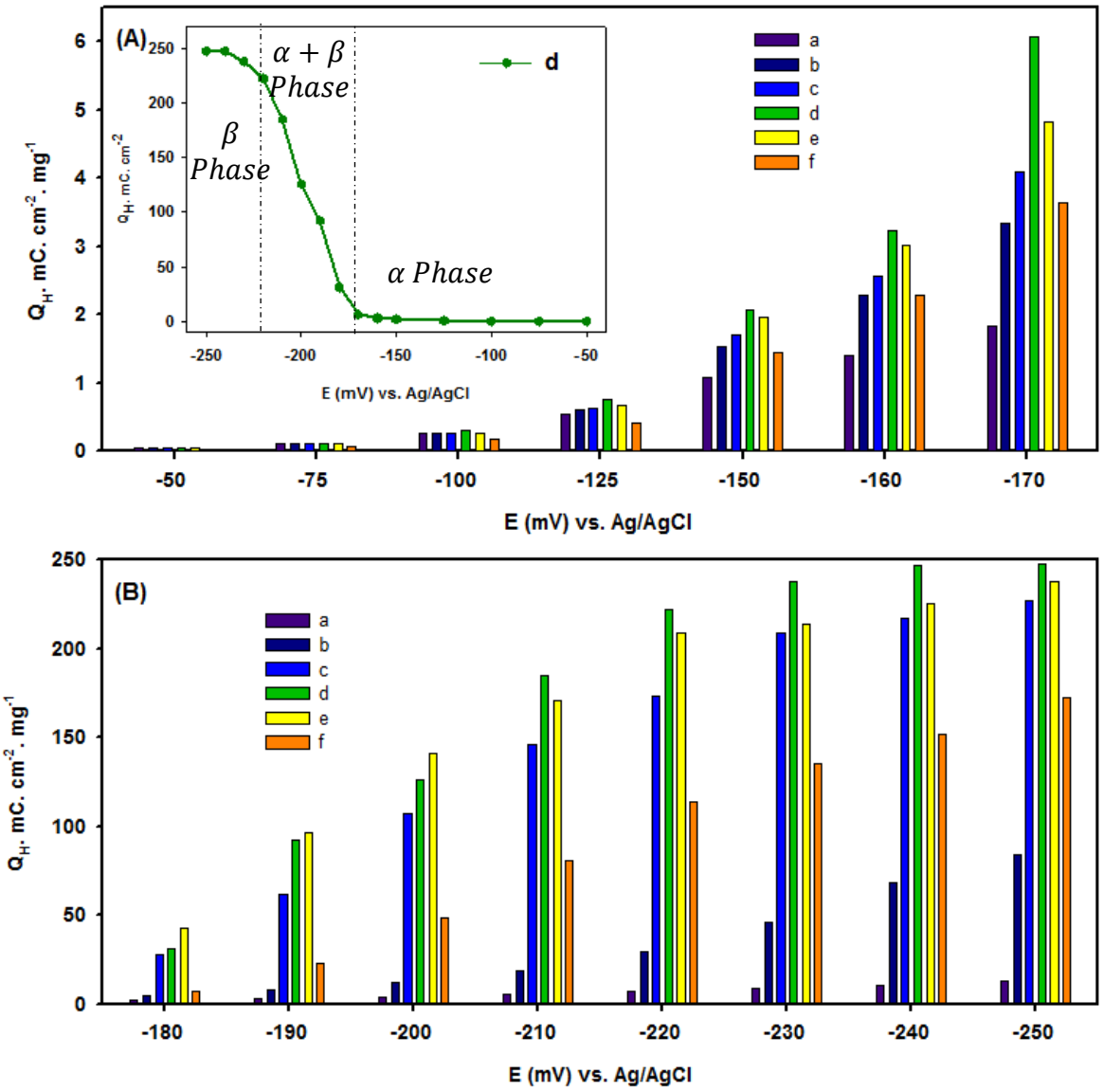

Figure 5.8: The overall hydrogen desorption charge Q_H versus the held electrode potential of -50 to -170 mV (A), -180 to -250 mV (B). Pd foil untreated (a) and annealed at different temperatures at 300 °C (b), 500 °C (c), 700 °C (d), 1000 °C (e) and 1200 °C (f). Inset of (A): the overall trend (Q_H) of the Pd foil annealed at 700 °C.

To determine the total hydrogen desorption/oxidation charge, the peak area under the LSV curves was integrated from Figs. 5.7A and 5.7b. Fig. 5.8 presents the total hydrogen desorption charges (Q_H) against the held potential vs Ag/AgCl. It is known that hydrogen uptake may undergo two different phases, referred to as α phase and β phase.[35] The α phase represents a solid solution phase, where the interstitial sites of the Pd are partially occupied by hydrogen. When the interstitial sites are completely occupied, the formation of metal hydride takes place to form the β phase, resulting in an increase in the lattice constant.

For clarification, Fig. 5.8A presents the α phase hydrogen uptake capacity of the untreated Pd thin foil (a) and the thin foils after being annealed at 300 °C (b), 500 °C (c), 700 °C (d), 1000 °C (e) and 1200 °C (f), where the held electrode potential was varied from -50 to -170 mV vs Ag/AgCl; and the corresponding mixed α and β phase as well as β phase hydrogen uptake capacity is displayed in Fig. 5.8B. The hydrogen uptake capacity was increased with the decrease of the held electrode potential from -50 to -250 mV. The inset of Fig. 5.8A presents the total desorption charge of the hydrogen versus the held electrode potential at the Pd thin foil, which was annealed at 700 °C. The electrode potential range above -170 mV corresponded to the α phase hydrogen sorption, where the amount of the hydrogen uptake was gradually increased with the decrease of the potential from -50 to -170 mV and the overall hydrogen sorption was low. The potential range below -220 mV corresponded to the β phase hydrogen storage, which was approximately 37 times higher than the α phase hydrogen sorption. The electrode potentials between -170 and -220 mV represented the α phase and β phase transition region, where the Q_H was significantly increased from 6.05 mC to 222.5 mC when the held electrode potential was decreased from -170 to -220 mV.

As seen in Figs. 5.8A and 5.8B, the annealing treatment had a strong positive impact on the hydrogen uptake capacity of the Pd foil, which was increased with the increase of the annealed temperature from 300 °C to 700 °C; but it was decreased with the further increase in annealing temperature from 700 °C to 1200 °C. For example, for the α phase hydrogen sorption when the electrode potential was held at -170 mV, the uptake hydrogen capacity Q_H of the Pd foil was increased in the following order: 1.84 mC (untreated) < 3.34 mC (annealed @ 300 °C) < 3.63 mC (@ 1200 °C) < 4.10 mC (@ 500 °C) < 4.82 mC (@ 1000 °C) < 6.05 mC (@ 700 °C). The Pd foil that was annealed at 700 °C showed the highest hydrogen sorption capacity, which was 3.2 times larger than that of the untreated Pd foil. In the case of the β phase hydrogen storage when the electrode potential was held at -250 mV, the uptake hydrogen capacity Q_H of the Pd foil was increased in the following order: 12.7 mC (untreated) < 84.3 mC ((annealed @ 300 °C) < 172.8 mC (@ 1200 °C) < 227.3 mC (@ 500 °C) < 237.4 mC (@ 1000 °C) < 247.4 mC (@ 700 °C). The Pd foil that was annealed at 700 °C showed a 19.4-fold increase in hydrogen uptake capacity in comparison to the untreated foil.

5.4 Conclusion

In summary, for the first time the effect of annealing on the electrosorption of hydrogen into Pd thin foil was studied using in-situ XRD and electrochemical methods. The Pd thin foil was morphologically and structurally characterized by SEM, XRD, and XPS, as well as being electrochemically studied using CV, CA, and LSV to elucidate the electrochemical kinetics of hydrogen uptake and release. The capacity for the hydrogen sorption and storage depends on the morphology, crystal structure and lattice parameters of the formed Pd thin foil, as well as the applied electrode potential. The presence of α and β phases, as well as the phase transition were clearly observed and identified with respect to the applied electrode potential. The Pd foil that was

annealed at 700 °C showed the highest hydrogen uptake capacity, a 3.2-fold increase in the α phase hydrogen storage and a 19.4-fold increase in the β phase hydrogen storage in comparison to the un-annealed one. The present study not only provided insights in the hydrogen sorption, but also demonstrated that a facile annealing process could significantly enhance the hydrogen uptake and storage capacity of Pd.

References

1. R. Nowakowski, P. Grzeszczak, R. Dus. Hydrogen-induced stress relaxation in thin Pd films: influence of carbon implementation. *Langmuir* **2007,** 23, 1752-1758.

2. C. Zhou, J. A. Szpunar, X. Cui. Synthesis of Ni/graphene nanocomposite for hydrogen storage. *ACS Appl. Mater. Interfaces* **2016,** 8, 15232-15241.

3. P. Jena. Materials for hydrogen storage: past, present, and future. *J. Phys. Chem. Lett.* **2011,** 2, 206-211.

4. F. Schuth, B. Bogdanovic, M. Felderhoff. Light metal hydrides and complex hydrides for hydrogen storage. *Chem. Comm.* **2004,** 20, 2249-2258.

5. L. Schlapbach, A. Zuttel. Hydrogen-storage materials for mobile applications. *Nature* **2001,** 414, 353-358.

6. V. Bérubé, G. Radtke, M. Dresselhaus, G. Chen, Size effects on the hydrogen storage properties of nanostructured metal hydrides: a review. *Int. J. Energ. Res.* **2007,** 31, 637-663.

7. S. S. Mohammadshahi, E. M. Gray, C. J. Webb. A review of mathematical modelling of metal-hydride systems for hydrogen storage applications. *Int. J. Hydrogen. Energ.* **2016,** 41, 3470-3484.

8. S. S. Stahl. Palladium oxidase catalysis: selective oxidation of organic chemicals by direct dioxygen-coupled turnover. *Angew. Chem. Int. Edit.* **2004,** 43, 3400-3420.

9. S. K. Konda, A. Chen. Palladium based nanomaterials for enhanced hydrogen spillover and storage. *Mater. Today* **2016,** 19, 100-108.

10. A. Borgschulte, R. J. Westerwaal, J. H. Rector, B. Dam, R. Griessen, J. Schoenes. Effect of the strong metal-support interaction on hydrogen sorption kinetics of Pd-capped switchable mirrors. *Phys. Rev. B* **2004,** 70, 155414.

11. J. W. J. Kerssemakers, S. J. van der Molen, N. J. Koeman, R. Gunther, R. Griessen. Pixel switching of epitaxial Pd/YHx/CaF_2 switchable mirrors. *Nature* **2000,** 406, 489-491.

12. H. Yan, X. Zhao, C. Zhang, C. Q.-Z. Li, J. Cao, D.-F. Han, H. Hao, M. Wang. A fast response hydrogen sensor with Pd metallic grating onto a fiber's end-face. *Opt. Commun.* **2016,** 359, 157-161.

13. M. Krishna Kumar, S. Ramaprabhu. Palladium dispersed multiwalled carbon nanotube based hydrogen sensor for fuel cell applications. *Int. J. Hydrogen. Energ.* **2007,** 32, 2518-2526.

14. E. Antolini. Palladium in fuel cell catalysis. *Energ. Environ. Sci.* **2009,** 2, 915-931.

15. S. Chen, C. Ostrom, A. Chen. Functionalization of TiO_2 nanotubes with palladium nanoparticles for hydrogen sorption and storage. *Int. J. Hydrogen. energ.* **2013,** 38, 14002-14009.

16. Y. Tang, X. Chi, S. Zou, X. Zeng. Facet effects of palladium nanocrystals for oxygen reduction in an ionic liquid and sensing applications. *Nanoscale* **2016**, 8, 5771-5779.

17. A. Chen, C. Ostrom. Palladium-based nanomaterials: synthesis and electrochemical applications. *Chem. Rev.* **2015,** 115, 11999-12044.

18. B. D. Adams, C. K. Ostrom, A. Chen. Hydrogen electrosorption into Pd−Cd nanostructures. *Langmuir* **2010,** 26, 7632-7637.

19. E. Masika, R. A. Bourne, T. W. Chamberlain, R. Mokaya. Supercritical CO_2 mediated incorporation of Pd onto templated carbons: a route to optimizing the Pd particle size and hydrogen uptake density. *ACS Appl. Mater. Interfaces* **2013,** 5, 5639-5647.

20. B. M. Geerken, R. Griessen, L. M. Huisman, E. Walker. Contribution of optical phonons to the elastic moduli of Pd H_x and Pd D_x. *Phys. Rev. B* **1982,** 26, 1637-1650.

21. L. A. Nygren, R. G. Leisure. Elastic constants of α'-phase PdH_x over the temperature range 4 - 300 K. *Phys. Rev. B* **1988,** 37, 6482-6485.

22. R. B. Schwarz, H. T. Bach, U. Harms, D. Tuggle. Elastic properties of Pd–hydrogen, Pd–deuterium, and Pd–tritium single crystals. *Acta Mater.* **2005,** 53, 569-580.

23. A. N. R. Bos, K. R. Westerterp. Mechanism and kinetics of the selective hydrogenation of ethyne and ethene. *Chem. Eng. Process: Process Intensification* **1993,** 32, 1-7.

24. A. V. Ledovskikh, D. L. Danilov, M. Vliex, P. H. L. Notten. Modeling and experimental verification of the thermodynamic properties of hydrogen storage materials. *Int. J. Hydrogen. Energ.* **2016,** 41, 3904-3918.

25. U. Laudahn, A. Pundt, M. Bicker, U. V. Hülsen, U. Geyer, T. Wagner, R. Kirchheim. Hydrogen-induced stress in Nb single layers. *J. Alloy. Compd.* **1999,** 293–295, 490-494.

26. J. L. Dossett, H. E. Boyer. Practical heat treating. *ASM International* **2006**, 2-6.

27. L. Arroyo-Ramírez, R. Montano-Serrano, T. Luna-Pineda, F. R. Román, R. G. Raptis, C. R. Cabrera. Synthesis and characterization of palladium and palladium–cobalt nanoparticles on vulcan XC-72R for the oxygen reduction reaction. *ACS Appl. Mater. Interfaces* **2013,** 5, 11603-11612.

28. S. Navaladian, B. Viswanathan, T. Varadarajan, R. Viswanath. A rapid synthesis of oriented palladium nanoparticles by UV irradiation. *Nanoscale Res. Lett.* **2008,** 4, 181-186.

29. S. Chen, M. Malig, M. Tian, A. Chen. Electrocatalytic activity of PtAu nanoparticles deposited on TiO_2 nanotubes. *J. Phys. Chem. C* **2012,** 116, 3298-3304.

30. S. Fu, C. Zhu, D. Du, Y. Lin. Facile one-step synthesis of three-dimensional Pd–Ag bimetallic alloy networks and their electrocatalytic activity toward ethanol oxidation. *ACS Appl. Mater. Interfaces* **2015,** 7, 13842-13848.

31. S. K. Konda, C. K. Ostrom, A. Chen. Synthesis and electrochemical study of Cd@Pd core/shell nanomaterials for hydrogen sorption and storage. *Int. J. Hydrogen. Energ.* **2015,** 40, 16365-16374.

32. C. Gabrielli, P. P. Grand, A. Lasia, H. Perrot. Investigation of hydrogen adsorption and absorption in palladium thin films: II. cyclic voltammetry. *J. Electrochem. Soc.* **2004,** 151, A1937-A1942.

33. N. Comisso, A. De Ninno, E. Del Giudice, G. Mengoli, P. Soldan, Electrolytic hydriding of $Pd_{79.5}Rh_{20.5}$ alloy. *Electrochim. Acta* **2004,** 49, 1379-1388.

34. A. Żurowski, M. Łukaszewski, A. Czerwiński. Electrosorption of hydrogen into palladium–rhodium alloys. *Electrochim. Acta* **2006,** 51, 3112-3117.

35. D. G. Narehood, S. Kishore, H. Goto, J. H. Adair, J. A. Nelson, H. R. Gutiérrez, P.C. Eklund. X-Ray diffraction and H-storage in ultra-small palladium particles. *Int. J. Hydrogen. Energ.* **2009,** 34, 952-960.

Chapter 6: One-step Synthesis of Pd and Reduced Graphene Oxide Nanocomposites for Enhanced Hydrogen Sorption and Storage

6.1. Introduction

Hydrogen storage materials have garnered much attention due to their critical applications in a hydrogen economy.[1] The Department of Energy (DOE) has set an ultimate target for hydrogen storage materials: 6.5 wt.% of stored hydrogen with a volume density of 62 kg/m^3 of hydrogen at ambient temperatures for applications in fuel cell powered vehicles.[2] Current hydrogen storage methods, such as high pressure hydrogen gas, liquid hydrogen tanks, metal hydrides, complex metal hydrides, and metal organic frameworks have not yet met these DOE targets.[3] Solid-state hydrogen storage materials are presently attractive as they are cost effective and safe.[4] Pd is of particular interest in this area due to its high affinity for hydrogen sorption.[5] Typically, in the absence of protective agents, metallic nanoparticles (NPs) tend to aggregate due to attractive molecular van der Waals forces. To overcome this aggregation, toward improving their morphology and catalytic activity, they are commonly deposited on solid supports that possess larger surface area.[6,7] It is recognized that hydrogen molecular dissociation takes place at the Pd surface, and that dissociated hydrogen atoms occupy its interstitial sites.[8,9] Hydrogen sorption and storage may be augmented at room temperature by a phenomenon called the "spillover effect", which is defined as the chemical dissociation of hydrogen molecules on metallic NPs in the form of atomic hydrogen, and the subsequent migration of these hydrogen atoms onto adjacent surfaces of the adsorbate via surface diffusion.[10,11,12]

---

*The results presented in this chapter have been published in *Electrochemistry Communications* **2015**. 60, 148-152.

Recently, graphene-based nanomaterials have proven to be potential candidates for hydrogen sorption and storage in various science and technology applications due to their remarkable attributes including extensive surface areas, high catalytic activity and stability, and elevated thermal and electrical conductivity.[13-18] The primary advantage of graphene is that all of its atoms are exposed at its surface, which are highly sensitive to adsorbed molecules, thus it exhibits robust electron transport properties. The deposition of metallic NPs onto graphene sheets utilizing conventional methods involves the use of complex reductants and surfactants, which tend to block a percentage of the active sites on the graphene oxide surface, thereby reducing catalytic activity.[19] Recently, the electrochemistry of graphene-based nanostructures has received much interest as they have the capacity to enable applications in numerous fields.[20-23] Therefore, intense efforts are being invested toward the development of a simplistic and environmentally compatible technique for the synthesis of graphene nanocomposites. In the present study, we report a one-step facile electrochemical approach method for the simultaneous synthesis Pd NPs and reduced GO (rGO) nanocomposites for promising applications in hydrogen sorption and storage.

6.2. Experimental

Graphene oxide (4mg/mL), Pd nitrate (99.99%), and Nafion (10%) were purchased from Sigma-Aldrich; and all other analytical reagents were used as received. Pure water (18.2 MΩ cm) produced by a NANOpure water system was employed in the preparation of all solutions. Scanning electron microscopic (SEM) and energy-dispersive X-ray spectroscopic (EDX) characterizations were carried out using a Hitachi SU-70. Thermo Scientific K-Alpha X-ray photoelectron spectroscopy (XPS) was employed to study the composition and oxidation states of the Pd/rGO nanocomposites prior to and following reduction. The samples were run at a takeoff angle (relative to the horizontal surface) of 90°. A monochromatic Al Kα X-ray source was employed with a spot

size of 400 µm. A VoltaLab PGZ 402 potentiostat was employed to conduct electrochemical measurements using a three electrode cell system. A glassy carbon electrode (GCE) with a geometric surface area of 0.1964 cm^2 was utilized as the working electrode, a silver/silver chloride (Ag/AgCl) saturated KCl solution served as the reference electrode, and a platinum coil was used as the counter electrode. All electrochemical experiments were conducted at room temperature (20 ± 2°C).

The fabrication of Pd/rGO nanocomposites was achieved via the in situ electrochemical reduction of the GO and Pd precursors. The GCE surface was polished with alumina powder (0.5 µm) followed by sonication in pure water for 1 min. A 20 µL mixture of GO (0.5 mg/mL), $Pd(NO_3)_2$ (10mM) and Nafion (5%) was cast on the GCE and then allowed to air dry. The in situ formation of Pd NPs and rGO nanocomposites on the GCE was achieved using cyclic voltammetry (CV) in 0.1 M Na_2SO_4 (pH 7) by cycling the electrode potential between +0.5 V and -1.2 V (vs Ag/AgCl) at 10 mVs for ten cycles. For comparison, pure Pd particles and rGO were prepared using the identical electrochemical approach, with the amount of Pd precursor and Nafion used for the synthesis of the pure Pd particles and the Pd/rGO nanocomposite the same.

6.3. Results and discussion

6.3.1 Surface Characterization

Fig. 6.1 depicts SEM images of the electrochemically reduced GO (A), Pd nanoparticles (B), and the Pd/rGO nanocomposite (C). The rGO exhibited a wrinkled texture with a larger surface area. The electrochemical reduction of pure Pd resulted in a larger particle size, whereas in the case of the Pd/rGO nanocomposite, the SEM image revealed the average particle size of 7 nm, which were uniformly dispersed on rGO sheets with high density. Fig. 6.1D shows the EDX spectra of rGO, pure Pd, and the Pd/rGO nanocomposite, confirming the existence of carbon, oxygen in the case

of rGO (black curve), presence of carbon, oxygen and Pd in the case of pure Pd particles (blue curve) were observed, carbon peak is due to the usage of carbon tape in SEM as sample substrate and oxygen peak could be due to the atmospheric exposure of sample. Presence of carbon, oxygen and Pd in the case of the Pd/rGO nanocomposite were identified (red curve). The fluorine peak in all samples was due to the incorporation of Nafion as a binder.

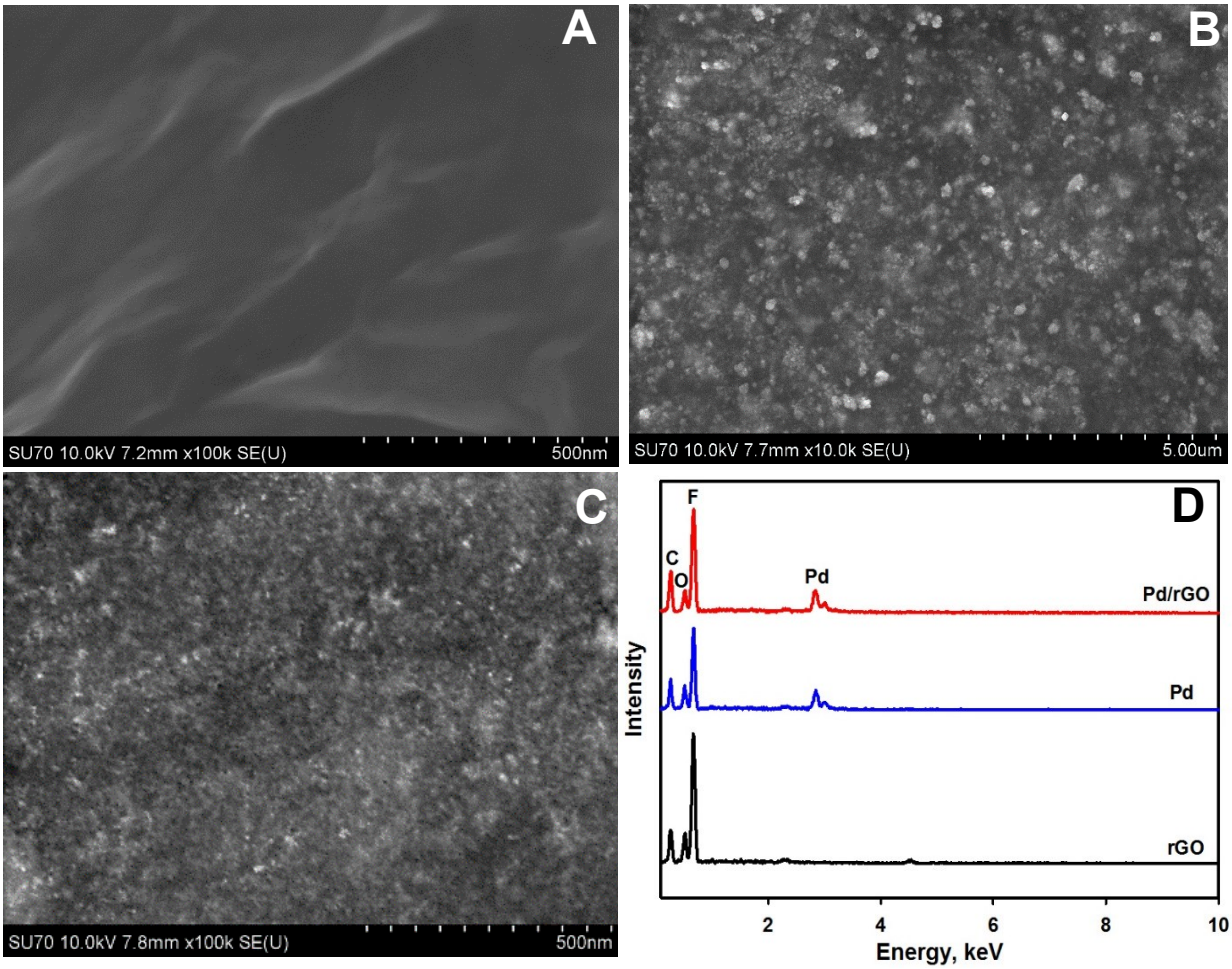

Figure 6.1: SEM images of reduced graphene oxide, pure Pd, and the Pd/rGO nanocomposite (A, B and C). EDX spectra (D) of rGO (black), pure Pd (blue) and Pd/rGO nanocomposite (red).

XPS was performed to confirm the degree of reduction of the graphene oxide and Pd. The C 1s spectra of GO (Fig. 6.2A) and rGO (Fig. 6.2C) revealed several peaks at 284.03, 284.95, 286.37, 287.41, 288.59, 290.46, 291.59 and 293.08 eV, corresponding to aromatic C-C, sp^2 C, C-OH, C-O, C=O, HO-C=O, C-F_3 and C-F_2 bonds, respectively.[24,25] The C 1s spectrum of GO revealed the presence of a highly oxidized carbon species, and for rGO, the decrease of C-OH, C-O, C=O, HO-C=O binding energies (at 286.37, 287.41, 288.59, 290.46 eV) and an additional peak at 285.6 eV indicated the presence of a non-oxygenated rings of C,[26] revealing that the electrochemical reduction process was effective for the removal of exogenous oxygenated functional groups. High-resolution spectra of 3d regions of Pd prior to and following reduction are shown in Figs. 6.2B and 6.2D, respectively, where doublet peaks were located at a low binding energy ($3d_{3/2}$) and a high binding energy ($3d_{5/2}$). The binding energies were measured at 337.3, 342.6 eV in the case of pure Pd, and at 340.0 and 334.7 eV in the case of the Pd/rGO nanocomposite. The negative shifts of the Pd 3d doublet peaks, in the case of the Pd/rGO nanocomposite, indicated the effective reduction of the metal ions. By fitting the high resolution XPS spectra (Fig. 6.2 D), the oxidation state of the Pd nanoparticles in the Pd/rGO nanocomposites were determined. It is found that 72.8% of Pd in its metallic state and 27.2% of Pd in its higher oxide states. The aforementioned results confirmed that the Pd NPs were trapped within the rGO sheets through stable bonding, which involved complex interactions, rather than simple physical adsorption.

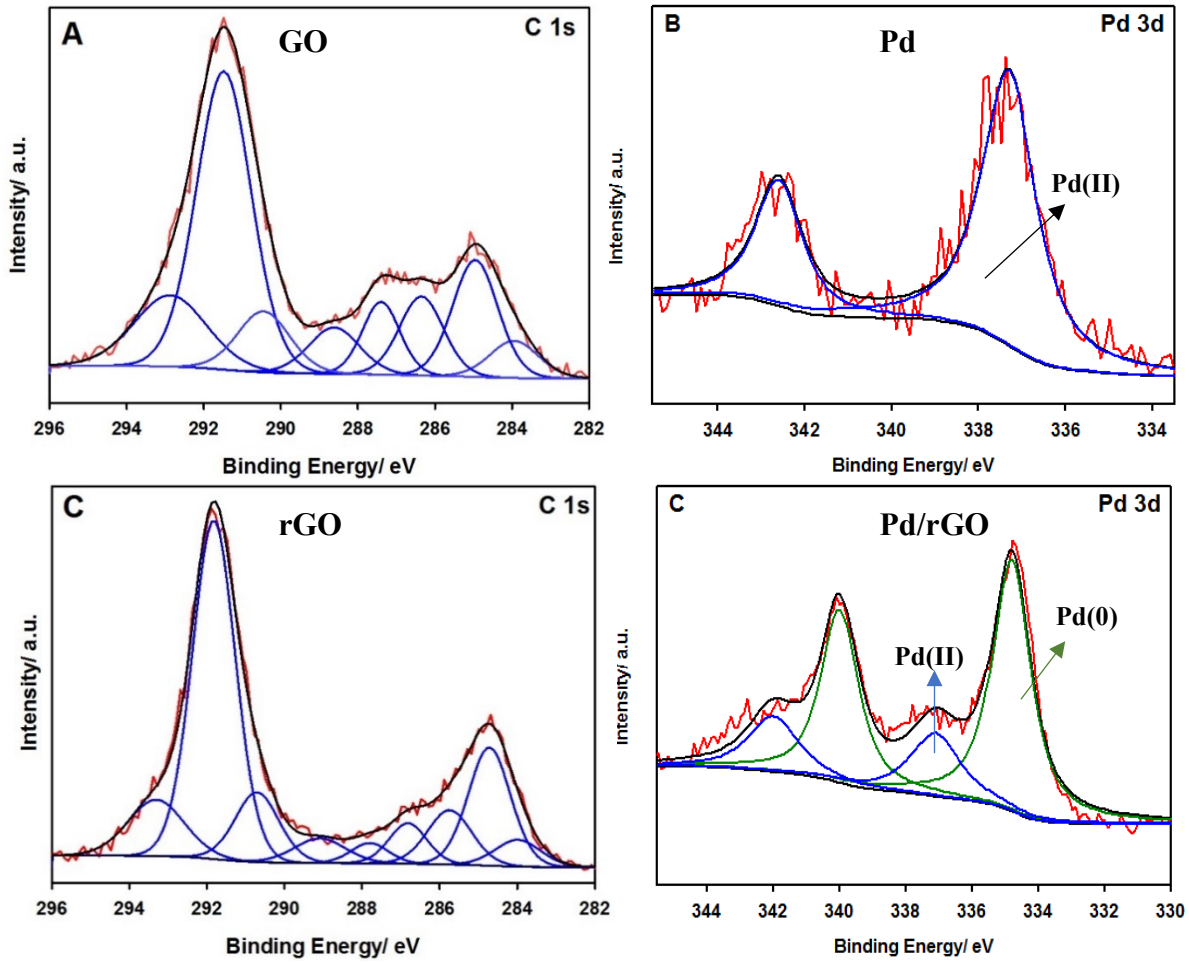

Figure 6.2: XPS spectra of the C 1s region (A and C) and Pd 3d regions of (B and D) of Pd/GO and Pd/rGO nanocomposites.

6.3.2 Electrochemical Studies

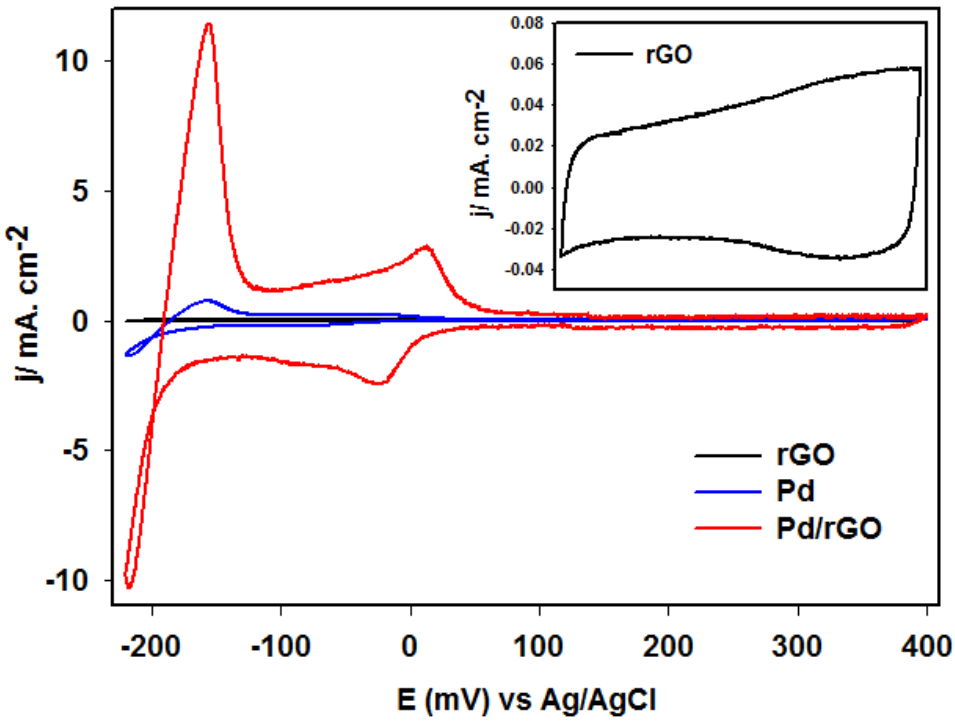

Figure 6.3: CV of rGO (black), pure Pd (blue) and the Pd/rGO nanocomposite (red) on GCE, Inset: CV of rGO.

For the electrochemical characterization of rGO, pure Pd, and the Pd/rGO nanocomposite for hydrogen sorption, two cycles of the CVs were performed in an argon saturated 0.5 M H_2SO_4 solution in the range of from -220 to 400 mV, at a scan rate of 20 mV/s. First cycle is considered to activate or clean the surface of the electrode, so if any impurities present on the surface that can be removed. The second cycle was selected for the comparison of rGO, pure Pd, and the Pd/rGO nanocomposite and presented in Fig. 6.3. The inset illustrates the enlarged CV of rGO. In the case of rGO, no adsorption or desorption peaks were observed, whereas, in the case of pure Pd and Pd NPs dispersed on rGO, there were significant changes in the hydrogen sorption and desorption observed in CVs at below 50 mV.

For the Pd/rGO nanocomposite, the hydrogen adsorption began at 50 mV when scanning the electrode potential from 400 to -220 mV. A large peak due to the desorption of hydrogen appeared at -155 mV, followed by a shoulder in the range from -50 to 50 mV; appeared when the electrode potential was scanned from -220 to 400 mV, which is due to the presence of Pd oxide on the surface. In contrast, hydrogen sorption and desorption were much smaller, with the hydrogen desorption peak at -155 mV, in the case of pure Pd due to larger particle sizes. The integrated hydrogen oxidation charges from the CVs were calculated to be 1017 mC and 203 mC for the Pd/rGO nanocomposite and the pure Pd. This significant improvement may be attributed to the formation of the uniform and small dimensions of the Pd NPs, which were dispersed on the large reduced graphene oxide surface area, which was consistent with the SEM image shown in Fig. 6.1C. Another cause for the significant improvement is due to the spillover effect. Hydrogen spillover is commonly described as the dissociative adsorption of H_2 on metal catalyst particles, followed by the migration of H atoms to the support and diffusion of the atoms on the support.[27] This clearly demonstrated that Pd NPs dispersed on rGO had superior capacity toward hydrogen sorption and storage in contrast to Pd.

In order to determine the time required for steady state hydrogen sorption, chronoamperometry (CA) was performed by holding the electrode potential constant at -220 mV over different time periods (e.g., 0, 1, 3, 5, 7 and 10 min), immediately followed by linear voltammetry (LV), where the electrode potential was scanned from -220 to 400 mV, as shown in Fig. 6.4A. The hydrogen desorption charge Q_H was calculated by integrating the hydrogen desorption current from the LVs of Fig. 6.4B. The Q_H plot versus the holding time is depicted in Fig. 6.3C, revealing a rapid hydrogen uploading process. The hydrogen storage capacity was increased in the following order: 0 (584 mC) < 10 (1011 mC) < 1 (1017 mC) < 7 (1018 mC) < 5 (1025 mC) < 3 (1038 mC).

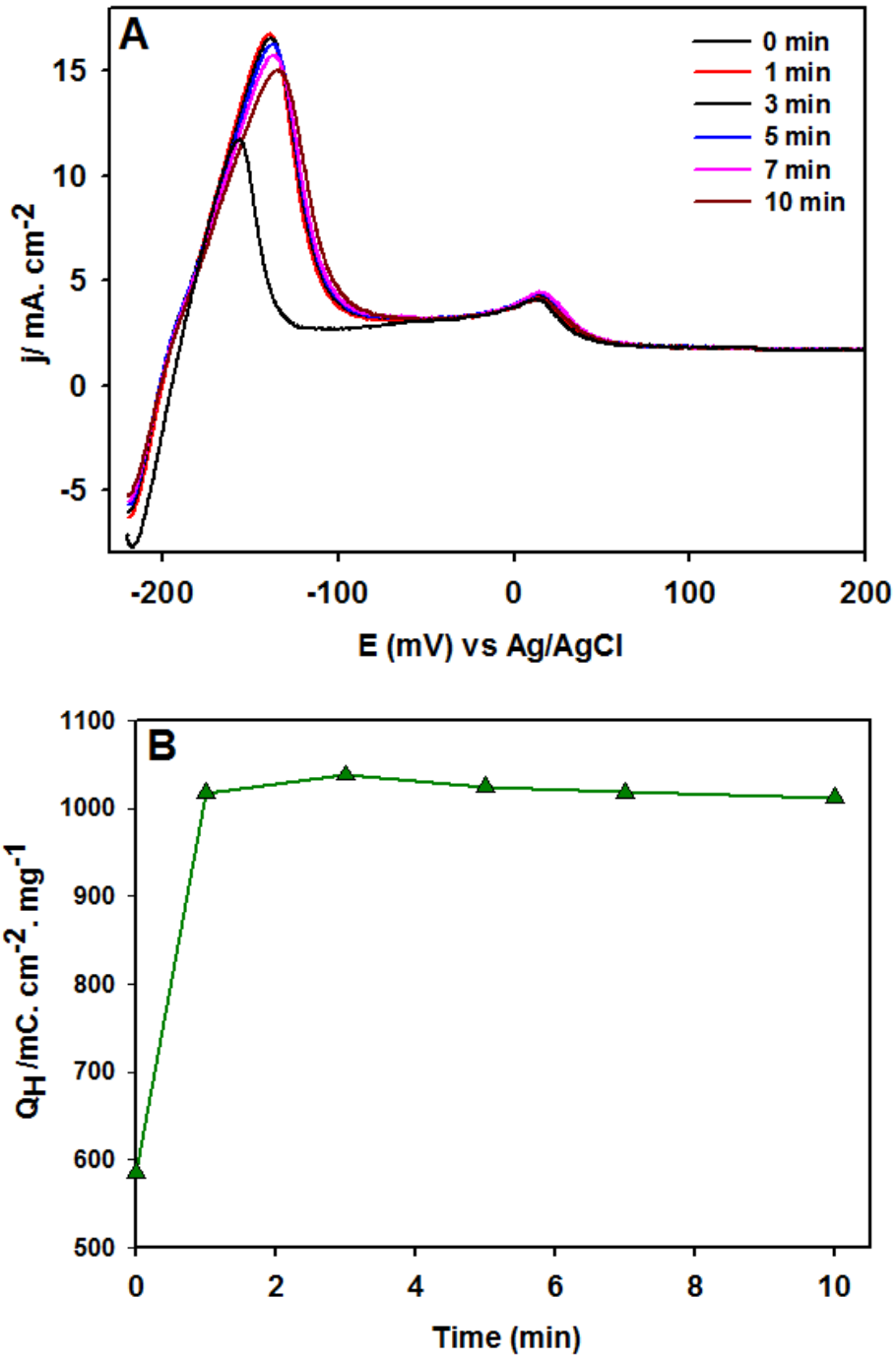

Figure 6.4: (A) Anodic sweeps of the Pd/rGO nanocomposite at -210 mV at different holding times at 20 mVs in 0.5 M H_2SO_4, and (B) Hydrogen desorption charge capacity at different holding times.

To further investigate the kinetics and effect of the held potential on the capacity of hydrogen sorption and storage, the potential was held constantly for 3 min which was sufficient to ensure the complete saturation of hydrogen into the prepared catalyst as seen in Fig. 6.4B, where the held electrode potential was gradually varied from -50 to -210mV. Three minute time holding with respect to Pd/rGO has taken as reference for the pure Pd samples. Fig. 6.5A and 6.5B present a series of LVs of the pure Pd and Pd/rGO nanocomposite, respectively. In case of pure Pd the current for the hydrogen desorption/oxidation peak was slowly increased with a negative shift of the peak potential form -50 to -170 mV, further lowering of the held potential from -170 to -190 mV, the peak current was increased significantly, with a positive shift of the peak potential. When the held potential was lowered from -190 to -210 mV, the peak current was slightly altered with a small positive shift and the hydrogen is not completely desorbed. This is mainly due to the larger particle size of Pd which is consistent with SEM image as shown in Fig. 6.1b the active surface sites available for hydrogen absorption/adsorption were limited which results in much slower sorption kinetics when compared to the nanoparticulate forms. Whereas in case of Pd NPs dispersed on rGO, the current for the hydrogen desorption/oxidation peak was slowly increased with a negative shift of the peak potential form -50 to -190 mV, further lowering of the held potential from -190 to -210 mV, the peak current was increased significantly indicating the fact that under electrochemical conditions, the volume of hydrogen stored within the Pd NPs was potential dependent, where a lower electrode potential, in gas phase experiments, corresponded to a higher hydrogen pressure. In case of both pure Pd and Pd/rGO nanocomposite, there is small peak centered at 0 mV, which is may be due to the presence of palladium oxide.

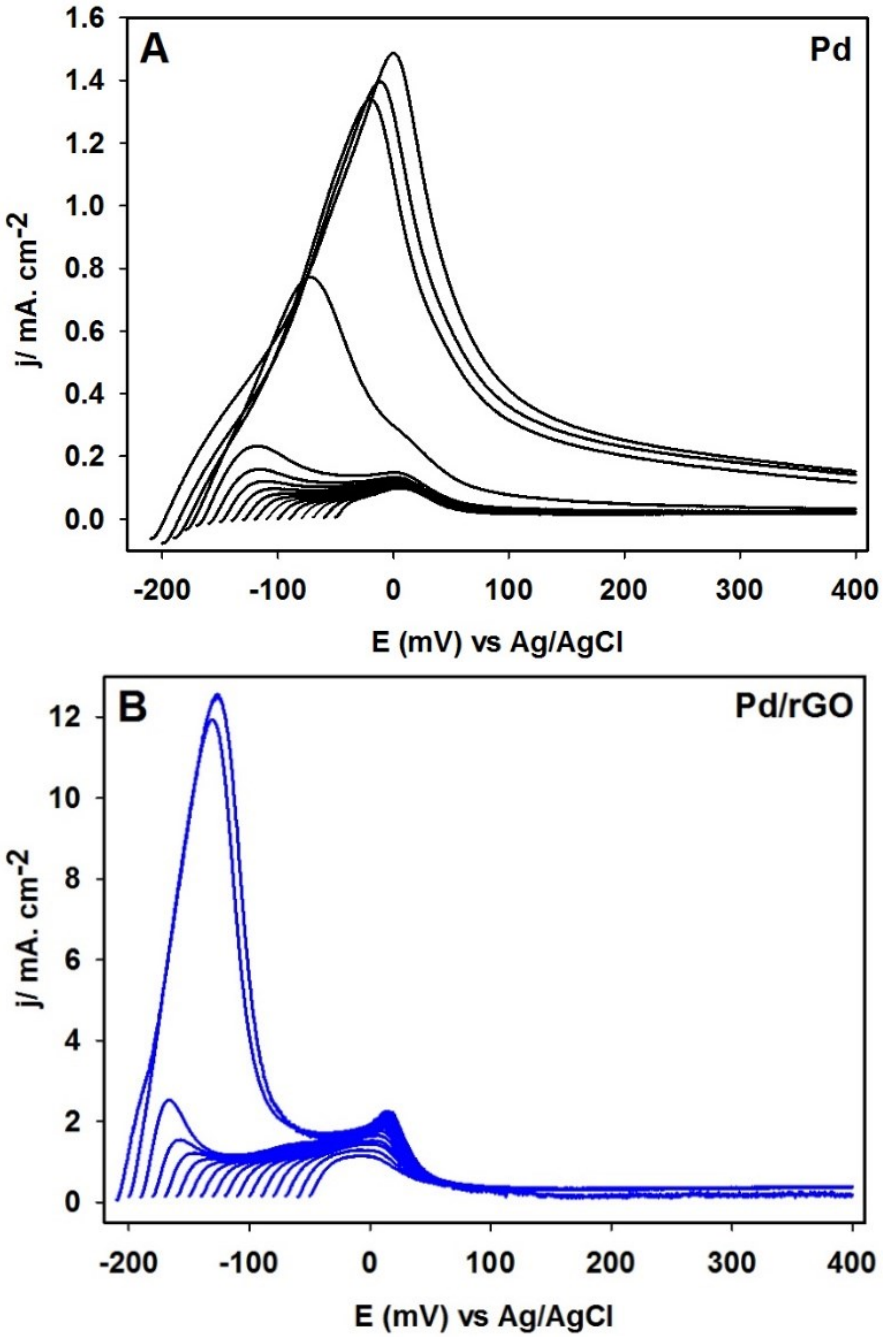

Figure 6.5: Anodic sweeps of the desorption of hydrogen from pure Pd (A) and the Pd/rGO nanocomposite (B) after holding the potential at various cathodic limits for 3 min in 0.5 M H_2SO_4 at a scan rate of 20 mV/s.

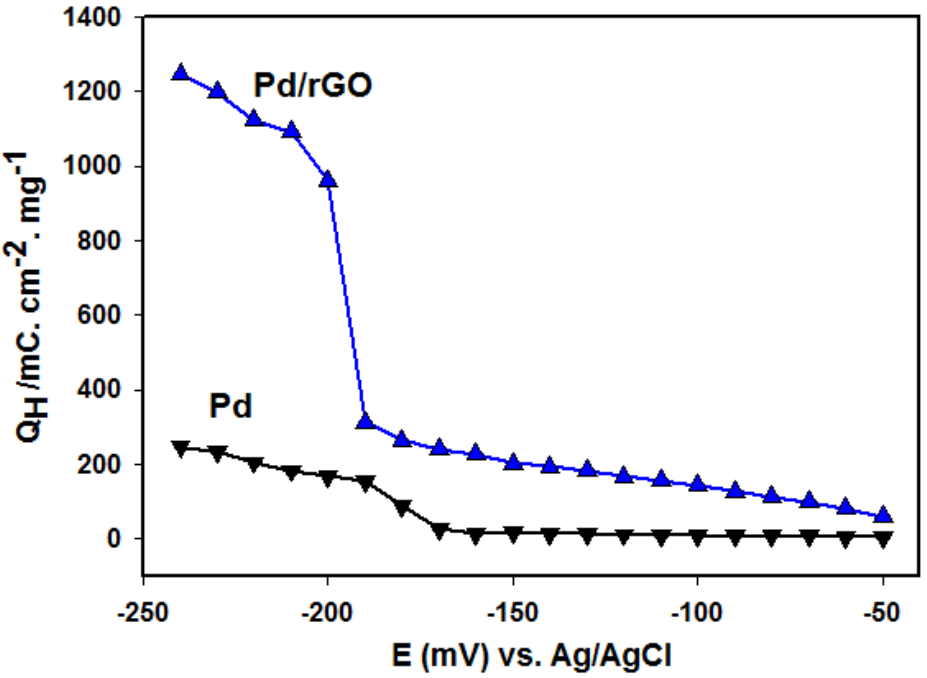

Figure 6.6: The overall hydrogen desorption charge, Q_H, was normalized by the mass of Pd versus the held electrode potentials.

Fig. 6.6 shows the comparison of the overall hydrogen oxidation charges (Q_H) of pure Pd and the Pd/rGO nanocomposite at the variously held electrode potentials. The total hydrogen discharge was calculated by integrating the hydrogen desorption peak shown in Figs. 6.4A and 6.4B. In the case of pure Pd and the Pd/rGO nanocomposite, Q_H was slightly increased, from -50 to -190 mV. A significant increase in Q_H was observed when the held potential was decreased from -190 to -200 mV, due to the phase transition. In the case of Pd, the adsorption/absorption of hydrogen may result in two different phases known as α phase and β phase.[28] At low hydrogen concentrations a solid solution is formed that represents the α phase, whereas at higher concentrations, a metal hydride is formed, which represents the β phase. In the case of the Pd/rGO nanocomposite electrode, the potential range from -50 to -190 mV represented α and the potential below -200 mV

corresponded to the β phase hydrogen sorption. The average of the Q_H ratios of the Pd/rGO nanocomposite to the Pd nanoparticles were calculated, showing an increase of 11.73 times in the α phase region and 5.43 times enhancement in the β phase region. Pure Pd exhibits the highest maximum value of H/Pd ratio of ∼0.27 at the potential of -240 mV. The maximum H/Pd ratio is seen at -240 mV for Pd/rGO nanocomposite is ∼1.32. At potentials more negative than this, a substantial amount of hydrogen evolution was observed, and this caused cracking and loss of the nanostructured coatings to the electrolyte solution.

6.4. Conclusion

In summary, a new Pd/rGO nanocomposite was synthesized via a simple one-step electrochemical reduction approach, which facilitates the formation of highly dense and uniform Pd nanoparticles and rGO nanocomposite in the absence of any capping agents, organic solvents and reducing chemicals. The synthesised Pd/rGO nanocomposite demonstrated significantly enhanced capacity for hydrogen sorption and storage in contrast to pure Pd nanoparticles. The approach described in this study may be applied to fabricate various metallic nanoparticles and rGO nanocomposites for further improvement of hydrogen sorption and energy storage capacities.

References

1. L. Schlapbach, A. Zuttel. Hydrogen-storage materials for mobile applications, Nature **2001**, 414 , 353-358.

2. V. B. Parambhath, R. Nagar, S. Ramaprabhu. Effect of nitrogen doping on hydrogen storage capacity of Pd decorated graphene. *Langmuir* **2012**, 28, 7826-7833.

3. A. Züttel. Hydrogen storage methods. *Naturwissenschaften* **2004**, 91, 157-172.

4. M. Lototskyy, V. A. Yartys. Comparative analysis of the efficiencies of hydrogen storage systems utilising solid state H storage materials. *J. Alloys Comp.* **2015**, 645, S365-S373.

5. B. D. Adams, G. Wu, S. Nigro, A. Chen. Facile synthesis of Pd-Cd nanostructures with high capacity for hydrogen storage. *J. Am. Chem. Soc*. **2009**, 131, 6930-6931.

6. X. Zhou, Z. Chen, D. Yan,. H. Lu. Deposition of Fe-Ni NPs on polyethyleneimine-decorated graphene oxide and application in catalytic dehydrogenation of ammonia borane. *J. Mater. Chem.* **2012**, 22, 13506-13516.

7. I. López-Corral, E. Germán, A. Juan, M. A. Volpe, G. P. Brizuela. DFT Study of hydrogen adsorption on Pd decorated graphene. *J. Phys. Chem. C* **2011**, 115, 4315-4323.

8. B. D. Adams, A. Chen. The role of palladium in a hydrogen economy. *Mater Today* **2011**, 14, 282-289.

9. I .Cabria, M. J. López, S Fraile, J. A Alonso. Adsorption and dissociation of molecular hydrogen on Pd clusters supported on graphene. *J. Phys. Chem. C* **2012**, 116, 21179-21189.

10. V. B. Parambhath, R. Nagar, K. Sethupathi, S. Ramaprabhu. Investigation of spillover mechanism in Pd decorated hydrogen exfoliated functionalized graphene. *J. Phys. Chem. C* **2011**, 115, 15679-15685.

11. C.-C. Huang, N.-W. Pu, C.-A. Wang, J.-C. Huang, Y. Sung, M.-D. Ger. Hydrogen storage in graphene decorated with Pd and Pt nano-particles using an electroless deposition technique. *Separation and Purification Technology* **2011**, 82, 210-215.

12. B. D. Adams, C. K. Ostrom, A. Chen. High-Performance Pd-based hydrogen spillover catalyst for hydrogen storage. *J. Phys. Chem. C* **2010**, 114, 19875-19882.

13. V. Sridhar, H.-J. Kim, J.-H. Jung, C. Lee, S. Park, I.-K. Oh. Defect-engineered three-dimensional graphene–nanotube–Pd nanostructures with ultrahigh capacitance. *ACS Nano* **2012**, 6, 10562-10570.

14. E. P. Randviir, D. A. C. Brownson, C. E. Banks. A decade of graphene research: production, applications and outlook. *Mater Today* **2014**, 17, 426-432.

15. M. Pumera. Electrochemistry of graphene, graphene oxide and other graphenoids: Review. *Electrochem. Commun*. **2013**, 36, 14-18.

16. M. Shi, W.Liu, D. Zhao, Y. Chu, C. Ma. Synthesis of Pd NPs supported on reduced graphene oxide-tungsten carbide composite and the investigation of its performance for electrooxidation of formic acid. *J. Solid State Electrochem.* **2014**, 18, 1923-1932.

17. Y. Jiang, Y. Lu, F. Li, T. Wu, W. Chen. Facile electrochemical codeposition of "clean" graphene-Pd nanocomposite as an anode catalyst for formic acid electrooxidation. *Electrochem. Commun.* **2012**, 19 21-24.

18. D. R. Dreyer, S. Park, C. W. Bielawski, R. S. Ruoff. The chemistry of graphene oxide. *Chem. Soc. Rev.* **2010**, 39, 228-240.

19. Y. Jiang, Y. Lu, F. Li, T. Wu, L. Niu, W. Chen. Facile electrochemical codeposition of “clean” graphene–Pd nanocomposite as an anode catalyst for formic acid electrooxidation. *Electrochem. Commun.* **2012**, 19, 21-24.

20. M. Pumera. Graphene-based nanomaterials and their electrochemistry. *Chem. Soc. Rev*. **2010**, 31, 4146-4157.

21. H. Ji, M. Li, Y. Wang, F. Gao. Electrodeposition of graphene-supported PdPt nanoparticles with enhanced electrocatalytic activity. *Electrochem. Commun.* **2012***,* 24, 17-20.

22. W. Song, X. Ji, W. Deng, Q. Chen, C. Shen, C.E. Banks, Graphene ultracapacitors: structural impacts. *Phys. Chem. Chem. Phys.* **2013**, 15, 4799-4803

23. E. P. Randviir, C. E. Banks. The oxygen reduction reaction at graphene modified electrodes. *Electroanalysis* **2014**, 26, 76-83.

24. M. Govindhan, A. Chen. Simultaneous synthesis of gold nanoparticle/graphene nanocomposite for enhanced oxygen reduction reaction. *J. Power Sources* **2015,** 274, 928-936.

25. Y. H. Ding, P. Zhang, Q. Zhuo, H. M. Ren, Z. M. Yang, Y. Jiang. A green approach to the synthesis of reduced graphene oxide nanosheets under UV irradiation**.** *Nanotechnology* **2011**, 22, 215601-215606.

26. D. Cai, M. Song. Preparation of fully exfoliated graphite oxide nanoplatelets in organic solvents. *J. Mater. Chem.* **2007**, 17, 3678-3680.

27. S. K. Konda, A. Chen. Palladium based nanomaterials for enhanced hydrogen spillover and storage. *Mater Today* **2015,** 19, 100-108.

28. D. G. Narehood, S. Kishore, H. Goto, J. H. Adair, J. Nelson, H. R. Gutiérrez, P. C. Eklund. X-ray diffraction and H-storage in ultra-small palladium particles. *Int. J. Hydrogen Energy* **2009**, 34, 952-960.

Chapter 7: Photo-assisted Deposition of Palladium Nanoparticles on Carbon Nitride for Efficient Oxygen Reduction

7.1 Introduction

Given the critical degradative environmental impacts of traditional energy sources, there is a great interest to develop clean, cost-effective, and efficient energy technologies. One potential solution toward addressing global energy demands comprises fuel cell technologies. The potential applications of fuel cells are extensive as they have the capacity to provide clean energy and sustainable power.[1] Fuel cells directly utilize fuels (e.g., hydrogen, methanol, formic acid) and oxygen to effectively convert their chemical energy into electricity with a high power density.[2] The difficult challenges associated with fuel cells relate to the development of highly active electrocatalysts to reduce the high overpotential at the cathode during the ORR.[3] The ORR mechanism in alkaline aqueous solution occurs as follows:[11]

$$O_2 + 2H_2O + 4e^- \rightarrow 4OH^- \qquad (7\text{-}1)$$

$$O_2 + H_2O + 2e^- \rightarrow HO_2^- + OH^- \qquad (7\text{-}2)$$

$$HO_2^- + H_2O + 2e^- \rightarrow 3OH^- \qquad (7\text{-}3)$$

ORR in alkaline solution occurs mainly either through the direct pathway which involves the transfer of four electrons to produce hydroxide or the indirect pathway which involves two step two electron transfer which produces intermediate superoxide. In some cases, depending on the catalyst used the formed superoxide is not further reduced to hydroxide and can decrease the catalytic activity. Therefore, the complete reaction with formation of hydroxide with four electron transfer is desirable.

*The results presented in this chapter have been published in *The Journal of Physical Chemistry C,* **2016**. 120, 14467-14473.

Platinum (Pt) is considered as one of the preeminent electrocatalysts for ORR. Unfortunately, the limited availability and expense of Pt are major constraints that limit its wide commercial application.[4] There have been significant advancements made in the elucidation of ORR on Pt-based nanomaterials; however, they still struggle with severe stability and consistency issues, together with crossover and poisoning effects in the cathodic compartments of the direct methanol fuel cell, which result in a decrease in the performance of the catalysts.[5] Therefore, it is necessary to identify alternate new materials and methodologies to overcome costs related issues and to enhance the catalytic performance of electrocatalysts.[6,7]

Graphitic carbon nitride (g-C_3N_4) has a planar structure, similar to graphite.[8] It includes both pyridinic and graphitic nitrogen moieties, where each C atom is connected to three N atoms. Additionally, g-C_3N_4 may be facilely produced at a large scale with low cost. Recent studies have shown that C_3N_4 is an effective photocatalyst with enhanced visible light response.[9,10] In contrast, the activity of C_3N_4 as an electrocatalyst for ORR was observed to be very low due to its poor conductivity. To further enhance the electrocatalytic activity of g-C_3N_4, different carbon-based materials are integrated as a co-support; meanwhile, metal nanomaterials are employed as catalysts to improve charge-transfer as well as the electrochemical behaviour of carbon nitrides.[11,12]

Pd based nanomaterials have gained remarkable attraction in miscellaneous research studies,[13,14] comprising catalysis,[15] and sensors.[16,17] It may serve as an attractive alternative in the development of non-platinum catalysts with catalytic activity similar to Pt.[18] Recent studies have shown that the active sites for ORR strongly depend on the surface structure of Pd. Kondo et al. have shown that the Pd(100) electrode surface exhibited over three times increase in current density in comparison with the Pt(110) surface for ORR.[19] It was reported that in acidic media, pure Pd activity is higher than that of all other noble metals, except Pt; however, the tendency of

Pd dissolution in acidic media decreases the stability of the electrode. On the other hand, it is known that in alkaline solutions Pd exhibits high stability and electrocatalytic activity toward ORR due to a reduced anion poisoning effect.[20] Density functional theory (DFT) calculations based on oxygen adsorption and vacancy formation energies indicated that the use of Pd as a co-catalyst might play an important role in ORR in case of catalytic behaviour as well as long-term stability.[21]

In this study, g-C_3N_4 was fabricated using a facile combustion method, and the synthesized g-C_3N_4 was used as a support for the Pd NPs. For the first time, a photo-assisted deposition approach was used in the fabrication of Pd-g-C_3N_4 at room temperature. The physicochemical characteristics of the g-C_3N_4 and Pd-g-C_3N_4 electrodes were evaluated by SEM, TEM, EDX, XRD, XPS, and various other characterization techniques. Our experimental results have shown that the Pd-g-C_3N_4 nanocomposite exhibited significantly improved electrocatalytic behaviour for the ORR in 0.1 M KOH solution. The prepared catalyst also demonstrated enhanced tolerance against methanol and a significant improvement in terms of stability in comparison to the state-of-the-art Pt/C catalyst.

In this chapter, Mona Amiri assisted with the XRD (Fig 7.3 A) and also helped in calculating the electron transfer number using KL plots. Jiali Wen performed BET analysis (Fig. 7.3 B). She analysed pore size, micropore volume and mesopore volume using QSDFT, DA and BJH methods. Rest of the material characterisation, analysis and electrochemical studies were performed by me.

7.2 Experimental

7.2.1 Synthesis of g-C_3N_4 and Pd-g-C_3N_4

Urea (99.99%) was used to synthesize the g-C_3N_4 nanomaterials. In a classic reaction, 15.0 g urea was added to 20.0 ml of pure water produced by a NANOpure® system. The solution was allowed to stir for 30 min until all of the urea was dissolved, and then heated to 400 °C. The solid products

obtained were heated further at 450 °C in a closed atmospheric chamber oven for 3 h.[22] The Pd NPs were directly deposited onto g-C_3N_4 using a facile photo-assisted reduction process. To deposit Pd NPs onto the g-C_3N_4, 10.0 mM $Pd(NO_3)_2$ and 1.0 mg of synthesized g-C_3N_4 were added in 5 mL of ultrapure water and allowed to sonicate for 15 min. Subsequently, 5 mL of 50% (v/v) methanol was added to the above mixture, then it was deaerated for 20 min with ultrapure argon gas prior to UV exposure. The solution was then treated by UV-Visible light for 60 min and lastly rinsed with NANOpure water several times and centrifuged and dried in a vacuum oven at 40 °C overnight. The mass of the Pd NPs loaded onto the carbon nitride was indirectly estimated by inductively coupled plasma atomic emission spectroscopy (ICP-AES) and further confirmed by thermo gravimetric analysis (TGA).

7.2.2 Material Characterization

The surface structure and composition of the prepared catalysts were analysed using JEOL 5900LV SEM and JEOL 2010 TEM. The EDX spectra and elemental mapping of the prepared catalyst were obtained using a Hitachi Su-70 Schotty. The XRD patterns were measured on a PW1050-3710 diffractometer with a Cu Kα (λ = 1.5405 Å) radiation source. XPS was performed with a Thermo Scientific K-α XPS spectrometer. All prepared catalysts were run at a takeoff angle of 90°. A monochromatic Al Kα X-ray source was employed, with a spot size of 400 μm. Charge compensation was measured, and the location of the energy scale was adjusted to place the main C 1s feature (C−C) at 284.6 eV. All data analysis was carried out using XPS peak software. TGA was performed (SDTQ600) in a dried air atmosphere with a ramp rate of 10 °C per minute. FTIR measurements were performed using a Bruker TENSOR27 FTIR spectrometer (Bruker Optics, Germany) with a DTGS detector and a KBr beam splitter in the range from 400 to 4000 cm^{-1} at a resolution of 4 cm^{-1}. The N_2 gas sorption analysis were performed with a Quantachrome Nova

2200 surface area and pore size instrument. All of the catalysts were primarily degassed at 250 °C for 3 h under vacuum. ICP-AES was used to estimate the amount of Pd^{2+} in the solutions before and after photochemical reduction experiment.

7.2.3 Preparation of Electrodes

The working electrodes employed in the present study were rotating disc glassy carbon electrodes (RDGCEs) (0.1964 cm^2 surface area), which were modified with synthesized g-C_3N_4, the Pd-g-C_3N_4 nanocomposite or the commercial Pd/C (wt.10%) purchased from Sigma-Aldrich for comparison. Before coating, the RDGCE surface was polished to a high shine using a fine aluminium powder. For electrochemical studies, the nanocomposites were prepared by dispersing 1.0 mg in 1.0 mL of ultrapure water, then subjected to sonication for 10 min to attain a uniform distribution. Further 10 µL Nafion was added and sonicated for 20 min. A total of 20 µL of prepared solution was dropped on to the RDGCE surface and dried overnight.

7.2.4 Electrochemical Characterization

The electrocatalytic behaviour and electrochemical performance of all the catalysts were investigated by a VoltaLab Potentiostat PGZ301. A three-electrode cell system was employed in all experiments. The counter electrode was a polycrystalline Pt wire, which was flame annealed before the experiments. The reference electrode utilized was a silver/silver chloride (Ag/AgCl). Nernst equation was employed to convert the measured potentials vs. Ag/AgCl ($E_{Ag/AgCl}$) to the reversible hydrogen electrode (RHE) scale (E_{RHE}):[42]

$$E_{RHE} = E_{Ag/AgCl} + 0.059\ pH + E^{o}_{Ag/AgCl} \qquad (7\text{-}4)$$

Where $E^{o}_{Ag/AgCl} = 0.1976$ at 25°C. All the electrochemical analysis were performed in 0.1 M KOH (pH=13) at room temperature, therefore, $E_{RHE} = E_{Ag/AgCl} + 0.964$. The modified RDGCEs were

used as the working electrodes. The electrolyte solutions were deaerated with ultrapure argon (Ar) gas into the electrolyte before the electrochemical characterisation.

Subsequently, 99.99% pure oxygen was purged into the electrolyte for 30 min before the electrochemical measurements, and O_2 was purged over the solution during the electrochemical studies. The electrochemical techniques employed in this study included cyclic voltammetry (CV), linear sweep voltammetry (LSV) and chronoamperometry (CA). The LSV and CA techniques were performed using rotating disk electrodes (RDEs) at different RPM in an O_2-saturated 0.1 M KOH solution at room temperature. The ORR stability tests were performed by initially holding the potential at 960 mV for 20 s, with subsequent stepping to 610 mV for 12.5 h at 1600 rpm.

The number of electrons that were involved in the ORR at various applied electrode potentials was calculated by means of the Koutecky-Levich (K-L) equation[23]:

$$\frac{1}{J} = \frac{1}{J_L} + \frac{1}{J_K} = \frac{1}{B\omega^{1/2}} + \frac{1}{J_K} \quad (7\text{-}5)$$

$$\mathrm{B} = 0.62nFC_0(D_0)^{2/3}v^{-1/6} \quad (7\text{-}6)$$

$$J^{-1} = a + h\omega^{-1/2} \quad (7\text{-}7)$$

where J corresponds to the experimental current density; J_L is the diffusion limiting current density; J_K is the kinetic current density; ω is the electrode rotating speed in rad s^{-1}; n is the overall electron transfer number in ORR; F is the Faraday constant (F = 96485 C mol^{-1}); C_0 is the bulk concentration of O_2 (C_0 = 1.2 x 10^{-3} mol L^{-1}); D_0 is the diffusion coefficient (D_0 = 1.9 x 10^{-5} cm^2 s^{-1}); and v is the kinetic viscosity of the solution (v = 0.01 cm^2 s^{-1}). A plot of J^{-1} versus $\omega^{-1/2}$ is commonly referred to as the Koutecky-Levich plot. From this y-intercept yields the kinetic current density (J_k) and the overall number of electrons passed can be extracted from slope.

7.3 Results and Discussion

7.3.1 Surface Morphology

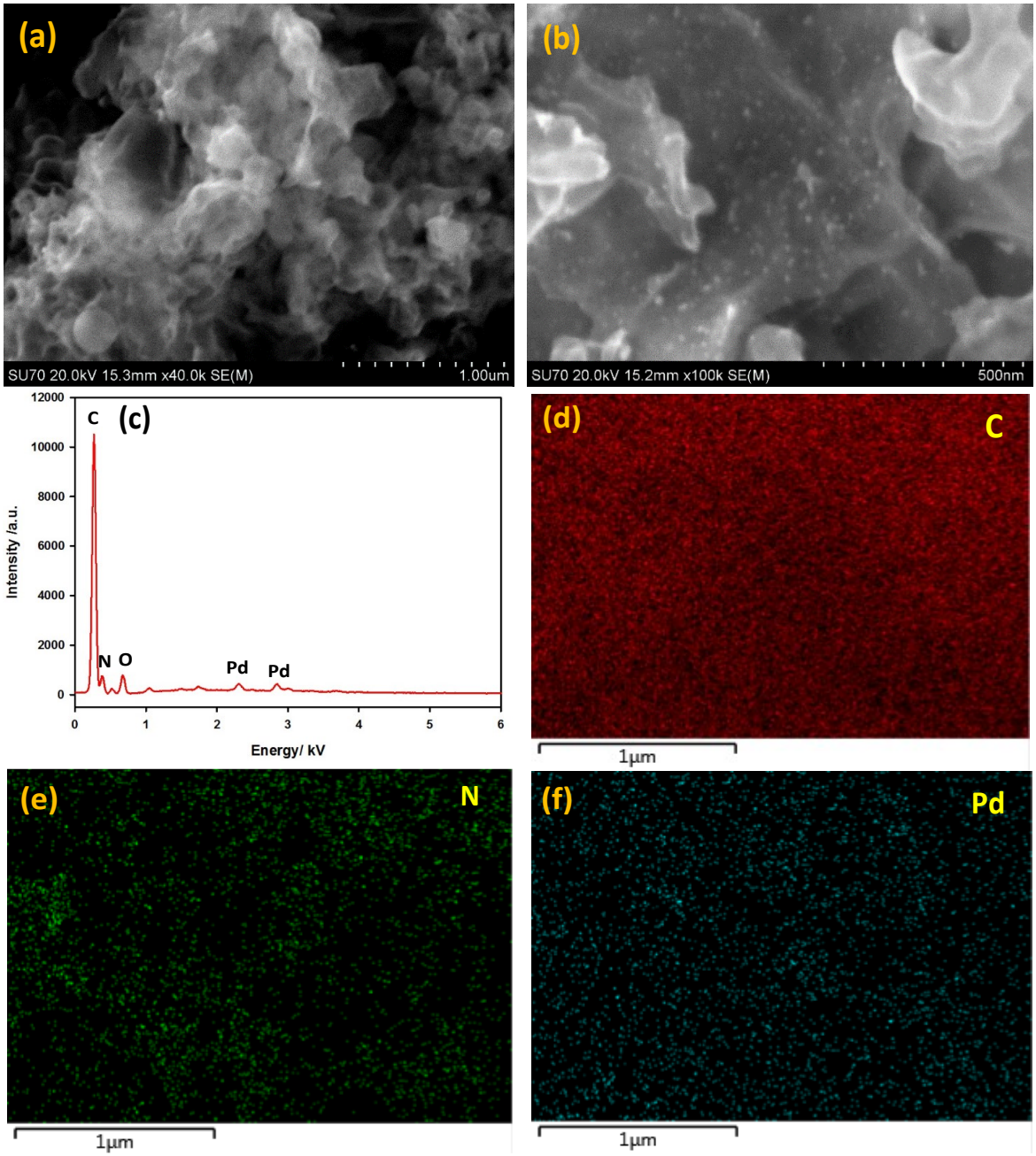

Figure 7.1: SEM images of g-C_3N_4 (a) and Pd-g-C_3N_4 (b) nanocomposite. EDX spectra (c) and elemental mapping distribution images of Carbon (d), Nitrogen (e), and Pd (f) content for the Pd-g-C_3N_4 sample.

The surface morphologies of the synthesized g-C_3N_4 and Pd-g-C_3N_4 nanocomposite were characterized using SEM. Fig. 7.1 depicts the typical SEM image of the g-C_3N_4 (Fig. 7.1a) and Pd-g-C_3N_4 (Fig. 7.1b) nanocomposite. Fig. 7.1a reveals that the synthesized g-C_3N_4 possessed a pore structure and a high surface area. The Pd nanoparticles were well dispersed with an average size distribution from 6 to 10 nm in diameter, as shown in Fig. 7.1b. EDX spectra confirmed the presence of carbon (C), nitrogen (N), and Pd in the Pd-g-C_3N_4 nanocomposite (Fig. 7.1c). A further investigation of the fabricated Pd-g-C_3N_4 nanocomposite distribution, EDX elemental mapping provided a meaningful depiction of the dispersion of elements that comprised the surface containing the C, N, and Pd (Figs. 7.1d, 7.1e, and 7.1f) of the Pd-g-C_3N_4 nanocomposite.

Fig. 7.2a depicts the TEM image of g-C_3N_4, revealing the nanoporous structure and the origin of the large surface area. The TEM image of the Pd-g-C_3N_4 nanocomposite (Fig. 7.2b) indicates a uniform distribution of Pd nanoparticles with the size of 6±0.7 nm. Fig. 7.2c presents a high-resolution TEM image of Pd nanoparticles dispersed on g-C_3N_4; the *d (lattice spacing distance),* among the adjoining planes of the lattice in case of Pd nanoparticles was estimated to be 0.226 nm, attributed to the Pd (111) plane.[15]

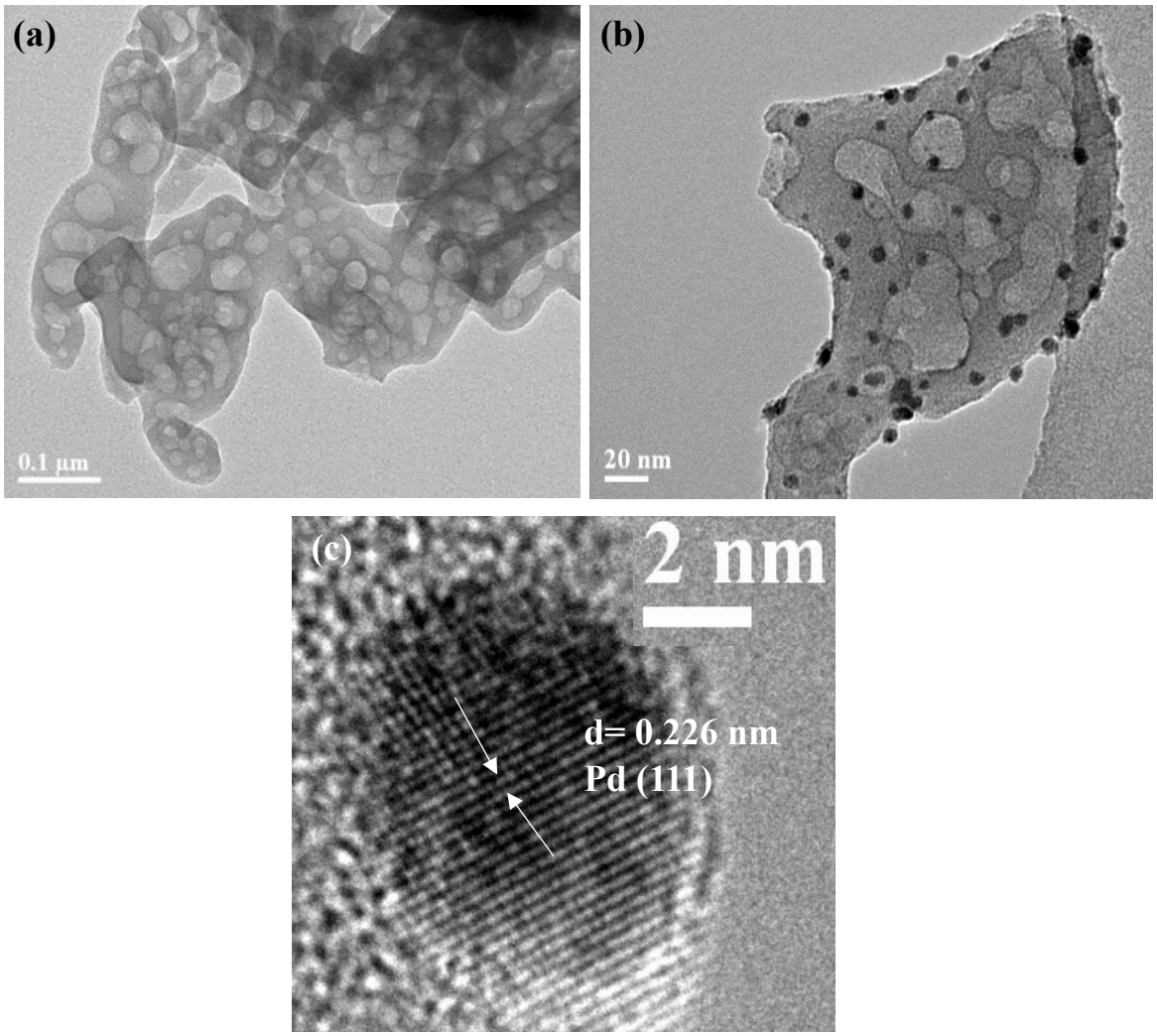

Figure 7.2: TEM images of g-C_3N_4 (a) and Pd-g-C_3N_4 (b); and HRTEM image of the Pd-g-C_3N_4 nanocomposite (c).

7.3.2 Structural Characterisation

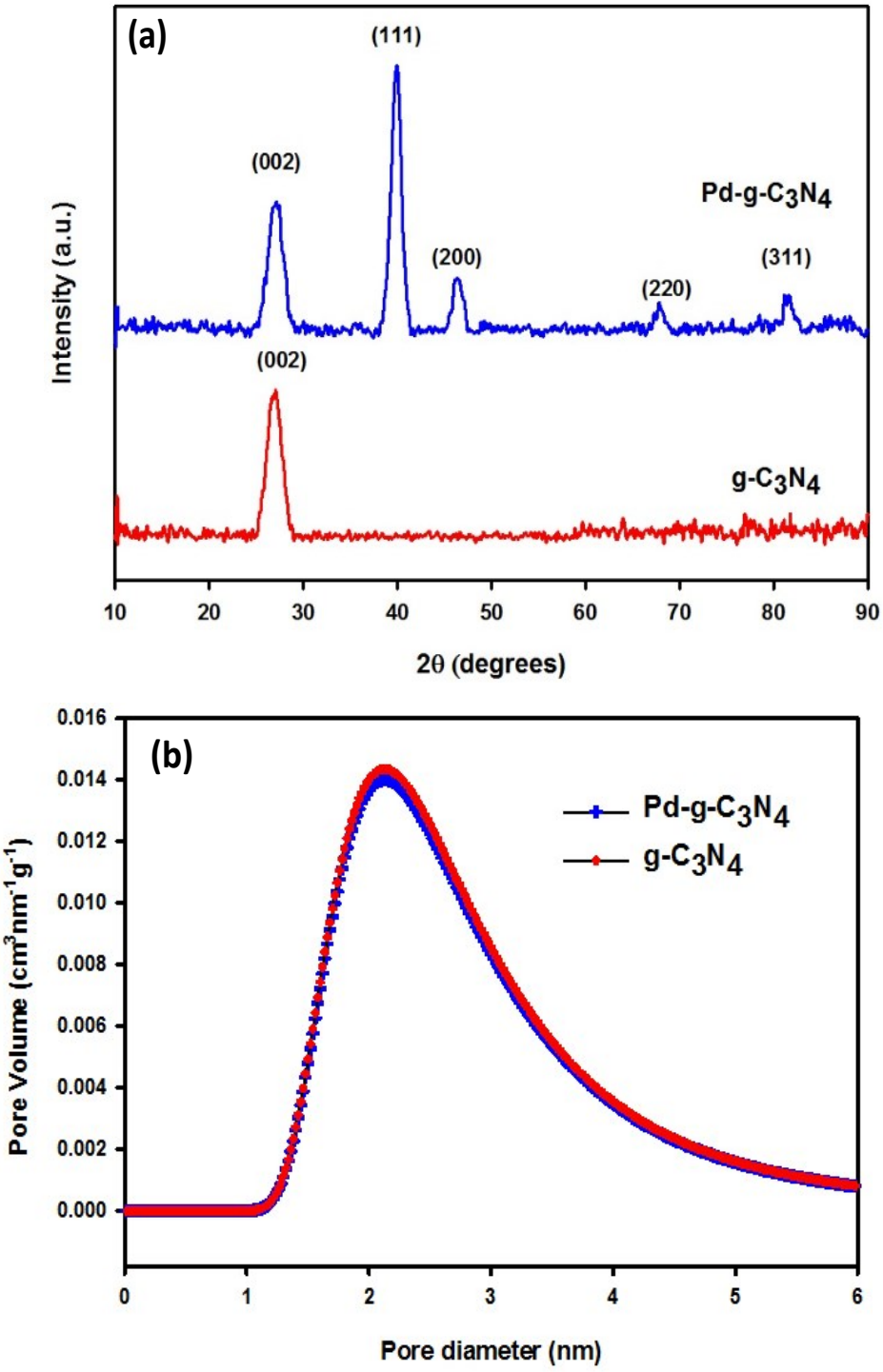

Figure 7.3: XRD patterns (a) and the micropore volumes were measured using the Dubinin−Astakhov method (b) of samples g-C_3N_4 and Pd-g-C_3N_4 nanocomposite.

Fig. 7.3a displays the XRD peaks of the g-C_3N_4 and Pd-g-C_3N_4 nanocomposite. The strong diffraction peak appearing at 27.08° can be attributed to the typical interlayer-stacking phase (002) of g-C_3N_4, revealing the characteristic graphitic structure. The intensity of (002) interlayer-stacking peak represents the extent of graphitization, showing that the g-C_3N_4 synthesized in this study exhibited a higher graphitic features than the typical polymer-based carbon.[24,25] In the case of the Pd-g-C_3N_4 nanocomposite, four additional peaks centered at 39.92°, 46.43°, 67.76°, and 81.68° are the characteristics of face centered cubic (fcc) Pd lattices, which correspond to the (111), (200), (220), and (311) facets, respectively, further confirming the formation of the crystalline Pd nanoparticles within these composites.

The Brunauer−Emmett−Teller (BET) surface areas and pore size of the synthesised g-C_3N_4 and Pd-g-C_3N_4 nanocomposite were examined via N_2 adsorption and desorption at 77 K. The BET surface area was found to be 34.0 and 33.0 $m^2\ g^{-1}$ for the g-C_3N_4 and Pd-g-C_3N_4 nanocomposite, respectively. The isotherm was further fitted using the quenched-solid density functional theory (QSDFT). QSDFT method was generally used for the pore size analysis of geometrically and chemically disordered micro-mesoporous carbons. As shown in Fig. 7.3b, the pore size distribution of the g-C_3N_4 and Pd-g-C_3N_4 nanocomposite was very similar as expected. The total pore volume was calculated to be 0.048 and 0.053 $cm^3\ g^{-1}$, and the micropore volume obtained using the Dubinin−Astakhov (DA) method was 0.029 and 0.028 $cm^3\ g^{-1}$ for the g-C_3N_4 and Pd-g-C_3N_4 nanocomposite, respectively. Further, the Barrett−Joyner−Halenda (BJH) analysis was employed to estimate the volume of mesopore, which were found to be 0.040 and 0.051 $cm^3\ g^{-1}$ for the g-C_3N_4 and Pd-g-C_3N_4 nanocomposite, respectively. The modal micropore diameter was estimated using the DA method to be 2.12 nm for both samples. The micropore and mesopore intensities showed analogous trends with respect to peak intensity for the fabricated g-C_3N_4 and Pd-g-C_3N_4

nanocomposite. All the aforementioned results show that the synthesized g-C_3N_4 and Pd-g-C_3N_4 nanocomposite exhibited large surface areas along with microporous and mesoporous morphology.

The FTIR spectra of the g-C_3N_4 and Pd-g-C_3N_4 nanocomposites were recorded and are displayed in Fig. 7.4a. The IR peaks observed for g-C_3N_4 are consistent with the previous results.[22] The absorption band at 1611 cm^{-1} could be attributed to the C-N stretching vibration modes, the peaks observed at wavenumbers 1253, 1321, 1413, and 1561 cm^{-1} may be attributed to the typical stretching modes of CN heterocycle in g-C_3N_4. The peak at wavenumber 807 cm^{-1} correspond to the skeletal bending modes of the triazine cycle.[22,26]

It was evidently visible that all of the primary distinguishing peaks of g-C_3N_4 appeared in the Pd-g-C_3N_4 nanocomposite, indicating that the modification with Pd NPs did not cause any notable structural change of the g-C_3N_4 substrate. Thermogravimetric technique was used to determine the Pd loading into g-C_3N_4. This was further investigated by ICP-AES technique. The solutions comprising the metal precursor were tested for Pd metal content before and after the synthesis of the Pd-g-C_3N_4 nanocomposite. In the solution less than 0.2 ppm of the metal ions were present, revealing that the Pd precursor was completely reduced by the photochemical reduction approach. Through the subtraction of the final metal ion value from the initial concentration of precursor value, it was observed that the bulk amount of the used catalysts was nearly equal to the input precursor value, indicating that the simple photo-assisted chemical reduction approach employed in this work can precisely control the compositions of the fabricated Pd-g-C_3N_4 nanocomposite.

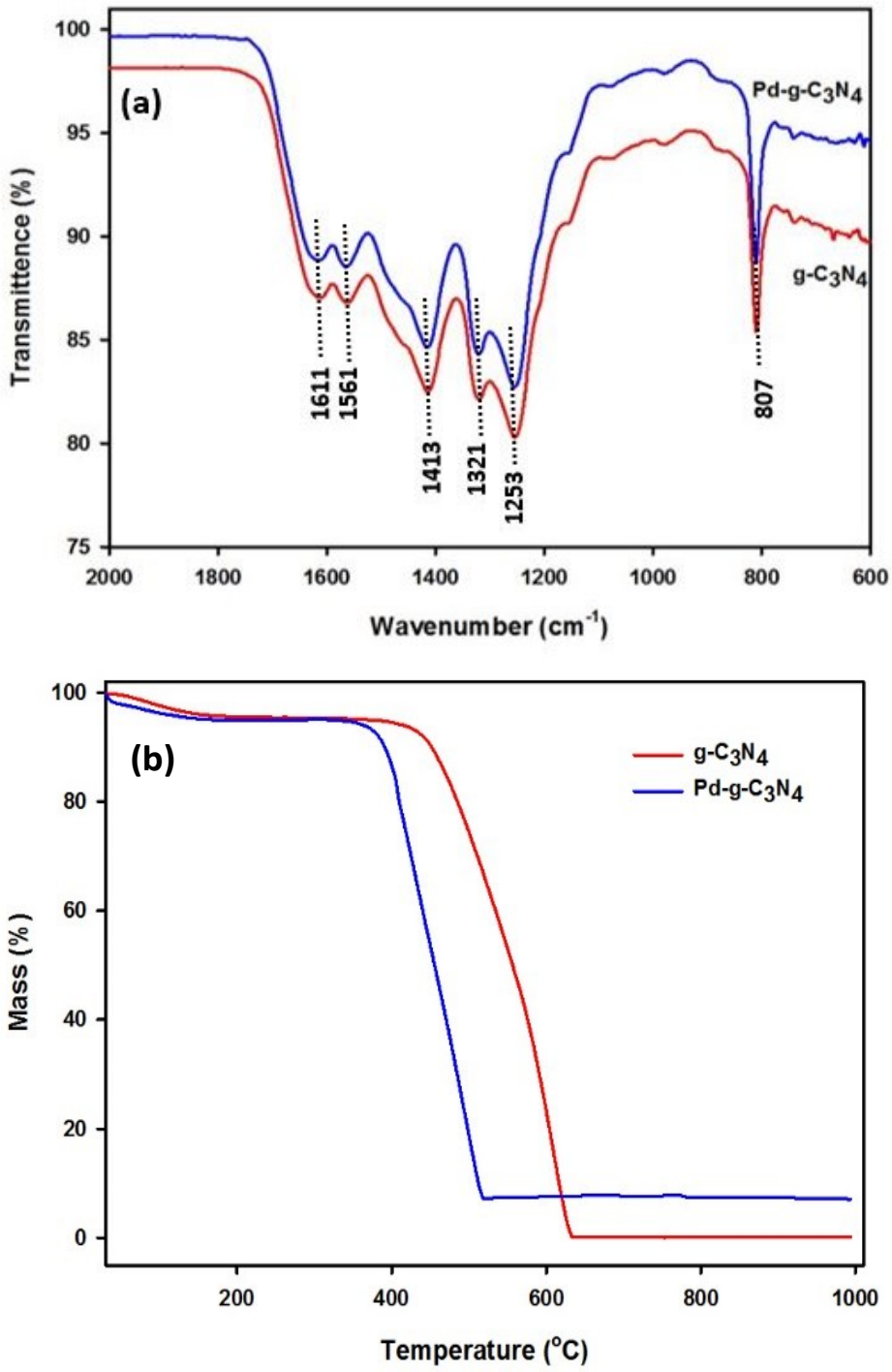

Figure 7.4: FTIR spectra (a) and TGA curves (b) of the g-C_3N_4 and Pd-g-C_3N_4 nanocomposite samples.

To investigate the chemical nature of the synthesised electrocatalysts, XPS technique was performed, with the results shown in Fig. 7.5. The elemental survey scans of the g-C_3N_4 and Pd-g-C_3N_4 nanocomposite samples are displayed in Fig. 7.5a, revealing strong C and N peaks for both samples as well as the additional Pd peaks for the Pd-g-C_3N_4 nanocomposite. The presence of the small oxygen 1s peak at ~531 eV might be due to the adsorption of water or gases like O_2 and CO_2 during preparation of samples. The high-resolution C 1s spectrum presented in Fig. 7.5b reveals three deconvoluted peaks at 288.53, 286.68, and 285.14 eV. The major C peak at 288.53 eV could be correspond to sp^2-bonded C (N–C=N), while the low intense peak at 285.14 eV related to graphitic carbon, which is typically observed during the XPS analysis of carbon nitride.[27,28]

Two distinguished peaks appeared in the high-resolution N 1s spectrum (Fig. 7.5c). The stronger one at 399.03 eV could be assigned to the tertiary N, bonded to C atoms in the form of $N–(C)_3$ or $H–N–(C)_2$;[27,29,30] whereas the peak with a low intensity centred at 400.80 eV might be attributed to protonated pyridine or graphitic nitrogen.[31] The high-resolution scan of Pd 3d region is displayed in Fig. 7.5d, indicating $3d_{3/2}$ peaks at the lower binding energy and $3d_{5/2}$ at the higher binding energy,[32] confirming the presence of Pd nanoparticles.

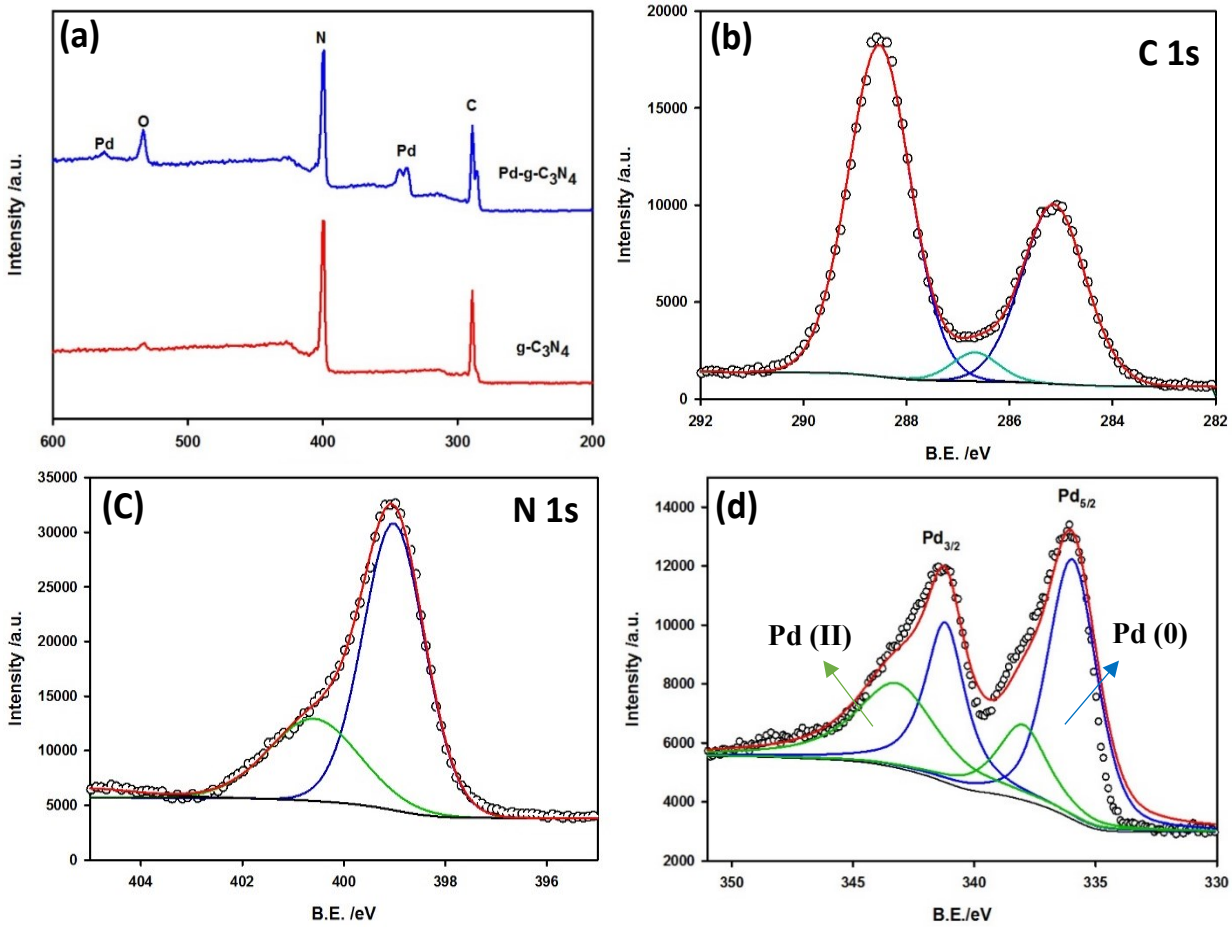

Figure 7.5: (a) XPS survey scans of the two samples; (b) high resolution scan of C 1s region; (c) high resolution scan of N 1s region; and (d) high resolution scan of Pd 3d region of the Pd-g-C_3N_4 nanocomposite. For the high resolution spectra, circles represent raw data, whereas solid dashed black lines, and blue, green, red lines represent baseline, individual components (zero and higher oxidation states), and total fit, respectively.

7.3.3 Electrochemical Activity

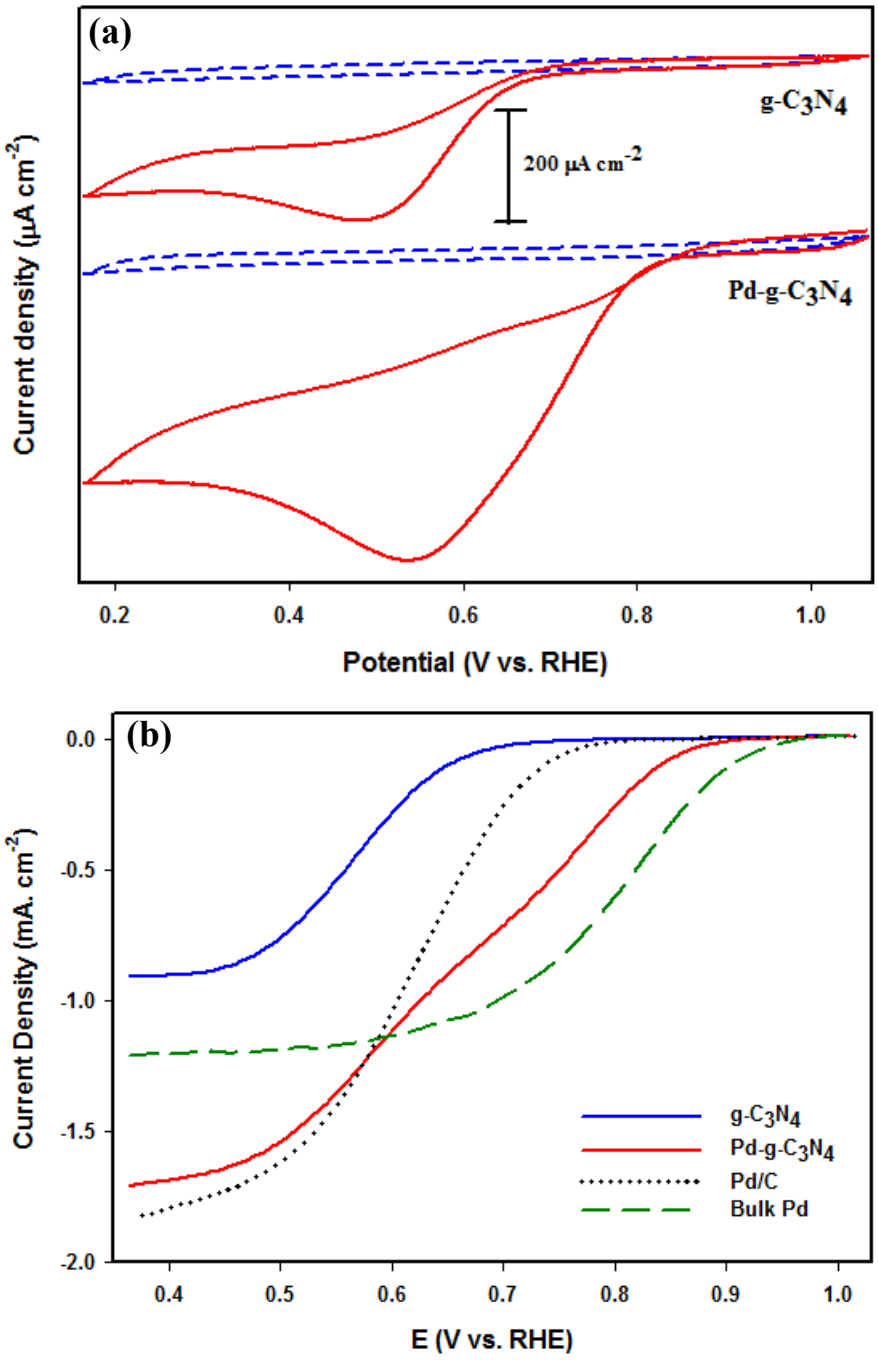

Figure 7.6: CVs of g-C_3N_4 and Pd-g-C_3N_4 (a) in argon (blue curve) and oxygen saturated (red curve) and LSVs of g-C_3N_4 and Pd-g-C_3N_4 at 1600 rpm (b) in 0.1 M KOH solutions. Scan rate: 50 mV/s.

Electrocatalytic activities towards ORR of g-C_3N_4 and Pd-g-C_3N_4 nanocomposite were studied via CV in Ar (dashed line) and O_2-saturated (solid line) 0.1 M KOH solutions measured in the range of 0.16 and 1.06 V vs. RHE at 50 mV/s, which are present in Fig. 7.6a. Featureless curves were seen in the Ar saturated solution for both the g-C_3N_4 and Pd-g-C_3N_4 modified electrodes; whereas well-defined ORR peaks were observed in case of g-C_3N_4 and Pd-g-C_3N_4 nanocomposite electrodes in the O_2-saturated solution. For g-C_3N_4, the onset electrode potential for the ORR was observed at 0.72 V vs. RHE, while the reduction peak appeared at 0.48 V. In contrast, upon the deposition of Pd nanoparticles on the g-C_3N_4, not only the onset potential and the reduction peak of the ORR were positively shifted to 0.90 and 0.54 V, respectively, but also the peak current density were increased over two times. The aforementioned results showed a substantial improvement in the ORR electrocatalytic behaviour for the Pd-g-C_3N_4 nanocomposite in comparison to g-C_3N_4.

To investigate the kinetics involved in the ORR, LSV experiments were conducted further on a RDE in the O_2-saturated 0.1 M KOH electrolyte at 50 mV/s under a rotation rate of 1600 rpm. As shown in Fig. 7.6b, ORR at the metal-free g-C_3N_4 electrode commenced 0.72 V. In contrast, the ORR onset potential at the Pd-g-C_3N_4 electrode was positively shifted to 0.90 V; and the limiting diffusion current was almost doubled. Although the Pd-g-C_3N_4 nanocomposite and the commercial Pd/C exhibited comparable ORR current density at 0.40 V, the onset ORR potential at Pd-g-C_3N_4 (0.90 V) was more positive than that at the Pd/C catalyst (0.81 V). For comparison, the LSV of a commercially available Pd thin foil was recorded under the same experimental condition and also presented in Fig. 7.6b, indicating the ORR onset potential at the bulk Pd (~0.95 V), which was more positive than that at the Pd/C catalyst, in line with the previous study.[33] However, the higher current observed at the Pd foil in the potential ranged from 0.6 to 0.95 V in

comparison with the Pd/C and Pd-g-C_3N_4 may be attributed to the larger electrochemical active surface area. In order to confirm this, CO-stripping experiments were performed in 0.1 M $HClO_4$, revealing that the CO-stripping charge at the Pd foil was 0.856 mC, which was 12 times larger than that at the Pd/C (0.0712 mC). The onset potential of a number of promising electrocatalysts for ORR recently published is listed in Table 7.1, showing that the Pd-g-C_3N_4 nanocomposite synthesized in the present study possessed high catalytic activity, better than Pd/C and the-state-of-art benchmark Pt/C.

Table 7.1. List of the onset potential values of various oxygen reduction reaction catalysts.

Catalysts	**Electrolytes**	**ORR onset potentials/V (RHE)**	**References**
Co-N-CNTs	0.1 M KOH	0.83	[23]
Pt/C (Commercial)	0.1 M KOH	0.85	[23]
Graphene	0.1 M KOH	0.81	[1]
Au/Graphene	0.1 M KOH	0.71	[34]
g-C_3N_4	0.1 M KOH	0.74	[35]
g-C_3N_4/rGO	0.1 M KOH	0.84	[35]
Fe_3O_4/N-Gas	0.1 M KOH	0.77	[36]
$MnFe_2O_4$	0.1M KOH	0.78	[37]
Ag/MWCNT	0.1M KOH	0.80	[38]
rGO/PtRu	0.1 M KOH	0.58	[7]
Au@Pd	1 M KOH	0.80	[39]
Pd/C	0.1M KOH	0.72	[39]
Pd Thin Foil	0.1M KOH	0.95	Present work
Pd-g-C_3N_4	0.1M KOH	0.90±0.01	Present work

The significant enhancement in the ORR could be ascribed to the synergistic charge-transfer effect among the Pd and g-C_3N_4 as well as the structure effect. The pore structure of g-C_3N_4 could play an important role through facilitating O_2 diffusion at the electrode and electrolyte interface. The uniform distribution and smaller size of the Pd nanoparticles directly deposited onto the g-C_3N_4 could also contribute to the high electrocatalytic activity of the Pd-g-C_3N_4 nanocomposite.

To estimate the electron transfer number (n) of the ORR at the g-C_3N_4 and Pd-g-C_3N_4 nanocomposite, a series of LSV measurements were carried out at various rotation rates varied from 400 to 2400 rpm in an O_2-saturated 0.1 M KOH electrolyte. As shown in Fig. 7.7a and Fig. 7.7c, the ORR current density was simultaneously improved along with the increase of the rotation rate, which could be ascribed to the improvement of the oxygen transfer. In case of Pd-g-C_3N_4 electrode, the limiting current densities were much larger than those obtained at the g-C_3N_4 electrodes under the same rotation speed. The number of electrons transferred per oxygen molecule in case of ORR was estimated using the aforementioned K-L equations. Fig. 7.7b and 7.7d display the K-L plots of the ORR at various electrode potentials for g-C_3N_4 and Pd-g-C_3N_4 electrodes, respectively. It was found the only two electrons were involved in the reaction in case of g-C_3N_4 with formation of mixture of superoxide and hydroxide where the reaction is not complete.[35] Whereas in case of Pd-g-C_3N_4 nanocomposite all the four electrons are completely utilised to form hydroxide.

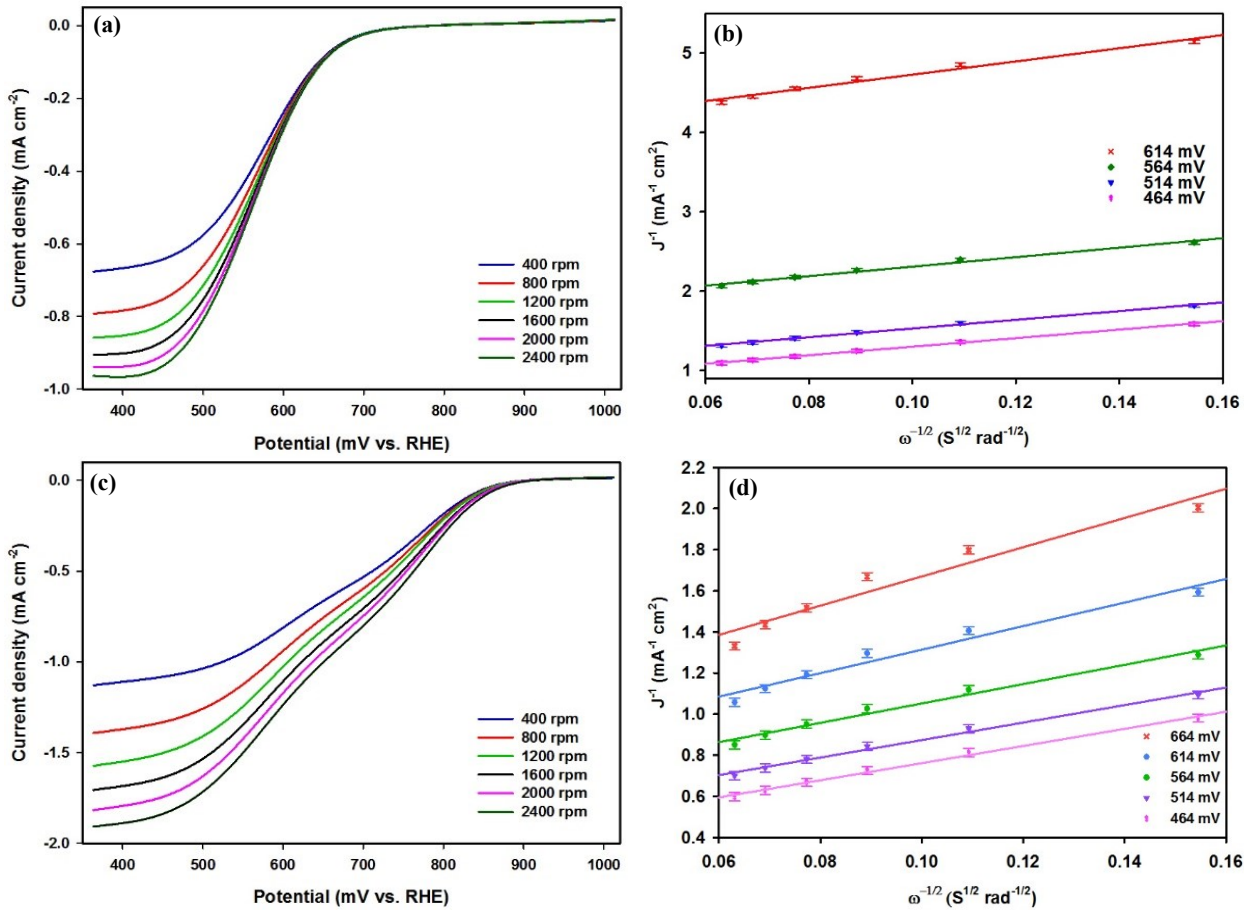

Figure 7.7: LSV curves of the g-C_3N_4 and Pd-g-C_3N_4 RDEs in O_2-saturated 0.1 M KOH (A) and (C) at various rotating rates. K-L plots obtained from the RDE measurements of g-C_3N_4 (B) and Pd-g-C_3N_4 (D) in O_2-saturated 0.1 M KOH solution.

7.3.4 Methanol tolerance effect

Another critical factor involved with the performance evaluation of electrocatalysts for the ORR is the level of methanol tolerance. It is well-known that methanol may crossover the membrane, which may significantly lower the performance of the fuel cell.[40] Fig. 7.8 displays the relative current density vs. time curves of the commercial benchmark Pt/C and the Pd-g-C_3N_4 nanocomposite measured in an O_2-saturated 0.1 M KOH electrolyte at 0.61 V vs. RHE at 1600 rpm. When 3.0 M methanol was introduced into the solution, a dramatic decrease of current at the Pt/C electrode was observed; however, the current density of the Pd-g-C_3N_4 nanocomposite was slightly decreased (less than 3%). These results show that the Pd-g-C_3N_4 nanocomposite was highly tolerant against methanol, offering a significant advantage over the benchmark Pt/C material for the ORR.

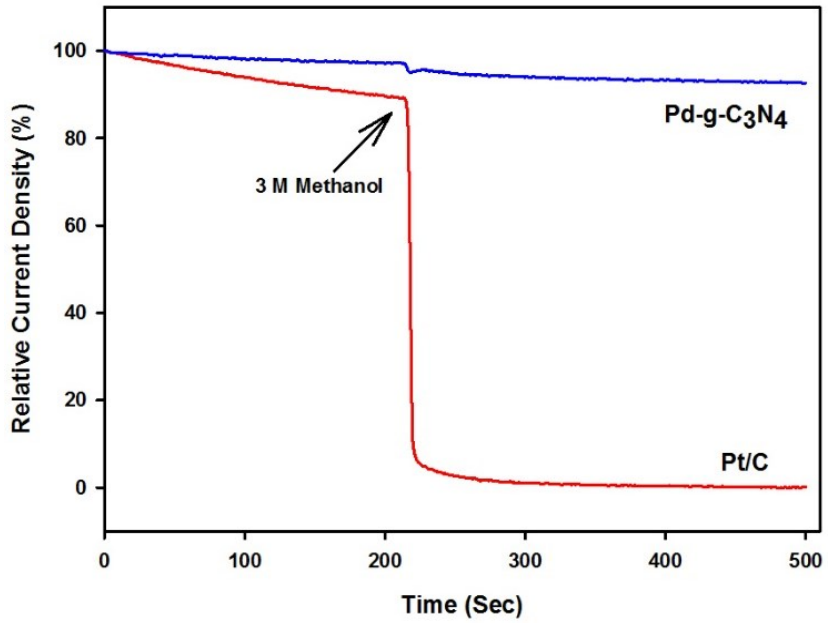

Figure 7.8: Effect of methanol on the ORR at the commercial Pt/C and the Pd-g-C_3N_4 nanocomposite in an O_2-saturated 0.1 M KOH electrolyte at the applied electrode potential of 0.61 V vs. RHE at the rotating rate of 1600 rpm. 3 M methanol was introduced after 200 sec.

7.3.5 Stability for the ORR

Electrocatalyst durability is another major concern in the performance of fuel cells. Carbon based materials are fraught with stability problems attributed to frail contacts between carbon/metal atoms. It is anticipated that nitrogen doping may enhance the bonding between the metal nanoparticles and the carbon support.[41] The long-term durability of the Pd-g-C_3N_4 nanocomposite and the Pt/C was also tested using CA at the applied electrode potential of 0.61 V, which are displayed in Fig. 7.9.

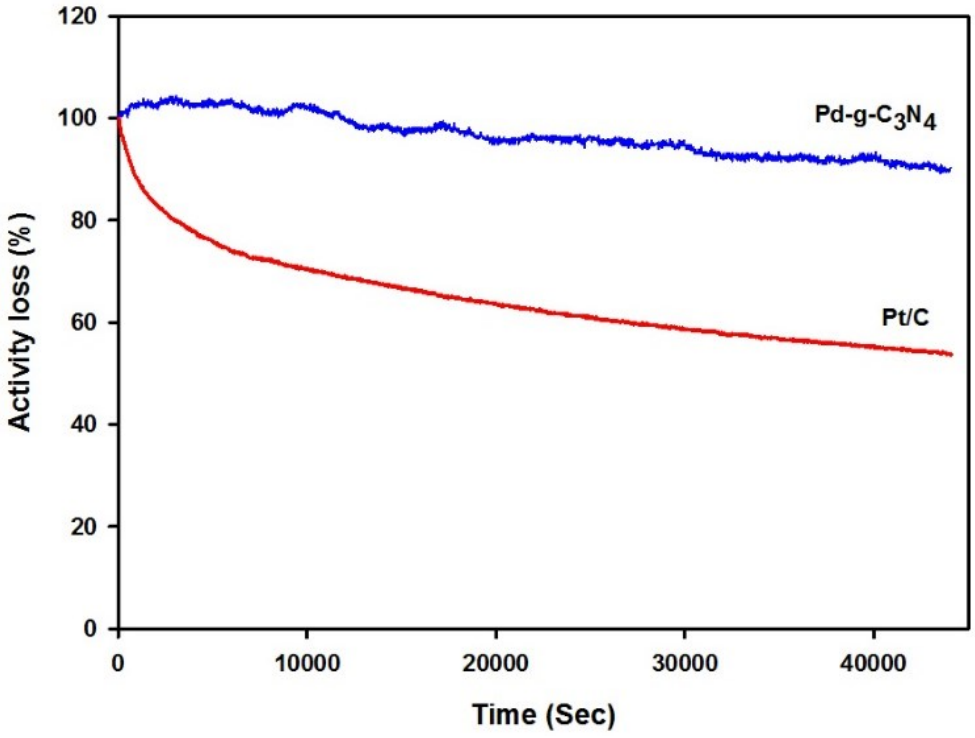

Figure 7.9: Stability tests of the Pd-g-C_3N_4 nanocomposite and the benchmark Pt/C material in O_2-saturated 0.1 M KOH at 0.61 V vs RHE under the rotating rate of 1600 rpm.

The activity of the Pd-g-C_3N_4 nanocomposite showed ~8% loss over 45000 s of the test; in contrast, over 45% loss was observed when the commercial 10 wt. % Pt/C catalyst was used. These results demonstrated that the Pd-g-C_3N_4 nanocomposite had superior stability over the benchmark

Pt/C, owing to the strong interaction between Pd nanoparticles and g-C_3N_4 frameworks. Therefore, the photo-assisted approach reported in this paper might be used further for the fabrication of different g-C_3N_4 based nanocomposite catalysts for promising environmental and energy applications.

7.4 Conclusions

We have demonstrated a facile and efficient photo-assisted chemical reduction approach for the direct formation of Pd nanoparticles onto the porous g-C_3N_4, which was synthesized by a rapid combustion technique. The prepared Pd-g-C_3N_4 nanocomposite was studied by various surface characterization techniques and electrochemical methods. The novel Pd-g-C_3N_4 nanocomposite exhibited significant enhancement for ORR in terms of the onset potential when compared with the advanced electrocatalysts recently reported in the literature. The tolerance to methanol crossover was significantly improved compared to the start-of-the-art Pt/C electrocatalyst. In addition, the Pd-g-C_3N_4 nanocomposite exhibited high stability for the ORR with only ~8% activity loss in comparison to 45% activity loss for the commercially available benchmark Pt/C catalyst. This study opens up new possibilities for the rational design and synthesis of platinum-free electrocatalysts with a significantly improved electrochemical performance for the development of fuel cell technologies.

References

1. L. Dai, Y. Xue, L. Qu, H.-J. Choi, J.-B. Baek. Metal-free catalysts for oxygen reduction reaction. *Chem. Rev.* **2015,** 115, 4823-4892.

2. M. del Cueto, P. Ocón, J. M. L. Poyato. Comparative study of oxygen reduction reaction mechanism on nitrogen-, phosphorus-, and boron-doped graphene surfaces for fuel cell applications. *J. Phys. Chem. C* **2015,** 119, 2004-2009.

3. M. Govindhan, A. Chen. Simultaneous synthesis of gold nanoparticle/graphene nanocomposite for enhanced oxygen reduction reaction. *J. Power. Sources* **2015,** 274, 928-936.

4. C. Sealy. The problem with platinum. *Mater. Today* **2008,** 11, 65-68.

5. N. Zhang, H. Yan, X. Chen, L. An, Z. Xia, D. Xia. Origins for the synergetic effects of $AuCu_3$ in catalysis for oxygen reduction reaction. *J. Phys. Chem. C* **2015,** 119, 907-912.

6. Y. Holade, N. E. Sahin, K. Servat, T. W. Napporn, K. B. Kokoh. Recent advances in carbon supported metal nanoparticles preparation for oxygen reduction reaction in low temperature fuel cells. *Catalysts* **2015,** 5, 310-348.

7. W. Alammari, M. Govindhan, A. Chen. Modification of TiO_2 nanotubes with PtRu/graphene nanocomposites for enhanced oxygen reduction reaction. *ChemElectroChem* **2015,** 2, 2041-2047.

8. S. M. Lyth, Y. Nabae, S. Moriya, S. Kuroki, M.-a. Kakimoto, J.-i. Ozaki, S. Miyata. Carbon nitride as a nonprecious catalyst for electrochemical oxygen reduction. *J. Phys. Chem. C* **2009,** 113, 20148-20151.

9. M. Xu, L. Han, S. Dong. Facile fabrication of highly efficient g-C_3N_4/Ag_2O heterostructured photocatalysts with enhanced visible-light photocatalytic activity. *ACS Appl. Mater. Interfaces* **2013,** 5, 12533-12540.

10. F. Goettmann, A. Fishcer, M. Antonietti, A. Thomas. Mesoporous graphitic carbon nitride as a versatile, metal-free catalyst for the cyclisation of functional nitriles and alkynes. *New. J. Chem*, **2007**, 31, 1455-1460.

11. A. Chen, C. Ostrom. Palladium-based nanomaterials: synthesis and electrochemical applications. *Chem. Rev.* **2015,** 115, 11999-12044.

12. A. Ferre-Vilaplana, E. Herrero. Charge transfer, bonding conditioning and solvation effect in the activation of the oxygen reduction reaction on unclustered graphitic-nitrogen-doped graphene. *Phys. Chem. Chem. Phys.* **2015,** 17, 16238-16242.

13. S. K. Konda, A. Chen. Palladium based nanomaterials for enhanced hydrogen spillover and storage. *Mater. Today* **2015,** 19, 100-108.

14. R. Modibedi, K. Ozoemena, M. Mathe. Palladium-based nanocatalysts for alcohol electrooxidation in alkaline media. In *Electrocatalysis in Fuel Cells*, Shao, M., Ed. Springer London: **2013**, 9, 129-156.

15. S. K. Konda, C. K. Ostrom, A. Chen. Synthesis and electrochemical study of Cd@Pd core/shell nanomaterials for hydrogen sorption and storage. *Int. J. Hydrogen. Energ.* **2015,** 40, 16365-16374.

16. L. Arroyo-Ramírez, R. Montano-Serrano, T. Luna-Pineda, F. R. Román, R. G. Raptis, C. R. Cabrera, Synthesis and characterization of palladium and palladium–cobalt nanoparticles on vulcan XC-72R for the oxygen reduction reaction. *ACS Appl. Mater. Interfaces* **2013,** 5, 11603-11612.

17. S. Tominaka, T. Hayashi, Y. Nakamura, T. Osaka. Mesoporous PdCo sponge-like nanostructure synthesized by electrodeposition and dealloying for oxygen reduction reaction. *J. Mater. Chem.* **2010,** 20, 7175-7182.

18. J. S. Jirkovský, A. Björling, E. Ahlberg. Reduction of oxygen on dispersed nanocrystalline CoS_2. *J. Phys. Chem. C* **2012,** 116, 24436-24444.

19. S. Kondo, M. Nakamura, N. Maki, N. Hoshi. Active sites for the oxygen reduction reaction on the low and high index planes of palladium. *J. Phys. Chem. C* **2009,** 113, 12625-12628.

20. W.-P. Zhou, K. Sasaki, D. Su, Y. Zhu, J. X. Wang, R.R. Adzic, Gram-scale-synthesized Pd_2Co-supported Pt monolayer electrocatalysts for oxygen reduction reaction. *J. Phys. Chem. C* **2010,** 114, 8950-8957.

21. S. J. Hwang, S. J. Yoo, J. Shin, Y.-H.Cho, J. H. Jang, E. Cho, Y.-E. Sung, S. W. Nam, T.-H. Lim, S.-C. Lee, S.-K. Kim. Supported core@shell electrocatalysts for fuel cells: close encounter with reality. *scientific reports* **2013,** 3, 1309.

22. J. Liu, T. Zhang, Z. Wang, G. Dawson, W. Chen. Simple pyrolysis of urea into graphitic carbon nitride with recyclable adsorption and photocatalytic activity. *J. Mater. Chem.* **2011,** 21, 14398-14401.

23. S. Fu, C. Zhu, H. Li, D. Du, Y. Lin. One-step synthesis of cobalt and nitrogen co-doped carbon nanotubes and their catalytic activity for the oxygen reduction reaction. *J. Mater. Chem. A* **2015,** 3, 12718-12722.

24. M. Kim, S. Hwang, J.-S. Yu. Novel ordered nanoporous graphitic C_3N_4 as a support for Pt-Ru anode catalyst in direct methanol fuel cell. *J. Mater. Chem.* **2007,** *17*, 1656-1659.

25. G. Wu, S. S. Thind, J. Wen, K. Yan, A. Chen. A novel nanoporous α-C_3N_4 photocatalyst with superior high visible light activity. *Appl. Catal. B-Environ.* **2013,** 142–143, 590-597.

26. B. Chai, T. Peng, J. Mao, K. Li, L. Zan. Graphitic carbon nitride (g-C_3N_4)-Pt-TiO_2 nanocomposite as an efficient photocatalyst for hydrogen production under visible light irradiation. *Phys. Chem. Chem. Phys.* **2012,** 14, 16745-16752.

27. Y. Li, J. Zhang, Q. Wang, Y. Jin, D. Huang, Q. Cui, G. Zou, Nitrogen-rich carbon nitride hollow vessels: synthesis, characterization, and their properties. *J. Phys. Chem. B* **2010,** 114, 9429-9434.

28. T. Komatsu, T. Nakamura. Polycondensation/pyrolysis of tris-s-triazine derivatives leading to graphite-like carbon nitrides. *J. Mater. Chem.* **2001,** 11, 474-478.

29. Q. Guo, Q. Yang, L. Zhu, C. Yi, S. Zhang, Y. Xie. A facile one-pot solvothermal route to tubular forms of luminescent polymeric networks $[(C_3N_3)_2(NH)_3]_n$. *Solid. State. Commun.* **2004,** 132, 369-374.

30. Y. Zhao, K. Watanabe, K. Hashimoto. Self-supporting oxygen reduction electrocatalysts made from a nitrogen-rich network polymer. *J. Am. Chem. Soc.* **2012,** 134, 19528-19531.

31. S. Kundu, W. Xia, W. Busser, M. Becker, D. A.Schmidt, M. Havenith, M. Muhler. The formation of nitrogen-containing functional groups on carbon nanotube surfaces: a quantitative XPS and TPD study. *Phys. Chem. Chem. Phys.* **2010,** 12, 4351-4359.

32. S. K. Konda, A. Chen. One-step synthesis of Pd and reduced graphene oxide nanocomposites for enhanced hydrogen sorption and storage. *Electrochem. Commun.* **2015,** 60, 148-152.

33. H. Erikson, A. Sarapuu, N. Alexeyeva, K. Tammeveski, J. Solla-Gullón, J. M. Feliu. Electrochemical reduction of oxygen on palladium nanocubes in acid and alkaline solutions. *Electrochim. Acta* **2012,** 59, 329-335.

34. S.-S. Kim, Y.-R. Kim, T. D. Chung, B.-H. Sohn. Tunable decoration of reduced graphene oxide with Au nanoparticles for the oxygen reduction reaction. *Adv. Funct. Mater.* **2014,** 24, 2764-2771.

35. J. Tian, R. Ning, Q. Liu, A. M. Asiri, A. O. Al-Youbi, X. Sun. Three-dimensional porous supramolecular architecture from ultrathin g-C_3N_4 nanosheets and reduced graphene oxide:

solution self-assembly construction and application as a highly efficient metal-free electrocatalyst for oxygen reduction reaction. *ACS Appl. Mater. Interfaces* **2014,** 6, 1011-1017.

36. Z.-S. Wu, S. Yang, Y. Sun, K. Parvez, X. Feng, K. Müllen. 3D Nitrogen-doped graphene aerogel-supported Fe_3O_4 nanoparticles as efficient electrocatalysts for the oxygen reduction reaction. *J. Am. Chem. Soc.* **2012,** 134, 9082-9085.

37. H. Zhu, S. Zhang, Y.-X.Huang, L. Wu, S. Sun. Monodisperse $MxFe_{3–x}O_4$ (M = Fe, Cu, Co, Mn) nanoparticles and their electrocatalysis for oxygen reduction reaction. *Nano Letters* **2013,** 13, 2947-2951.

38. Y. Cheng, W. Li, X. Fan, J. Liu, W. Xu, C. Yan. Modified multi-walled carbon nanotube/Ag nanoparticle composite catalyst for the oxygen reduction reaction in alkaline solution. *Electrochimica Acta* **2013,** 111, 635-641.

39. L. Kuai, X. Yu, S. Wang, Y. Sang, B. Geng. Au–Pd alloy and core–shell nanostructures: one-pot coreduction preparation, formation mechanism, and electrochemical properties. *Langmuir* **2012,** 28, 7168-7173.

40. N. K. Chaudhari, M. Y. Song, J.-S., Yu. Heteroatom-doped highly porous carbon from human urine. *Scientific Reports* **2014,** 4, 5221.

41. X. Fu, Y. Liu, X. Cao, J. Jin, Q. Liu, J. Zhang. FeCo–Nx Embedded graphene as high performance catalysts for oxygen reduction reaction. *Appl. Catal. B-Environ.* **2013,** 130–131, 143-151.

42. S. Mao, Z. Wen, T. Huang, Y. Hou, J. Chen. High-performance bi-functional electrocatalys of 3D crumpled graphene-cobalt oxide nanohybrids for oxygen reduction and evolution reactions. *Enery Environ. Sci*. **2014,** 7, 609-616.

Chapter 8: Summary and Conclusions

Metal hydrides are considered as one of the most promising candidates for safe, compact, and efficacious hydrogen storage for mobile applications. However, none of the presently known materials meets all the requirements in terms of hydrogen sorption conditions, hydrogen storage capacity, and reversibility. Although Pd has strong potential to serve as a catalyst for hydrogen storage and the oxygen reduction reaction, several issues pertaining to pure Pd include its limited supply, considerable expense, poor gravimetric capacity, and hydrogen embrittlement issues, which must be resolved prior to the realization of a hydrogen based economy. As reported in this thesis, great progress was made toward addressing these challenges by utilizing Pd with cost-effective materials, synthesizing various Pd-based nanomaterials/nanocomposites, increasing the lattice, and employing appropriate support materials for hydrogen spillover and for the oxygen reduction reaction in fuel cells.

As described in Chapter 4 of this thesis, a facile and efficient approach was developed for the synthesis of Cd@Pd core/shell nanostructures. This method was effective for controlling the compositions of the formed core/shell nanoparticles. The effect of a capping agent was investigated, revealing that it played a critical role in the formation of the uniform and small size of the Cd@Pd nanoparticles, resulting in a significant improvement in hydrogen sorption and storage. The formation of the Cd@Pd core/shell nanostructures was confirmed by HRTEM and XRD analysis, as well as cyclic voltammetric studies based on the electrochemical behaviours of hydrogen sorption and desorption. The capacity for hydrogen sorption and storage was strongly contingent on the composition and structure of the formed Pd-based nanomaterials, as well as the applied electrode potential. It was increased in the following order: CdPd(1:1) <Pd <Cd@Pd(1:3) <Cd@Pd(1:2), showing that the Cd@Pd core/shell nanoparticles with a 1:2 ratio exhibited the

highest capacity for hydrogen storage. A significant increase in the peak current and a dramatic positive shift for the peak potential were due to the α phase and β phase transition, when the held electrode potential was lowered, from -180 to -200 mV. These studies revealed that by forming Cd@Pd core/shell nanostructures with an optimized composition of 1:2, a 340% increase in hydrogen storage capacity was achieved, in comparison with pristine Pd nanoparticles.

The effect of annealing on the electrosorption of hydrogen into Pd thin foils was studied using in-situ XRD, and electrochemical methods were discussed in Chapter 5. Pd thin foils were morphologically and structurally characterized by SEM, XRD, and XPS, as well as being electrochemically studied using CV, CA, and LSV to elucidate the electrochemical kinetics of hydrogen uptake and release. The capacity for hydrogen sorption and storage was strongly contingent on the crystal structure and lattice parameters of the formed Pd thin foils, as well as the applied electrode potential. The presence of α and β phases, as well as the phase transition were clearly observed and identified with respect to the applied electrode potential. Pd foils that were annealed at 700 °C demonstrated the highest hydrogen uptake capacity, with a 3.4-fold increase in the α phase hydrogen storage and a 19.3-fold increase in the β phase hydrogen storage, in comparison to the untreated Pd thin foil. The present study provided insights not only for hydrogen sorption, but also demonstrated that a facile annealing process could significantly enhance the hydrogen uptake and storage capacity of Pd.

In Chapter 6, a new Pd/rGO nanocomposite was synthesized via a simple one-step electrochemical reduction approach, which facilitated the formation of highly dense and uniform Pd nanoparticles and rGO nanocomposites in the absence of any capping agents, organic solvents, or reducing chemicals. The synthesised Pd/rGO nanocomposite showed an enhanced capacity for hydrogen sorption in contrast to pure Pd nanoparticles.

The summary of materials that were discussed in chapter 4 to 6 were presented in table 8.1. With respect to the time required for hydrogen upload into the nanomaterials/nanocomposites and thin foil, it is observed that the kinetics are much faster in Pd/rGO nanocomposite, which requires only 3 minutes for the complete uptake of hydrogen into the system which is due to the spillover effect as mentioned in chapter 6. Among chemical and electrochemical reduction methods presented in this thesis, the electrochemical reduction approach presented in this thesis is simple and may be applied to fabricate various metallic nanoparticles and rGO nanocomposites for the further improvement of hydrogen sorption and energy storage capacities.

Table 8.1: Summary of key findings from chapters 4 to 6.

Catalyst	**Synthesis Method**	**Hydrogen Uploading Time (min)**	**Pd Oxidation States (%)**		**Q_H (mC. $cm^{-2}.mg^{-1}$)**
			Pd(0)	**Pd(II)**	
Pd Nanoparticles (Chapter 4)	Chemical Reduction	10	65.1	34.9	306
Cd@Pd(1:2) Nanostructures (Chapter 4)	Chemical Reduction	10	62.5	37.5	1131
Pd Thin Foil (untreated) (Chapter 5)	Commercial (Sigma-Aldrich)	10	90.5	9.5	9.2
Pd Thin Foil (Chapter 5)	Annealed at 700 °C	10	93.1	6.9	238
Pd/rGO Nanocomposites (Chapter 6)	Electrochemical Reduction	3	72.8	27.2	1199

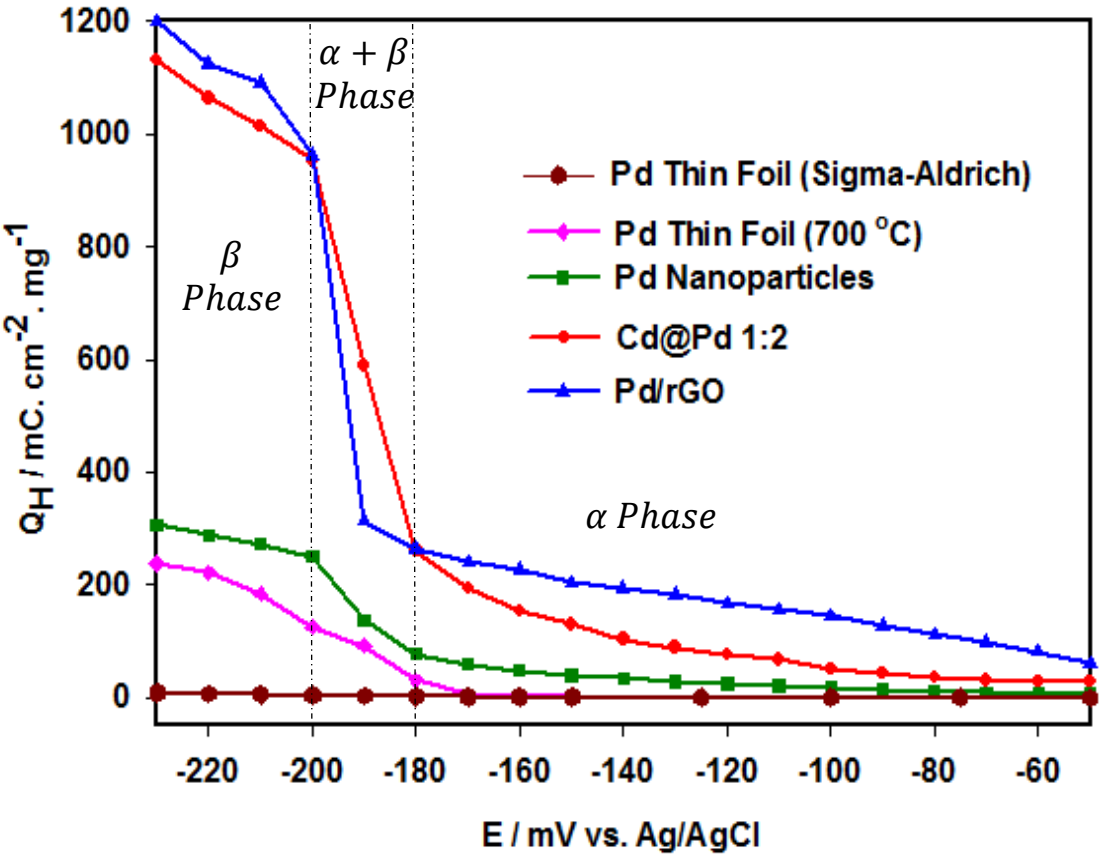

Figure 8.1. The overall hydrogen desorption charge, Q_H, normalized by the mass of Pd versus the held electrode potentials.

For comparison, Fig. 8.1 presents the hydrogen desorption charge capacity of the commercially available Pd thin foil purchased from sigma-aldrich, Pd thin foil which was annealed at 700 °C, Pd nanoparticles, Cd@Pd(1:2) core/shell nanoparticles and Pd/rGO nanocomposite, where the held electrode potential was varied from -50 to -230 mV vs Ag/AgCl. The hydrogen uptake capacity was increased with the decrease of the held electrode potential from -50 to -250 mV. In general electrode potential range above -180 mV corresponded to the α phase hydrogen sorption, where the amount of the hydrogen uptake was gradually increased with the decrease of the potential from -50 to -180 mV and the overall hydrogen sorption was low. The potential range below -200 mV corresponded

to the β phase hydrogen storage, potentials between -180 and -200 mV represented the α phase and β phase transition region, where the Q_H was significantly increased when the held electrode potential was decreased from -180 to -200 mV. The Pd/rGO nanocomposite had a strong positive impact on the hydrogen uptake capacity when the electrode potential was held from -50 to -230 mV. For example, for the α phase hydrogen sorption when the electrode potential was held at -180 mV, the uptake hydrogen capacity Q_H was increased in the following order: 2.4 mC (Commercial Pd thin foil) < 31.4 mC (Pd thin foil annealed @ 700 °C) < 78.0 mC (Pd nanoparticles) < 262.1 mC (Cd@Pd (1:2)) < 265.05 mC (Pd/rGO nanocomposite). The Pd/rGO nanocomposite showed the highest hydrogen sorption capacity, which was 100.4 times larger than that of the commercially available Pd thin foil. In the case of the β phase hydrogen storage when the electrode potential was held at -230 mV, the uptake hydrogen capacity Q_H was increased in the following order: 9.2 mC (Commercial Pd thin foil) 237.9 mC (Pd thin foil annealed @ 700 °C) < 306.7 mC (Pd nanoparticles) < 1131.7 mC (Cd@Pd (1:2)) < 1199.6 mC (Pd/rGO nanocomposite). The Pd/rGO nanocomposite showed a 130.3-fold increase in hydrogen uptake capacity in comparison to the commercially available Pd thin foil.

Finally, a facile and efficient photo-assisted chemical reduction approach for the direct formation of Pd nanoparticles onto the porous g-C_3N_4, which was synthesized by a rapid combustion technique, was presented in Chapter 7. The prepared Pd-g-C_3N_4 nanocomposite was investigated by various surface characterization techniques and electrochemical methods. Electrochemical analysis was performed to determine the hydrogen sorption behaviours of g-C_3N_4 and Pd-g-C_3N_4, hydrogen sorption behaviours were not observed for g-C_3N_4 but the prepared Pd-g-C_3N_4 showed hydrogen sorption capacities, which were smaller in comparison to pure Pd

nanoparticles. The novel Pd-g-C_3N_4 nanocomposite is tested for the electrochemical reduction of oxygen, which exhibited significant enhancement for the ORR, in terms of the onset potential, when compared with the advanced electrocatalysts that have recently been reported in the literature. The tolerance to methanol crossover was significantly improved compared to the start-of-the-art Pt/C electrocatalyst. In addition, the Pd-g-C_3N_4 nanocomposite exhibited high stability for the ORR, with only ~8% activity loss in comparison to 45% activity loss for the commercially available benchmark Pt/C catalyst. This study opens up new possibilities for the rational design and synthesis of platinum-free electrocatalysts with significantly improved electrochemical performance for the development of fuel cell technologies.

For hydrogen storage applications, where surface interactions are of greater concern than bulk phase absorption, the adsorption strength is the most crucial factor. All of these properties may be modified by synthesizing various Pd-based nanomaterials/nanocomposites. The optimization of the molecular composition of Pd with other materials using various synthesis methods are critical for the development of a hydrogen based economy. Along with the catalyst composition, factors such as support materials are also influential in varying the number of available active sites, which play an important role in enhanced hydrogen storage and for the oxygen reduction reaction in fuel cells. Future research work may focus on the following aspects: (i) Interaction of hydrogen with various other materials under variable conditions; (ii) investigations toward the elucidation of the mechanism of hydrogen spillover using a combination of spectroscopy and electrochemical techniques will provide further insights into a fundamental understanding of the spillover phenomenon; (iii) exploration of novel catalysts for fuel cell applications.

APPENDIX

List of Publications and Presentations

A.1. Journal Publications

- **S. K. Konda**, M. Amiri, A. Chen. Significant Enhancement of Electrosorption of Hydrogen into Palladium Via a Facile Annealing Process. *International Journal of Hydrogen Energy.* **2017***, in press.* (http://dx.doi.org/10.1016/j.ijhydene.2017.03.199)
- M. Amiri, **S. K. Konda,** A. Chen. Facile **S**ynthesis of a Novel Carbon Nitride/Reduced Graphene Oxide/Nickel Hydroxide Nanocomposite for Oxygen Reduction in Alkaline Media. *ChemElectoChem.* 4, **2017**, 1-6.
- **S. K. Konda**, M. Amiri, A. Chen. Photo-assisted Deposition of Palladium Nanoparticles onto Carbon Nitride for Efficient Oxygen Reduction. *Journal of Physical Chemistry C.* **2016,** 20, 14467−14473.
- **S. K. Konda**, A. Chen. Palladium Based Nanomaterials for Enhanced Hydrogen Spillover and Storage. *Materials Today.* **2016,** 19, 100-108.
- **S. K. Konda**, A. Chen. One Step Synthesis of Pd and Reduced Graphene Oxide Nanocomposite for Enhanced Hydrogen Sorption and Storage. *Electrochemistry Communications*. **2015,** 60, 148–152.
- **S. K. Konda**, C. K. Ostrom, A. Chen. Synthesis and Electrochemical Study of Cd@Pd Core/Shell Nanomaterials for Hydrogen Sorption and Storage. *International Journal of Hydrogen Energy*. **2015,** 40, 16365-16374.

A.2. Conference Presentations

A.2.1. Oral Presentations

- **S. K. Konda**, A. Chen. Synthesis and Electrochemical Study of Cd@Pd Nanomaterials for Hydrogen Storage**.** Research and Innovation Week, Mar 2014, Thunder Bay, Ontario, Canada.
- **S. K. Konda**, C.K. Ostrom, A. Chen. Synthesis and Electrochemical Study of Pd-Cd Nanomaterials for Hydrogen Purification and Storage. 97th CSC Conference June 2014, Vancouver. Canada.

- **S. K. Konda**, A. Chen. Synthesis and Electrochemical Studies of Pd-based Nanomaterials for Hydrogen Storage and Spillover**.** Research and Innovation Week, Mar 2016, Thunder Bay, Ontario, Canada.
- **S. K. Konda**, A. Chen. Pd-based Nanomaterials for Hydrogen Sorption and Storage. 99th CSC Conference. June 2016, Halifax, Nova Scotia, Canada.
- M.N. Hossan, **S. K. Konda**, A. Chen. Synthesis and Electrochemical Study of Cu/rGO Nanocomposite toward CO_2 Reduction. 99th CSC Conference, June 2016, Halifax, Nova Scotia, Canada.
- Chen, **S. K. Konda**, C. Ostrom. Synthesis and Electrochemical Study of Palladium Based Nanomaterials. 252nd ACS National Meeting, August 2016, Philadelphia, Pennsylvania, United States of America.
- Chen, **S. K. Konda**, S. Chen. Synthesis and Electrochemical Study of Palladium based Nanomaterials. ECS Conference, June 2016, Halifax, Nova Scotia, Canada.

A.2.1. Poster Presentations

- **S. K. Konda**, M. Amiri, A. Chen. Synthesis of Palladium and Carbon Nitride Nanocomposite for Oxygen Reduction. 99th CSC Conference, June 2016, Halifax, Nova Scotia, Canada.
- **S. K. Konda**, A. Chen. Palladium based Nanomaterials for Hydrogen Sorption and Storage. ECS Conference, June 2016, Halifax, Nova Scotia, Canada.
- **S. K. Konda**, C.K. Ostrom, B. Adams, A. Chen. Synthesis and Electrochemical FTIR Study of Nanoporous Palladium-Based Bimetallic Catalysts. 66th ISE Meeting, Oct 2015, Taipei, Taiwan.